Final Report

Black and Brown Carbon $(BC)^2$ Monitoring in Houston and El Paso in 2020

PGA: 582-20-12102-011
Grant Number: 582-18-81339

James Flynn III, Principal Investigator

Yuxuan Wang, Co-Investigator

University of Houston

Rebecca J. Sheesley, Co-Investigator

Sascha Usenko, Co-Investigator

Baylor University

June 30, 2021

Executive Summary

Recent efforts by TCEQ to monitor and study air quality in Texas cities have resulted in an improved understanding of the processes and sources which control urban air quality in Texas. Reductions in anthropogenic emissions through the implementation of cleaner technologies for sectors such as mobile sources and coal-fired power plants, have refocused efforts to understand the contribution of biomass burning to urban air pollution. The Black and Brown Carbon $(BC)^2$ 2020 study was designed to identify the influence of wildfires and dust events on urban air quality in Texas, specifically focused on the Houston and El Paso metropolitan areas. This project carries forward methodologies that were developed by the PIs in AQRP project 19-031 for El Paso in 2019 ozone season (Apr – Oct). Specifically, implementation of an aerosol optical monitoring protocol including continuous measurement of aerosol absorption and scattering at three wavelengths, event-based particulate matter (PM) filter-based collection and analysis for enhanced biomass and dust event characterization, co-location with a TCEQ site for meteorology, trace gas and PM measurements and supporting analysis of relevant satellite and trajectory models. The central indicator of biomass burning and dust impact at the $(BC)^2$ sites is the Ångström exponent. The Absorption Ångström Exponent (AAE) is used to track the influence of biomass burning through the quantification of the wavelength dependence of the aerosol absorption. Biomass burning aerosol has a strong wavelength dependence which results in an AAE >>1, while fossil combustion from motor vehicles has little wavelength dependence and an AAE ~1. The Scattering Ångström Exponent (SAE) is used to track the influence of dust through the quantification of the wavelength dependence of aerosol scattering. Larger particles have an SAE approaching zero while smaller particles have an enhanced SAE. The AAE and the SAE are monitored in realtime to characterize the influence of wildfires and dust on urban air quality in Texas. This scientific data can be directly used to help characterize and address air quality exceedance days.

For $(BC)^2$ 2020, four monitoring trailers were prepared and deployed adjacent to existing TCEQ sites in the Houston metropolitan area and in El Paso. The Houston sites were Galveston, West Liberty and Aldine. The El Paso site was at the University of Texas at El Paso (UTEP). Each trailer contained two tricolor absorption photometers (TAP, Brechtel) and one three-wavelength nephelometer (Aurora, Ecotech). Due to disruptions in preparation and deployment associated with the COVID-19 pandemic (please see section 2), the start date was different at each site. West Liberty started aerosol optical measurements on 6/26/20, while Aldine was started 7/1/20. The UTEP site started measurements on 9/25/20. Galveston started measurements on 10/11/20. Once started, the aerosol optical measurements ran continuously at each site until 11/15/20. In addition to the aerosol optical measurements, filter sampling was also conducted at each site. This filter sampling was conducted on different schedules at each site, depending upon identified biomass burning events and on the trailer deployment schedule at each site. The details of the filter sampling schedule are discussed in section 4.1.4.

Major Findings

1. Methodologies that were developed by the PIs in AQRP project 19-031 for El Paso in 2019, were also successfully deployed in Aldine, West Liberty, and Galveston to assess transport and wildfire influence in the Houston metro region.
2. The TAP + nephelometer was used to identify influence of biomass burning events on Houston metropolitan area's air quality. Findings were supported using satellite fire products, back trajectories, and aerosol composition measurements from co-located $PM_{2.5}$ filters.
    a. Filter-based composition provided additional ways to quantify wildfire impact via radiocarbon to soluble potassium ratios. It also illustrated the utility of sodium as an inland tracer for the extent and duration Saharan dust transport during Jun-July.
3. For seasonality during $(BC)^2$ 2020, the Saharan dust in July and Western wildfire in October were identified at multiple $(BC)^2$ 2020 sites. Saharan dust was supported using

MODIS aerosol optical depth measurements and aerosol composition. While Western wildfire was supported via NOAA HMS smoke, trajectory analysis and radiocarbon.

   a. The late fire season in October and November provided examples of long range and local biomass burning impacts. The three sites in the Houston metro area were used to better characterize the extent and influence of smoke events and to help better define source regions.

4. The TAP + nephelometer instrument suite provided a relatively low maintenance solution to conducting a long-term BB and dust monitoring campaigns and is sensitive enough to identify BB events when changes in PM concentrations alone are not indicative.
   a. The real-time nature of the aerosol optical measurements allows for better precision in characterizing the transport, intensity and duration of smoke into these urban areas.
5. The expansion of $(BC)^2$ to include the deployment and remote monitoring of multiple sites (spanning 750 miles along the 1-10 corridor) highlights the strength and flexibility of this approach and the utility of these methodologies even in a complex urban atmosphere, such as El Paso and Aldine as well as coastal and rural sites.

Recommendations for Future Analysis

1. The continuation of $(BC)^2$ to identify and assess periods of BB and dust influence in the Houston and El Paso metropolitan area. The $(BC)^2$ 2020 dataset will serve as the foundation for future multi-year studies to assess long-term trends by season and by urban area.
   a. Long term monitoring of wildfire and dust will also help to characterize any changes in these source impacts over time.
2. Along with site-specific AAEs developed in 2020, continue to analyze co-located $PM_{2.5}$ filters for radiocarbon and potassium ion, to quantify the impact of biomass burning on $PM_{2.5}$ concentrations and to establish a site-specific relationship between changes in AAE and the contribution of biomass burning.

3. Utilize aerosol optical data collected during the Corpus Christie San Antonio 2021 mobile field campaign and known or suspected areas of BB influence in 2020 and 2021 to identify potential $(BC)^2$ expansion sites along the 1-35 corridor. Note: that San Antonio would serve both the east-west and north-south sampling strategies.
4. Consider expansion to PM_{10} monitoring of aerosol absorption and scattering to better describe dust impacts in El Paso. This would also enable better characterization of potential mixed dust and smoke events which are anticipated when the dust is transported through regions of wildfire or agricultural burning prior to reaching El Paso.

Table of Contents

Executive Summary 2
Table of Contents 5
1. Introduction 18
2. Project Design 22
2.1. COVID delays 22
2.1.1. Impacts on Personnel, trailer buildout/deploy, and site setup 22
2.2. Network expansion to Houston 25
2.2.1. Implications for understanding regional impacts 25
3. Methods 27
3.1. Optical Absorption Measurements – Tricolor Absorption Photometer 27
3.2. Optical Scattering Measurements – Nephelometer 28
3.3. Optical Calculations 28
3.3.1. Ångström Exponents Calculations 28
3.3.2. Single Scattering Albedo 29
3.4. Particulate Matter Filter Sampling 29
3.5. Filter analysis 30
3.5.1. Organic and elemental carbon 30
3.5.2. Radiocarbon 30
3.5.3. Ion chromatography 31
3.6. Satellite data 33

3.6.1. HMS smoke product 33
3.6.2. VIIRS fire 33
3.6.3. Aerosol Optical Depth 33
3.7. Transport analysis 34
3.7.1. HYSPLIT Back Trajectories 34
3.7.2. 3D Tracer modeling 34
4. Results 38
4.1. Time Series Data 38
4.1.1. Aerosol Absorption and Scattering Coefficients 38
4.1.2. Optical properties – Ångström exponents and single scattering albedo 46
4.1.3. Site statistics 50
4.1.4. Filter-based PM composition 52
4.1.5. Supporting measurements including Trace Gas and realtime PM 59
4.2. Biomass Burning and Dust Events 63
4.2.1. Definition of BB event for each site 63
4.2.2. Definition of dust event for each site (MM + RJS) 65
4.2.2.1. Supporting data (e.g. satellite, filter analysis,) 68
4.2.3. Timeline of events – Houston and El Paso 75
4.2.4. Select Biomass burning events– Houston and El Paso 81
4.2.4.1. Houston - Late September and October 81
4.2.4.2. Late October 84
4.2.4.3. Trace gas enhancement ratios – NOx 90
4.2.4.4. Jun-Jul Saharan dust – Houston + NOAA ..... **Error! Bookmark not defined.**
5. Data Audits and Quality Assurance 101
5.1. Aerosol absorption – TAP A and TAP B 101
5.1.1. Data Audit 101
5.1.2. TAP intercomparison – all 103
5.1.3. Completeness, precision, and accuracy 105
5.2. Aerosol Scattering – Nephelometer 106
5.2.1. Data Audit 106
5.2.2. Nephelomter intercomparison – all 108
5.2.3. Completeness, precision, and accuracy 110

6. Conclusion 111
7. Recommendations for Additional Studies 112
8. References 114

List of Figures

Figure 1. Source regions of the 19 passive tracers in GEOS-Chem differentiated by distinct colors. San Antonio, Houston, Dallas-Fort Worth, and El Paso are indicated by four white boxes. 35
Figure 2. The 7-year average spatial distributions of the 19 passive tracers during summertime. 36
Figure 3. Time series of select normalized tracers (C_USA: Central USA, NW_USA: Northwest USA, NCA: Northern California, LA: Louisiana, SW_USA: Southwest USA) affecting the (a) Aldine, (b) El Paso, (c) Galveston, (d) West Liberty targeted grids. 37
Figure 4. Time series (hourly average) of absorption coefficient (σ_{abs}) and scattering coefficient (σ_{scat}) observed at Aldine during the month of July through November 2020. 39
Figure 5. Time series (hourly average) of absorption coefficient (σ_{abs}) and scattering coefficient (σ_{scat}) observed at West Liberty during the month of June through November 2020. 39
Figure 6. Time series (hourly average) of absorption coefficient (σabs) and scattering coefficient (σscat) observed at Galveston during the month of October through November 2020. 40
Figure 7. Time series (hourly average) of absorption coefficient (σabs) and scattering coefficient (σscat) observed at El Paso during the month of October through November 2020. 40
Figure 8. Diel variation in absorption coefficient (σabs) and scattering coefficient (σscat) observed at Galveston for October-November. The circle represents the average, and the line represents the median values of σabs and σscat, respectively. 42
Figure 9. Diel variation in absorption coefficient (σabs) and scattering coefficient (σscat) observed at Aldine. The circle represents the average, and the line represents the median values of σ_{abs} and σ_{scat}, respectively. 43
Figure 10. Diel variation in absorption coefficient (σabs) and scattering coefficient (σscat) observed at West Liberty. The circle represents the average, and the line represents the median values of σ_{abs} and σ_{scat}, respectively. 44
Figure 11. Diel variation in absorption coefficient (σabs) and scattering coefficient (σscat) observed at El Paso. The circle represents the average, and the line represents the median values of σ_{abs} and σ_{scat}, respectively. 45
Figure 12. Time series (hourly average) of Absorption Ångström Exponent (AAE) and Scattering Ångström Exponent (SAE) observed at West Liberty during the month of June through November 2020. 46
Figure 13. Time series (hourly average) of Single Scattering Albedo (SSA) observed at West Liberty during the month of June through November 2020. 47
Figure 14. Time series (hourly average) of Absorption Ångström Exponent (AAE) and Scattering Ångström Exponent (SAE) observed at Aldine during the month of July through November 2020. 47
Figure 15. Time series (hourly average) of Single Scattering Albedo (SSA) observed at Aldine during the month of July through November 2020. 48

Figure 16. Time series (hourly average) of Absorption Ångström Exponent (AAE) and Scattering Ångström Exponent (SAE) observed at Galveston during the month of October through November 2020. The missing data in November is associated with a delay in the filter change. 48
Figure 17. Time series (hourly average) of Single Scattering Albedo (SSA) observed at Galveston during the month of October through November 2020. 49
Figure 18. Time series (hourly average) of Absorption Ångström Exponent (AAE) and Scattering Ångström Exponent (SAE) observed at El Paso during the month of September through November 2020. 49
Figure 19. Time series (hourly average) of Single Scattering Albedo (SSA) observed at El Paso during the month of September through November 2020. 50
Figure 20. Time series of aerosol composition by site. This composition does not include insoluble minerals. Only dates with most of the data above detection limit were included in the figure. 54
Figure 21. Filter-based radiocarbon measurements from West Liberty, Aldine, and Galveston (top panel) and El Paso (bottom panel). 56
Figure 22. Filter-based potassium vs contemporary carbon across the three Houston- Galveston sites (n = 22). 58
Figure 23. Filter-based Potassium vs contemporary carbon for El Paso (n = 25). 59
Figure 24. Time series (hourly average) of trace gases (CO and NO_2) observed at West Liberty during the month of June through November 2020. The CO and NO_2 concentrations were taken from TCEQ CAMS 699 (UH- West Liberty) site. 60
Figure 25. Time series (hourly average) of trace gases (CO and NO2) observed at Aldine during the month of July through November 2020. The CO concentrations was taken from the BC2 trailer and NO_2 concentrations were taken from TCEQ CAMS 8 (Aldine, Houston) sites. 61
Figure 26. Time series (hourly average) of trace gases (CO) observed at Galveston during the month of October through November 2020. 61
Figure 27. Time series (hourly average) of trace gases (CO and NO_2) observed at El Paso during the month of September through November 2020. The CO and NO2 concentrations were taken from TCEQ CAMS 12 (UTEP) site. 62
Figure 28. Time series (hourly average) of $PM_{2.5}$ and PM_{10} observed at El Paso during the month of September through November 2020. The $PM_{2.5}$ and PM_{10} concentrations were taken from TCEQ CAMS 12 (UTEP) site. 62
Figure 29. Monthly percentage of datapoints with AAE > specific site average + 1σ and SAE > 0.5 at each site, an indicator of biomass burning influence (upper panel). The El Paso September bar represents data from Sept 25. Lower panel represents percentage of moving 4 hour average AAE > specific site average + 1σ and SAE > 1.0 at each site. 64
Figure 30. Monthly percentage of datapoints with SAE < 0.5 at each site, an indicator of dust influence (upper panel). Lower panel represents percentage of moving 4 hour average SAE > 0.5 and scattering coefficients > monthly average. 67

Figure 31. Time series of normalized tracers influencing the biomass burning transport event observed at the West Liberty site's targeted grids. Specific tracers were selected as they indicated an event on the date(s) of interest for biomass burning and aligned with possible source regions identified from back trajectories. Potential long range transport events are shown with black stars. Tracer abbreviations: C_USA: Central USA, NW_USA: Northwest USA, NCA: Northern California, SCA: Southern California, SW_USA: Southwest USA, LA: Louisiana, E_USA: Eastern USA, TX: Texas, N_GULF: Northern Gulf of Mexico, S_GULF: Southern Gulf of Mexico, N_MEXI: Northern Mexico. 69
Figure 32. Time series of normalized tracers influencing the biomass burning transport event observed at the Aldine site's targeted grids. Specific tracers were selected as they indicated an event on the date(s) of interest for biomass burning and aligned with possible source regions identified from back trajectories. Potential long range transport events are shown with black stars. Tracer abbreviations: C_USA: Central USA, NW_USA: Northwest USA, NCA: Northern California, SCA: Southern California, LA: Louisiana, E_USA: Eastern USA. 70
Figure 33. Time series of normalized tracers influencing the biomass burning transport event observed at the Galveston site's targeted grids. Specific tracers were selected as they indicated an event on the date(s) of interest for biomass burning and aligned with possible source regions identified from back trajectories. Potential long range transport events are shown with black stars. Tracer abbreviations: C_USA: Central USA, NCA: Northern California, SCA: Southern California, TX: Texas. 71
Figure 34. Time series of normalized tracers influencing the biomass burning transport event observed at the El Paso site's targeted grids. Specific tracers were selected as they indicated an event on the date(s) of interest for biomass burning and aligned with possible source regions identified from back trajectories. Potential long range transport events are shown with black stars. Tracer abbreviations: C_USA: Central USA, NW_USA: Northwest USA, NCA: Northern California, SCA: Southern California, SW_USA: Southwest USA. 72
Figure 35. Time series of normalized tracers influencing the dust influenced transport event observed at (a) Aldine, (b) West Liberty targeted grids. Specific tracers were selected as they indicated an event on the date(s) of interest for dust influenced and aligned with possible source regions identified from HYSPLIT back trajectories. Potential long range transport events are shown with black stars. Tracer abbreviations: C_USA: Central USA, NW_USA: Northwest USA, NCA: Northern California, SCA: Southern California, LA: Louisiana, E_USA: Eastern USA, TX: Texas, N_MEXI: Northern Mexico, C_MEXI: Central Mexico, S_MEXI: Southern Mexico. 73
Figure 36. Daily mean concentration maps of the central USA tracer for the targeted grids on identified event days. The maps for (a) Aldine on 10/3/2020, (b) El Paso on 9/29/2020, (c) Galveston 10/16/2020, and (d) West Liberty on 10/28/2020 confirms the central USA tracer's influence on the sites for these individual days. Black stars and site name labels indicate the location of the targeted grids for Aldine, El Paso, Galveston, and West Liberty, employed in the study. 74

Figure 37. Box and whisker plot for the AAE, SAE and SSA for the campaign average and the different dust and biomass burning events at West Liberty. The asterisk, triangle and the circle represent the average AAE, SAE and SSA values, respectively and the line represents the median values observed during the entire campaign and the respective event day..... 76
Figure 38. Box and whisker plot for the AAE, SAE and SSA for the campaign average and the different dust and biomass burning events at Aldine. The asterisk, triangle and the circle represent the average AAE, SAE and SSA values, respectively and the line represent the median values observed during the entire campaign and the respective event day..... 77
Figure 39 . Box and whisker plot for the AAE, SAE and SSA for the campaign average and the different dust and biomass burning events at Galveston. The asterisk, triangle and the circle represent the average AAE, SAE and SSA values, respectively and the line represents the median values observed during the entire campaign and the respective event day..... 78
Figure 40. Box and whisker plot for the AAE, SAE and SSA for the campaign average and the different dust and biomass burning events at El Paso. The asterisk, triangle and the circle represent the average AAE, SAE and SSA values, respectively and the line represents the median values observed during the entire campaign and the respective event day..... 79
Figure 41. Time series (hourly average) of AAE and SAE values observed at West Liberty and Aldine sites during late September and early October 2020 at Houston. 82
Figure 42. Spatial distribution of fire spots (retrieved from VIIRS), smoke cover (retrieved from NOAA fire and Hazard mapping model) during the biomass burning events at West Liberty and Aldine. The blue and red lines represent the 72 hours back trajectories obtained from the HYSPLIT model for the specific days at West Liberty and Aldine, respectively. 83
Figure 43. Time series (hourly average) of AAE and SAE values observed at West Liberty, Aldine, and Galveston sites during mid-October 2020 in Houston. 84
Figure 44. Spatial distribution of fire spots (retrieved from VIIRS), smoke cover (retrieved from NOAA fire and Hazard mapping model) during the biomass burning events at West Liberty, Aldine, and Galveston. The blue lines represent the 72 hours back trajectories. 84
Figure 45. Time series of AAE and SAE for Aldine, West Liberty, and Galveston in late October..... 85
Figure 46. Spatial distribution of fire spots (retrieved from VIIRS), smoke cover (retrieved from NOAA fire and Hazard mapping model) during the biomass burning events at West Liberty and Galveston. The blue and red lines represent the 72 hours back trajectories obtained from the HYSPLIT model for the specific days at West Liberty and Galveston, respectively..... 86
Figure 47. Time series of AAE and SAE for West Liberty and Galveston in mid-November.... 87
Figure 48. Spatial distribution of fire spots (retrieved from VIIRS), smoke cover (retrieved from NOAA fire and Hazard mapping model) during the biomass burning events at West Liberty and Galveston. The blue and red lines represent the 72 hours back trajectories obtained from the HYSPLIT model for the specific days at West Liberty and Galveston, respectively..... 87
Figure 49. Time series of AAE and SAE for West Liberty and Galveston in late September. NOTE: This include both dust and BB events over the course of two days..... 88

Figure 50. Time series of AAE and SAE for West Liberty and Galveston in mid-October..... 89
Figure 51. Spatial distribution of fire spots (retrieved from VIIRS), smoke cover (retrieved from NOAA fire and Hazard mapping model) during the biomass burning events at El Paso. The blue lines represent the 72 hours back trajectories obtained from the HYSPLIT model for the specific days at El Paso. 89
Figure 52. Enhancement ratios observed during the dust and biomass burning events at West Liberty. The circle (right y axis) shows the background values of the absorption/scattering coefficients at red, green and blue wavelengths, AAE and SAE taken for the calculation of the ER. 91
Figure 53. Enhancement ratios observed during the dust and biomass burning events at Aldine. The circle (right y axis) shows the background values of the absorption/scattering coefficients at red, green, and blue wavelengths, AAE and SAE taken for the calculation of the ER. 92
Figure 54. Enhancement ratios observed during the biomass burning events at Galveston. The circle (right y axis) shows the background values of the absorption/scattering coefficients at red, green, and blue wavelengths, AAE and SAE taken for the calculation of the ER. 93
Figure 55. Enhancement ratios observed during the dust and biomass burning events at El Paso. The circle (right y axis) shows the background values of the absorption/scattering coefficients at red, green, and blue wavelengths, AAE and SAE taken for the calculation of the ER. 94
Figure 56. VIIRS (Visible Infrared Imaging Radiometer Suite Instrument) true-color composite image showing blowing dust over the Gulf of Mexico during June 22, 2020..... 97
Figure 57. Spatial distribution of mean aerosol optical depth (AOD) at 550 nm derived from MODIS Terra deep blue product showing transport of dust from Sahara Desert to Southern US through Gulf of Mexico from June 18 to June 27, 2020..... 97
Figure 58. Spatial distribution of aerosol index (AI) over the study sites on June 22, 2020 as retrieved from NASA-NOAA's Suomi NPP satellite..... 98
Figure 59. Time series (hourly average) for fine PM scattering coefficient (σ_{scat}) observed at Puerto Rico (CPR), West Liberty (WL), Bondville (BND), and Appalachian State University (APP) during the month of June 2020. The shaded box highlights the dust events at each site. 99
Figure 60. Time series (hourly average) of fine PM scattering Angstrom exponent (SAE) observed at Puerto Rico (CPR), West Liberty (WL), Bondville (BND), and Appalachian State University (APP) during the month of June 2020. The shaded box highlights the dust event at the specific site. The pink dashed line indicates the campaign average SAE (Jun-Oct 2020) for WL. 100
Figure 61. Scatter plot between the aerosol absorption coefficient (Mm-1) measured at 365, 520 and 640 nm and calculated AAE using σabs measured using TAP A and TAP B (five-minute averages) at West Liberty. 101
Figure 62. Scatter plot between the aerosol absorption coefficient (Mm-1) measured at 365, 520 and 640 nm and calculated AAE using σabs measured using TAP A and TAP B (five-minute averages) at Galveston. 102

Figure 63. Scatter plot between the aerosol absorption coefficient (Mm^{-1}) measured at 365, 520 and 640 nm and calculated AAE using σ_{abs} measured using TAP A and TAP B (five-minute averages) at Aldine. 102
Figure 64. Scatter plot between the aerosol absorption coefficient (Mm^{-1}) measured at 365, 520 and 640 nm and calculated AAE using σ_{abs} measured using TAP A and TAP B (five-minute averages) at El Paso. 103
Figure 65. Scatter plot between the aerosol absorption coefficient (Mm^{-1}) at 640 nm and 520 nm wavelengths using measurements from TAP serial numbers 01 to 02 (a_1 to a_2) and TAP 05 to TAP 06 (b_1 to b_2). 104
Figure 66. Scatter plot between the aerosol absorption coefficient (Mm^{-1}) at 365 nm wavelengths and calculated AAE using measurements from TAP serial numbers 03 to 04 (a_3 to a_4) and TAP 07 to TAP 08 (b_3 to b_4). 105
Figure 67. Scatter plot between the measured total aerosol scattering coefficient (Mm^{-1}), total aerosol scattering corrected for angular truncation (true total scattering; Mm^{-1}) and calculated SAE at 635, 525 and 450 nm at West Liberty. 106
Figure 68. Scatter plot between the measured total aerosol scattering coefficient (Mm^{-1}), total aerosol scattering corrected for angular truncation (true total scattering; Mm^{-1}) and calculated SAE at 635, 525 and 450 nm at Aldine. 107
Figure 69. Scatter plot between the measured total aerosol scattering coefficient (Mm^{-1}), total aerosol scattering corrected for angular truncation (true total scattering; Mm^{-1}) and calculated SAE at 635, 525 and 450 nm at Galveston. 107
Figure 70. Scatter plot between the measured total aerosol scattering coefficient (Mm^{-1}), total aerosol scattering corrected for angular truncation (true total scattering; Mm^{-1}) and calculated SAE at 635, 525 and 450 nm at Galveston. 107
Figure 71. Scatter plot between the aerosol scattering coefficient (Mm-1) at measured (a) 635 nm (b) 525 nm (c) 450 nm and (d) calculated SAE using Nephelometer 01 to Nephelometer 04 (five-minute averages). 109

List of Tables

Table 1. Campaign averages for aerosol optical properties by site. All are listed as average ± standard deviation. σ_{abs} and σ_{scat} represents absorption and scattering coefficients, respectively measured at three different wavelengths..... 51
Table 2. Monthly averages of aerosol optical properties by site. [1] incomplete month. σ_{abs} and σ_{scat} represents absorption and scattering coefficients, respectively measured at three different wavelengths..... 51
Table 3. List of biomass burning influenced days.……80

List of Abbreviations

AAE	Absorption Ångström exponent
AQRP	Air Quality Research Program
σ_{abs}	Aerosol Absorption coefficient
$\sigma_{abs_{\lambda_1}}$	Absorption coefficient at 640 nm
$\sigma_{abs_{\lambda_2}}$	Absorption coefficient at 520 nm
$\sigma_{abs_{\lambda_3}}$	Absorption coefficient at 365 nm
σ_{scat}	Aerosol Scattering coefficient
$\sigma_{scat_{\lambda_1}}$	Scattering coefficient at 635 nm
$\sigma_{scat_{\lambda_2}}$	Scattering coefficient at 525 nm
$\sigma_{scat_{\lambda_3}}$	Scattering coefficient at 450 nm
BC	Black Carbon
BrC	Brown Carbon
σ_{bscat}	Aerosol back-scattering coefficient
CO	Carbon monoxide
CAMS	Continuous Air Monitoring Site
CLAP	Continuous Light Absorption Photometer
EC	Elemental Carbon
HYSPLIT	Hybrid Single Particle Lagrangian Integrated Trajectory Model
MODIS	Moderate Resolution Imaging Spectroradiometer
m^{-1}	Per meter
$m^2 g^{-1}$	Meters squared per gram
Mm^{-1}	Per Megameter
$\mu g/m^3$	Microgram per meter cubed
NASA	National Aeronautics and Space Administration

NOAA	National Oceanic and Atmospheric Administration
NO	Nitrogen monoxide
NO_2	Nitrogen dioxide
NO_x	Oxides of Nitrogen
O_3	Ozone
PM	Particulate matter
$PM_{2.5}$	Particulate matter with an aerodynamic diameter of 2.5 microns or less
PSAP	Particle Soot Absorption Photometer
r^2	Coefficient of Determination
SAE	Scattering Ångström exponent
SSA	Single Scattering Albedo
SOA	Secondary organic aerosol
TAP	Tricolor Absorption Photometer
TCEQ	Texas Commission on Environmental Quality
UTEP	University of Texas at El Paso
UV	Ultraviolet
VOC	Volatile Organic Compound

1. Introduction

Biomass burning, which can include wildfires, agricultural burning and residential wood smoke, emits particulate matter (PM) and a wide range of gas-phase pollutants. PM emissions from biomass burning are predominantly carbonaceous, with aerosol absorbance from both black carbon (BC, or elemental carbon) and brown carbon (BrC, or light-absorbing organic carbon) [1]. Biomass burning plumes can also impact ozone (O_3) and secondary organic aerosol (SOA) formation through the emission of NO_x (nitric oxide; NO and nitrogen dioxide; NO_2), sulfur dioxide, ammonia, and volatile organic compounds (VOCs). AQRP Project 16-008 and AQRP Project 16-024 identified biomass burning plumes from out-of-state as a significant source of regional background air pollution in Texas potentially impacting both O_3 and $PM_{2.5}$. Both El Paso and Houston are considered urban areas of interest in terms of defining impacts of biomass burning, specifically wildfires and long range transport.

Since the optical properties of BC and BrC will be utilized for source identification of biomass burning, a brief overview is warranted. Andreae and Gelencsér wrote a classic review of light-absorbing aerosols focused on BC and BrC [2]. BC is defined both by its light absorption and by its refractory nature. It is formed during combustion as nearly pure elemental carbon that has a graphitic-like structure and absorbs across the visible spectrum with a mass absorption efficiency of $7.5 \pm 1.2 m^2\ g^{-1}$ [2, 3]. Brown carbon, BrC or light-absorbing organic carbon [2], has been identified in emissions from smoldering biomass burning fires and unlike BC, it's absorption has a strong wavelength dependence (peaking in the UV). BrC has a very low absorbance in the visible and longer wavelengths, which are typically utilized by filter-based absorption techniques to determine BC (e.g., 600-900 nm). This difference in wavelength dependence for BrC vs BC, combined with the emission source differences, has resulted in utilization of BrC to BC absorption ratios to identify biomass burning plumes [1, 4-10].

Laboratory and chamber studies have identified compounds and secondary organic aerosol products which could potentially act as BrC [11, 12]. The precursor sources that have produced BrC in chambers when reacted in the presence of NO_x include aromatic compounds like

benzene, naphthalene, and m-cresol and also the biogenic compound, isoprene. These precursor compounds produced BrC under the specific conditions in the chamber. To assess whether these types of precursors and reactions are relevant in urban areas, field or ambient measurements are needed. There have been a few field studies which have apportioned the BrC as well as measuring its impact [13, 14]. Both of the referenced studies apportioned the BrC with co-located aerosol mass spectrometer measurements. The studies in the southeast US [14] and in Fresno, CA [13] both report that biomass burning dominates BrC. The study in Fresno had a contribution from an aged, nitro-organic factor as well [13], however, the biomass burning factor had a stronger contribution and a distinct temporal trend that matched the BrC absorption. In summary, although it is possible to have other BrC contributions, additional measurements, temporal trends, statistical methods and supporting remote sensing can facilitate clean separation of biomass burning BrC.

Considerable work has been done to quantify and characterize BC and aerosol absorption in the atmosphere using a variety of instrumentation and protocols [1, 15-27]. The most effective campaigns for investigation of BC and BrC have included more than one absorption instrument. This guarantees that the results can be compared across a variety of previous studies, but still incorporate the advancements of new technologies. Therefore, $(BC)^2$ El Paso includes both TAP and aethalometer measurement of wavelength-dependent aerosol absorption.

Cost-effective options for real-time monitoring have included many filter-based techniques, where light transmission through a filter media is measured at short intervals while atmospheric PM is slowly accumulating. There are uncertainties associated with this type of measurement, which can be large. Uncertainties associated with the filter can include: a lack of reference standard for quantification of BC, uncertainty in the scattering correction by the filter and PM loading resulting in shadowing effects [26, 28]. Additional uncertainties include specificity of light source wavelength, flow rate, and definition of size of sample area [26]. To assess the "best" instrument for a given application, these uncertainties need to be adequately addressed.

To address on-going issues with other filter-based, realtime BC and BrC instruments (i.e. high frequency of manual filter changes, problematic and contentious correction schemes for aerosol scattering and other filter effects), NOAA developed and constructed an aerosol absorption instrument, the continuous light absorption photometer or CLAP (tricolor absorption photometers, TAP, Bechtel, Inc. is the commercial version) that fulfilled the needs of long-term monitoring, improved corrections, multiple wavelengths, high sensitivity and low noise, precisely defined filter spot areas, temperature stabilization, with same correction factors as the PSAP, very low cost and very small instrument footprint [25]. To minimize uncertainty in absorption measurements, and to improve aerosol classification through complementary measurement of aerosol scattering, the $(BC)^2$ El Paso campaign deployed a three-wavelength nephelometer [1, 25]. The TAP represents the cutting edge of filter-based photometers and was purchased, deployed, and validated for long-term application during $(BC)^2$ El Paso in 2018-19.

Influence of biomass burning plumes was identified utilizing the absorption measurements of BC and BrC, using methodology based on recently published studies [1, 4, 6, 7, 29]. Specifically, high AAE values indicated the presence of BrC (1.5-4.5) and influence of biomass burning, while the typical urban combustion sources dominated by BC had a lower AAE value, which remained near 1. Higher concentrations of BrC in the aerosol results in a higher AAE value due to it's ability to selectively absorb short wavelengths. Motor vehicle exhaust, or similar fossil fuel combustion has been demonstrated to have an AAE value dominated by BC while biomass burning has been demonstrated to contribute the higher, BrC-influenced AAE [30]. AAE values can be calculated for specific absorption coefficient pairs or through the calculation of the slope of the difference in absorption coefficients over multiple wavelengths. Most recently, Laing et al. and Schmeisser et al., outlines the use of TAP aerosol light absorption coefficient measurements (σ_{abs}), nephelometer aerosol light scattering coefficient measurements (σ_{scat}) and CO to further characterize the influence of transported biomass burning plumes [1, 31]. Laing et al. identified that long-range transport events had lower AAE values and higher σ_{abs} to CO enhancement ratios ($\Delta\sigma_{abs}/\Delta CO$) as compared to more regional transport. This difference in AAE values was

attributed to two different possibilities. However, this example is for a remote site, and the use of enhancement ratios needs to be tested for Texas urban areas.

The AAEs reported in other studies may be site specific as transport time, combustion conditions and local mixing of sources may have an impact on the resultant optical properties. This is the rationale for the long field campaign that extends beyond the biomass burning season in El Paso: so that a site specific AAE average without biomass burning can be determined. Additional validation/instrumentation will be used during this project to confirm wildfire impacts (i.e., CO, and $PM_{2.5}$ from TCEQ monitoring sites in El Paso). Once validation is completed for a specific site, the absorption instruments may be sufficient in themselves to identify and quantify biomass burning contribution. This will be investigated during the $(BC)^2$ El Paso project, where a nephelometer will be deployed with the TAPs and aethalometer while synoptic TCEQ monitoring network data will be utilized for confirmation and further characterization.

While previous studies have focused on identification of biomass burning influence at remote sites, the $(BC)^2$ 2020 study was an urban study. This confounded the ability to identify by concentration differences or enhancement ratios. However, since the AAE is assessing the wavelength dependence of absorption, an intrinsic property, it has the unique utility to identify biomass-burning influence under lower concentration conditions.

2. Project Design

2.1.COVID delays

2.1.1. Impacts on Personnel, trailer buildout/deploy, and site setup

Despite rolling state and university shutdowns associated with the COVID-19 pandemic, the four sites and supporting infrastructure were constructed, prepped, and successfully deployed in 2020. The impacts of the pandemic could be measured both directly and indirectly and effect the project's effort at the personnel, trailer buildout/deploy, and site setup (i.e. the physical site infrastructure) level. These impacts resulted in the creations of new barriers and challenges for the project membership and associated universities including forced shutdowns, testing protocols, social distancing, and layoffs.

Throughout the pandemic, project personnel experienced social distancing and self-isolation (typically for 2 intervals). This resulted in delays due to limited in-person interactions between students and PIs, and between Baylor and UH group members. As the site rollout was concurrent with these shutdowns and challenges (e.g., social distancing), significant supply chain limitations impacted the delivery of instrumentation, equipment, materials, and consumables associated with this project. Supply limitations resulted in price increases for basic building materials, reduced availability of specific items, and increased lead times. Significant changes in lead times were experienced for supplies coming from overseas (i.e., Europe and the Digitals) and heavily impacted states (e.g., California and the TAPs). The acquisition of the two new Digitel high-volume $PM_{2.5}$ samplers (Digitel, Volketswil, Switzerland) was scheduled during the spring with a 6-week lead time. Due to heavy outbreaks across Europe and large-scale nationwide shutdowns, the $PM_{2.5}$ samplers were not received until August of 2020 (see monthly reports). A similar scenario occurred with the purchase of the optical instruments. The Brechtel TAPs are built in California, which experienced significant periods of statewide shutdowns and forces stay-at-home government mandates. Specifically, the TAP order (eight units) was delayed and Baylor received the TAPs in batches. The first batch of four TAPs was received May 11th. A similar scenario played out with the purchase of four Ecotech Aurora 3000 Nephelometers. All three companies worked diligently to overcome these significant challenges including the

instrumentation buildouts and pre and post-deployment technical support. Comparison studies for the TAP and nephelometers were conducted by Baylor has batches were received. One of the Aurora 3000 nephelometers was identified as an outlier and replaced with a fifth unit. The delays mentioned above resulted in a staggered deployment of the $(BC)^2$ trailers, where the first trailer (Aldine) was deployed in the last few days of June.

Beginning in late January 2020, shortly after Notice to Commence was issued, UH and Baylor began construction of three sampling trailers in PI Flynn's workshop. This workspace was used as there was not sufficient space for a build of this scale at either UH or Baylor given space constraints at the time. During February and early March Baylor faculty and students traveled to Magnolia and worked with UH faculty and staff to upgrade the cargo trailers for use as laboratories for this project. During March, when the scale of the COVID-19 pandemic began to be realized, both UH and Baylor effectively closed all on-campus operations and suspended travel. While this did significantly slow the completion of the three trailers since they were being built at PI Flynn's residence, he (and his family) were able to continue construction. Once deemed safe, some UH staff also helped with the completion. This was possible because PI Flynn's group was able to be deemed "essential" by the university. As the trailers became ready for instrument installation, they were delivered to PI Usenko's residence where he and his team were able to practice safe social distancing and adherence to mask guidance while installing and testing the systems. Additionally, the decision was made to deploy Baylor's Mobile Air Quality Lab #2 (MAQL2) to the UH site at West Liberty using much of the 2019 AQRP platform with upgraded instrumentation to match the other three measurement systems that were built under this project, resulting in significant savings in time and effort. While the pandemic restrictions certainly resulted in many weeks of delays, the first trailers were ready for deployment in June 2020, when the West Liberty and Aldine sites became operational.

Additional delays, either largely or in part, resulted from site preparations for the Galveston and El Paso sites. In Galveston, although site access was negotiated through the TCEQ Monitoring

Division the City of Galveston presented many hurdles to the expansion of the gravel pad outside the TCEQ fence line. With much of the country working from home, communication with the permitting departments was even more difficult than normal and prevented any kind of site visit to discuss practical solutions. Ultimately it became clear that the City would not allow the gravel pad to be extended for a parking space for the trailer in a reasonable manner or timeline, so an alternate plan was developed. In place of the gravel pad, a series of 18" square concrete pavers were arranged for the trailer tires which provided some additional elevation from potential standing water as well as to provide a stable footing for the trailer. Additional pavers were placed strategically around the perimeter for use with leveling/stabilizing jack stands to further improve the installation. This was so successful that it has become the group's preferred method for establishing temporary measurement sites when it is not necessary or practical to construct a more traditional measurement site.

The El Paso site construction was also delayed due to restrictions on activities in El Paso. At the time, El Paso was particularly hard hit by the pandemic, to the point where the hospitals adjacent to the measurement site were forced to bold both temporary hospital shelters in their parking lots, but also overflow morgues and parking for refrigerated trucks to deal with the high rate of fatal cases in the area. Eventually the crisis waned and the most severe restrictions on general activities in El Paso began to lift enough that progress could be made on the site preparations. The work performed expanded the gravel pad built for the 2019 AQRP project and provides a more suitable space for the new, larger sampling trailer described earlier. Additional complications for the deployment of this site were a result of the travel restrictions imposed by both UH and Baylor. In the case of UH, requests for an exception to the blanket travel ban were required to originate with the faculty member and be sent to the department chair, then to the Dean, followed by the Vice Provost for Research, and finally to the Provost, before responses could be fed back down the hierarchy. As with many government agencies and large institutions, this process took some time, but was ultimately approved. Eventually, in September, a small team was able to safely deploy the trailer and equipment to El Paso and train a local UT-El Paso student to assist in the routine operation of the site.

2.2.Network expansion to Houston

2.2.1. Implications for understanding regional impacts

The expansion of the optical network to the Houston metropolitan area involved utilizing the methodologies that were developed by the PIs in AQRP project 19-031 for El Paso in 2019, and deploying them successfully in Aldine, West Liberty, and Galveston as well as continuing to operate the El Paso $(BC)^2$ site (see Figure below). Within this experimental design, we see the specificity of these measurements (within a complex urban atmosphere) integrated into a multi-

Figure caption: Clockwise from top left: $(BC)^2$ trailers at Aldine, West Liberty, Galveston, and El Paso. Both Galveston and El Paso had Digitel samplers installed inside with inlets through the roof, while Aldine and West Liberty had URG samplers which were installed outside on the walkable roof.

faceted approach (i.e. combine real-time and subsequently offline measurements with remote satellite observations and forecasting), will significantly enhance our ability characterize BB and dust event in El Paso Houston metropolitan areas.

This expansion provides an opportunity for improving the following:

- Characterization of two major Texas cities – Houston and El Paso.
- Improved characterization of air quality throughout the state via a multi-city approach
    - El Paso and Houston are ~750 miles apart with very different air sheds
    - Houston has regional impacts from the East/Central US combined with periodic influence from Central and South America, while El Paso has regional impacts from the Southwest/West US and Mexico.
- Improved characterization of BB and dust arriving from the Gulf of Mexico at the Aldine, Galveston, and West Liberty sites.
- Increased spatial resolution for Houston through characterization of a single urban site (i.e. Aldine) and two upwind satellite sites (West Liberty and Galveston).
- Improved characterization of both interstate and international BB and dust transport.
- Opportunities to begin to assess plume transport across the State of Texas.
- On the national scale, the $(BC)^2$ 2020 campaign help fill critical gaps in the country's aerosol optical network. For example, the PIs worked with NOAA to track the multi-state impact of the June-July Saharan Dust event [32].

While these individual improvements and opportunities are significant, the combination of these improvements should also be considered. They will allow for improved real-time characterization of BB and dust events at the state level (eastside and westside along the I-10 corridor), while simultaneously provide site specific measurements. This framework will provide new opportunities to assess plume transport, specifically the aging/transport of BB plumes and subsequently air quality chemistry across the Houston metropolitan area.

Specifically, the combination of these improvements will lead to a better understand of where and when BB and dust is influencing air quality in Texas and as this dataset grows to better understand how BB and dust is impacting Texas air quality.

3. Methods

3.1. Realtime aerosol inlet

The real-time aerosol absorption and scattering instrumentation sampled off a $PM_{2.5}$ cyclone inlet which operated at 42 lpm. Flow was controlled after each instrument using a mass flow controller. These mass flow controllers were monitored remotely via DAQ Factory.

3.2. Optical Absorption Measurements – Tricolor Absorption Photometer

A tricolor absorption photometer (TAP; Model 2901, Brechtel Inc., Hayward, CA) was used to measure the aerosol light absorption coefficients (σ_{abs}) at UV (365 nm), green, (520 nm) and red (640 nm) wavelengths. The TAP is the commercially available version of NOAA's continuous light absorption photometer (CLAP) and uses 10 solenoid valves to consecutively sample through eight sample filter spots and two reference filter spots (Ogren et al., 2018). LED light sources simultaneously shine light through the sample and reference spots. The reference spot allows a differential measurement approach in the TAP so the increase in light attenuation due to deposited particles on the sample spot can be largely separated from filter effects. A transmittance threshold for light attenuation was set to 50% to change the sampling filter spot. Each of the 8 sample spots is separated from the other by O-rings that clamp the filter material to prevent any inter-spot leakage. The air flow passes through the filter and into a solenoid valve controlled by the TAP Reader software. For spot loading effect, TAP automatically does the correction using its inbuilt methodology (based on the filter correction method discussed by Ogren., 2010 and Ogren et al., 2017) and finally provides real time corrected absorption coefficients.

3.3. Optical Scattering Measurements – Nephelometer

Aerosol scattering coefficients (σ_{scat}) at three different wavelengths (450 blue, 525 green and 635 red) were measured using an Ecotech Aurora 3000 nephelometer. Ecotech Aurora 3000 nephelometer uses a white light source to illuminate the air sample and the light scattered by the aerosol particles (and gases) at a particular wavelength is measured using a photomultiplier tube. In addition, this nephelometer provides a separate measurement of particle back-scatter (σ_{bscat}). The instrument automatically calculates Rayleigh scattering from internally measured temperature and pressure and corrects the reported signal for those factors. Averaging time was determined based on the performance of the aethalometer and TAP instruments and set to a five-minute average.

3.4. Optical Calculations

3.4.1. Ångström Exponents Calculations

The TAP and nephelometer measurements were used to calculate the Ångström (Absorption and Scattering) exponents for characterization of the wavelength dependency of aerosol absorption and scattering, respectively. The Ångström exponent is calculated as the negative slope of the linear fit of the optical parameter versus the wavelengths on a log-log plot (Moosmüller and Chakrabarty, 2011). The Ångström exponents for three wavelength bands can be represented using the following equation (Bergstrom et al., 2007; Kirchstetter et al., 2004; Schnaiter, 2005; Schnaiter et al., 2006).

$$\text{Absorption Ångström Exponent} = -\frac{\ln\left(\sigma abs_{\lambda 1,}\, \sigma abs_{\lambda 2,}\, \sigma abs_{\lambda 3,}\right)}{\ln(\lambda 1, \lambda 2, \lambda 3)} \quad (1)$$

The absorption Ångström exponent (AAE) is calculated with the absorption coefficient data measured using the TAPs at 640, 520, 365 nm (λ_1, λ_2, and λ_3, respectively). The SAE is calculated with the scattering coefficient measured using the nephelometer at 450, 525 and 635 nm (λ_1, λ_2, and λ_3, respectively).

$$\text{Scattering Angstrom Exponent} = -\frac{\ln\left(\sigma scat_{\lambda 1,}\, \sigma scat_{\lambda 2,}\, \sigma scat_{\lambda 3,}\right)}{\ln(\lambda 1, \lambda 2, \lambda 3)} \quad (2)$$

SAE is an intrinsic property of the aerosol derived based on the wavelength dependency of the aerosol scattering. SAE is inversely related to the particle size which indicates that larger particles will have smaller SAE and vice-versa (Schmeisser et al., 2017).

3.4.2. Single Scattering Albedo

The single scattering albedo (SSA) is the ratio of scattering to the total extinction. SSA is considered as the proxy to estimate the radiative effects of the atmospheric aerosols and is calculated using the following equation:

$$SSA = \frac{\sigma_{scat}}{\sigma_{scat} + \sigma_{abs}} \quad (3)$$

where, σ_{scat} and σ_{abs} are the scattering coefficient and absorption coefficients, respectively. In conjunction with the AAE and SAE, the SSA can be used for aerosol source characterization.

3.5.Particulate Matter Filter Sampling

Atmospheric PM2.5 was collected on a 90 mm quartz fiber filter using a URG medium-volume air samplers (URG Corporation, Chapel Hill, NC) or equivalent with a 2.5 μm cyclone inlet. Sampling rates are typically 5.4 m3 hr-1. The air flow of the URG air sampler is controlled by a critical orifice and as a result only periodic calibration is needed. The sample flow is measured at the inlet with a calibrated flowmeter prior to filter collection to confirm flow rates for each sample. The URG samplers were used at Aldine and West Liberty for filter collection in 2020. Filter sampling with the URGs started at noon and ended the next day at 10:00.

Two new Digitel high volume PM2.5 samplers (Digitel, Volketswil, Switzerland) were deployed at Galveston and El Paso in 2020. These samplers have a PM2.5 inlet and operate at a flowrate of 500 l/min. The samplers have autosampler capabilities and were loaded with a week's worth of filters in Teflon-coated aluminum filter holders. Filter sampling with Digitel did midnight to midnight collections. The samplers utilize a 150mm quartz fiber filter. Filter blanks are collected at the front of each set of loaded filters for weekly sampling. Filter holders are cleaned between samples.

All filters used to capture atmospheric PM2.5 were analyzed for organic and elemental carbon (OC/EC) and a selection of filters was subsampled and analyzed for inorganic ions and radiocarbon.

Quartz fiber filters were subsampled and handled only under clean laboratory conditions: nitrile gloves for operators, fresh, baked aluminum foil surfaces, pre-cleaned stainless-steel tweezers and pre-cleaned stainless-steel razors and filter punches. Stainless steel filter punches (1.5 cm2) were used to isolate filter samplers for bulk carbon analysis. Filter punches and razors were cleaned between each batch of carbon analysis by sequential rinsing with DI water, acetone and hexane followed by wiping with blank filters.

3.6.Filter analysis

3.6.1. Organic and elemental carbon

The OC/EC analysis was performed on a Sunset Laboratory Carbon Analyzer. Daily checks include a blank run, calibration check using a sucrose standard, and duplicate analysis for every 10 samples. A 1.5 cm^2 punch is removed for each OC/EC run.

3.6.2. Radiocarbon

For the radiocarbon analysis, a subsample of the PM filters were acidified using HCl fumigation in a desiccator to remove carbonate. The acid fumigated samples were then be dried and shipped to a radiocarbon contract lab (e.g. National Ocean Sciences Accelerator Mass Spectrometry, NOSAMS, facility) for analysis. Results of the radiocarbon analysis was utilized to calculate the fraction of contemporary carbon and its ambient concentration.

NOSAMS measures the ratio of ^{14}C to ^{12}C for the samples, field blanks, and a modern reference standard which 0.95 times the specific activity of the oxalic acid, which is used as the standard reference material (Stuiver and Polach, 1977). The reported data from NOSAMS is in fraction modern (*Fm*) which described below.

The $\Delta^{14}C$ value can be calculated from the *Fm* as in equation 4 where the λ is the inverse of ^{14}C's half-life and *Yc* is the year the sample was collected. This Δ14C is the relative difference

between the standard reference material and the corrected, to account for decay that took place between collection and time of measurement.

$$F_m = \frac{(^{14}C/^{12}C)_{sample} - (^{14}C/^{12}C)_{blank}}{(^{14}C/^{12}C)_{AD1950} - (^{14}C/^{12}C)_{blank}}$$

The $\Delta^{14}C$ value of each sample can be used to apportion total carbon (TC: organic and elemental carbon) as either fossil fuel (*ffossil*) or contemporary carbon (*fcont*) using equation 5. For this calculation, a contemporary end member ($\Delta 14C_{cont}$) of +67.5‰ (an average of +107.5‰ and +28‰ representing wood burning and annual growth +28‰ (Zotter et al., 2014), respectively) and fossil end member ($\Delta 14C_{fossil}$) of -1000‰ (Gustafsson et al., 2009) was used.

$$\Delta^{14}C = [F_m * e^{\lambda(1950-Y_s)} - 1] * 1000$$

An uncertainty for each measurement was calculated based on the instrument's standard error, standard deviation, and relative difference from its blank correction.

$$\Delta^{14}C_{sample} = (\Delta^{14}C_{cont})(f_{cont}) + (\Delta^{14}C_{fossil})(1 - f_{cont})$$

3.6.3. Ion chromatography

Inorganic ion analysis was performed on a deionized water extraction of a subsample of the PM filters and filter blanks. The inorganic anion analysis was performed on a Dionex ICS-2100 Reagent Free Ion Chromatography System (Thermo Scientific Dionex, Waltham, MA 02451) for analysis of the inorganic anions and organic acids. A Dionex IonPac AG11-HC guard column (4x50 mm) helped with separation before a Dionex IonPac AS11-HC (4x250 mm) analytical column. An eluent gradient was utilized with a potassium hydroxide eluent generator. The mobile-phase flow rate was 1.5 mL min-1 and the column temperature was set to 30 °C. The eluent gradient is based on a Thermo Scientific application note (Christison, Saini, & Lopez, 2015). The calibration curve is comprised of seven to eight points starting from 0.1 mg/L to up to 50 mg/L. Standards for the inorganic anions were purchased from ThermoScientific. Only

concentrations that fall within the calibration curve or immediately below were accepted. For the inorganic cations, a Dionex Aquion system was utilized. The column is a Dionex IonPac CS12A (4x250 mm) with a Dionex IonPac CG12A (4x50 mm) guard column. The isocratic eluent is 20 mM MSA for 15 minutes. The 6-cation standard for the inorganic cations was purchased from ThermoScientific. The ICS-2100 and Aquion systems utilize the same autosampler. All data was blank subtracted using an average of the filter blanks. Uncertainty was calculated as the average percent difference for the check standard.

The concentrations of sea salt, non-sea-salt sulfate (nss-SO_4^{2-}), non-sea-salt potassium (nss-K^+), non-sea-salt magnesium (nss-Mg^{2+}), and non-sea-salt calcium (nss-Ca^{2+}) were calculated utilizing the IC data. To calculate sea salt concentrations 1.47 was used to represent the seawater mass ratio of $(Na^+ + K^+ + Mg^{2+} + Ca^{2+} + SO_4^{2-} + HCO_3^{2-})/Na^+$ (Equation 1) [33]. Previous studies do not include any Cl^- greater than the Cl^- to Na^+ sea water ratio of 1.8 to prevent the inclusion of non-sea-salt compounds and allow for Cl^- depletion [34-36]. This was also applied to the data for this study. Two samples at Aldine, four at West Liberty, and two at El Paso fell under this category.

$$[sea\ salt] = [Cl^-] + [Na^+] \times 1.47 \quad (1)$$

For the non-sea-salt compounds the concentration of sodium ([Na+]) and the compound of interest ([X]) were utilized with the ratio of that compound to sodium in sea water (k) to calculate their concentrations (Equation 2) [33, 37]. The ratio used for nss-SO_4^{2-} was 0.252, for nss-K^+ was 0.03595, for nss-Mg^{2+} was 0.121, and for nss-Ca^{2+} was 0.03791. The calculations can sometimes result in negative concentrations. To correct this, a linear regression of the nss-compound and sodium concentrations was performed. The slope of this regression was then added to the k value [38]. Negative values were obtained nss-Mg^{2+} at Aldine, Galveston, and El Paso. The corrected k values used for the sites were 0.103 for Aldine, 0.0785 for Galveston, and 0.0154 for El Paso.

$$[nss - X] = [X]_{total} - k[Na^+] \quad (2)$$

3.7.Satellite data

3.7.1. HMS smoke product

The National Oceanic and Atmospheric Administration (NOAA) Hazard Mapping System (HMS) Fire and Smoke Analysis product (https://www.ospo.noaa.gov/Products/land/hms.html) has been used to identify the presence of smoke over the study sites. The system combines polar and geostationary satellite observations in a common framework from where the smoke plumes are digitized by the image analyst experts in a quality-controlled way. The ability to detect smoke through the NOAA HMS product can be compromised by many factors affecting satellite smoke and fire observations. These mainly includes presence of cloud, tree canopy, terrain, and the time of the day (McNamara et al., 2004; Eastman and Warren, 2010).

3.7.2. VIIRS fire

The active fire spots retrieved from Visible Infrared Imaging Radiometer Suite (VIIRS), aboard the Suomi-National Polar-orbiting Partnership (S-NPP) satellite have been used here to determine the location of active fires across the United States and Mexico. The VIIRS 375 m active fire product (VNP14IDG) have been used. The algorithm for this product is built on the well-established Moderate Resolution Imaging spectroradiometer (MODIS) Fire and Thermal Anomalies algorithm using a contextual approach to detect thermal anomalies (Schroeder et al., 2014). Due to its high spatial resolution VIIRS captures more fire pixels than MODIS (Schroeder et al., 2014). The fire pixels with normal and high confidence levels only are used in this study. This helped in removal of all false fires typically associated with the sun glint during the daytime and gas flares.

3.7.3. Aerosol Optical Depth

MODIS Collection 6 (C6) Level 2 daily aerosol data (MOD04_3k) at 3km resolution was used to study the impact of transported Saharan Dust on the aerosol loading over the BC^2 site: West Liberty. The C6 aerosol data set is created from three separate retrieval algorithms that operate over different surface types. These are the two “Dark Target” (DT) algorithms for retrieving (1) over ocean (dark in visible and longer wavelengths) and (2) over vegetated/dark-soiled land

(dark in the visible), plus the "Deep Blue" (DB) algorithm developed originally for retrieving (3) over desert/arid land (bright in the visible) (Levy et al., 2013 and Remer et al., 2013).

3.8. Transport analysis

3.8.1. HYSPLIT Back Trajectories

Developed by NOAA's Air Resources Laboratory, the Hybrid Single-Particle Lagrangian Integrated Trajectory model (HYSPLIT) was utilized to determine the origin of the air masses influencing the $(BC)^2$ sites [39, 40]. Backward trajectories were run at 10 meters above ground level for 72-hour duration, and new trajectories were started every 6 hours. The trajectories were downloaded and imported to Google Earth Pro (version 7.3.2.5776 (32-bit)) for evaluation with the MODIS satellite data to determine possible biomass burning influences. Back trajectories can be computed at https://ready.arl.noaa.gov/HYSPLIT_traj.php.

3.8.2. 3D Tracer modeling

The GEOS-Chem model is a global 3-D chemical transport model (CTM) driven by the assimilated meteorological inputs from the Goddard Earth Observation System (GEOS) of the National Aeronautics and Space Administration (NASA) Global Modeling and Assimilation Office (GMAO). The GEOS-Chem model (v12-09) flex-grid simulations with synthetic passive tracers were conducted driven by Modern-Era Retrospective analysis for Research and Applications, version 2 (MERRA-2) data with a native resolution of 0.5° × 0.625° over North America, using lateral boundary conditions updated every 3 hours generated from a global GEOS-Chem simulation with a horizontal resolution of 2° × 2.5°. The passive-tracer simulation is a useful tool to determine the air mass origins in the model, as demonstrated in our prior work investigating long-range transport of Mexican pollutants (Wang S. et al. 2018).

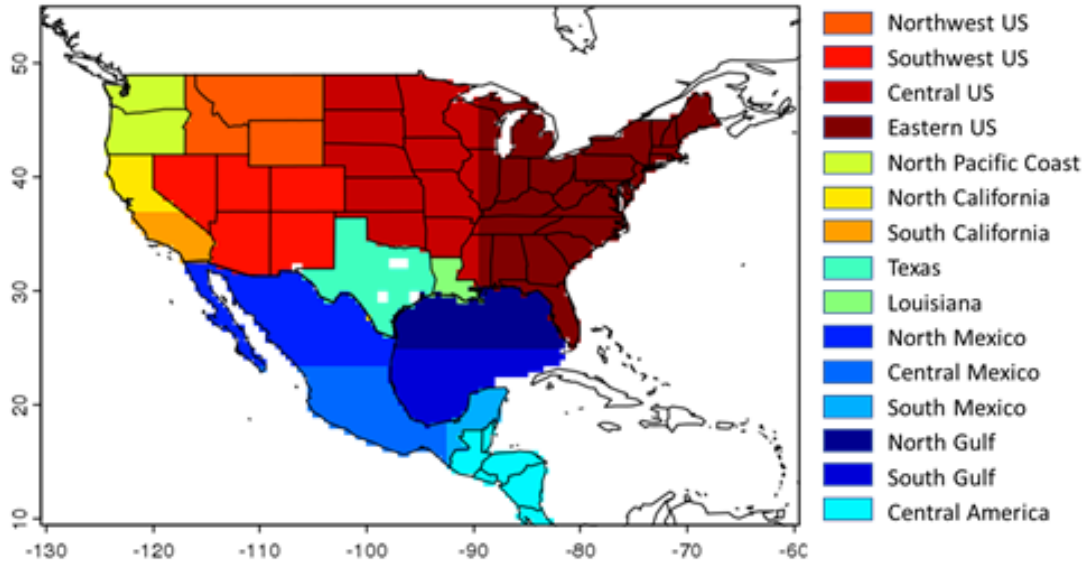

Figure 1. Source regions of the 19 passive tracers in GEOS-Chem differentiated by distinct colors. San Antonio, Houston, Dallas-Fort Worth, and El Paso are indicated by four white boxes.

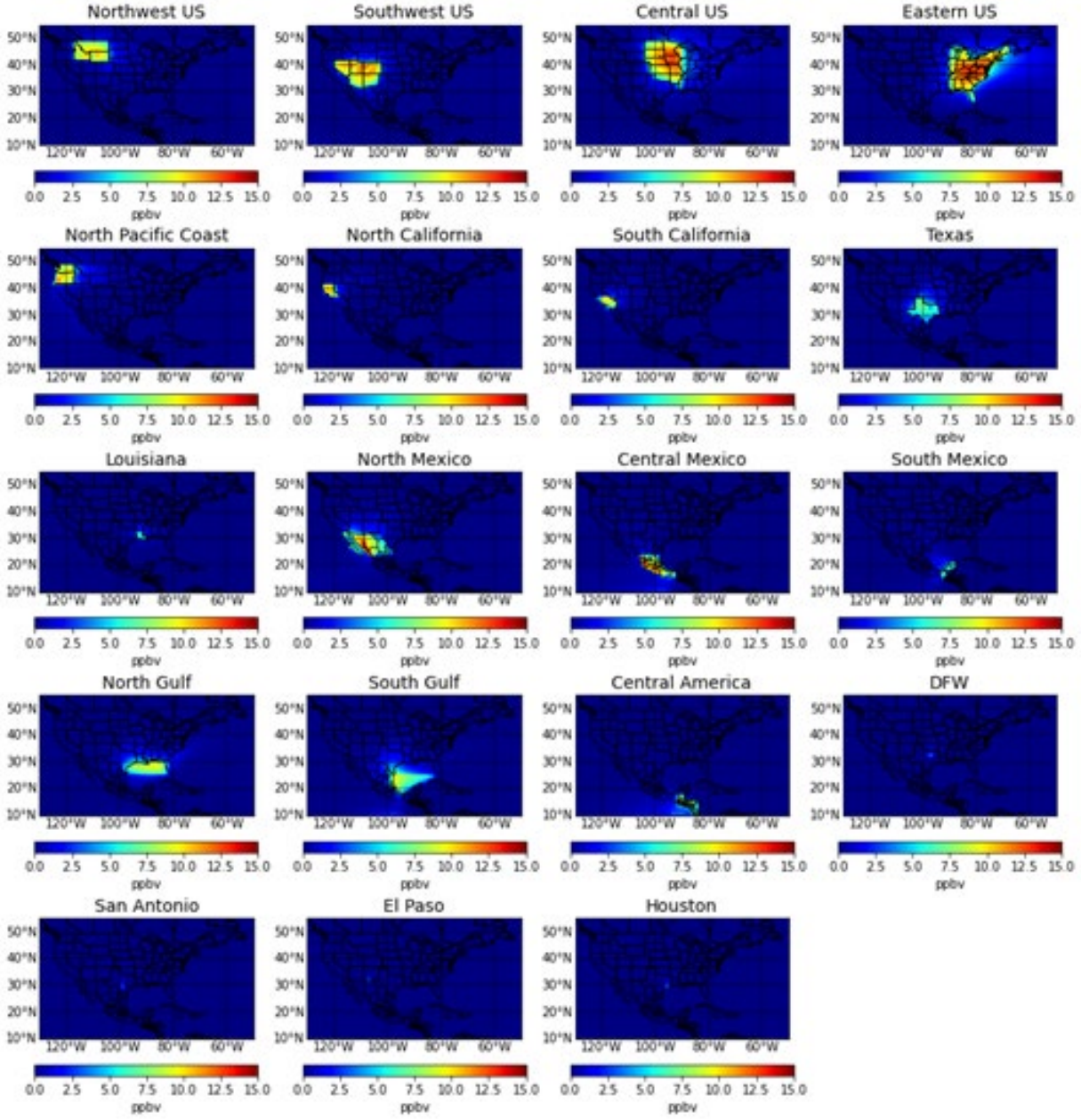

Figure 2. The 7-year average spatial distributions of the 19 passive tracers during summertime.

eliminating the effects of source region area on the value of passive tracers' concentrations, the mixing ratio of each passive tracer was normalized at the targeted grids (i.e. the grids containing the sampling sites in Houston and El Paso). Figure 3 shows the result of a select

number of normalized tracer mixing ratios for each measurement site during its respective sampling period. To determine if the passive tracer had the potential to influence the site of interest during a perceived event, we tested many methodologies, such as the prior work from Wang S. et al. [2018] in which the long-range transport events of Mexican pollutants were determined by the daily mean mixing ratio of the Mexican passive tracer exceeding 75% compared to its 14-year average. Given the different components of this study, such as having a smaller study area or a shorter climatological study period, it was determined that a new methodology for identifying potential tracer influence is needed to appropriately categorize influence of the passive tracers for this study.

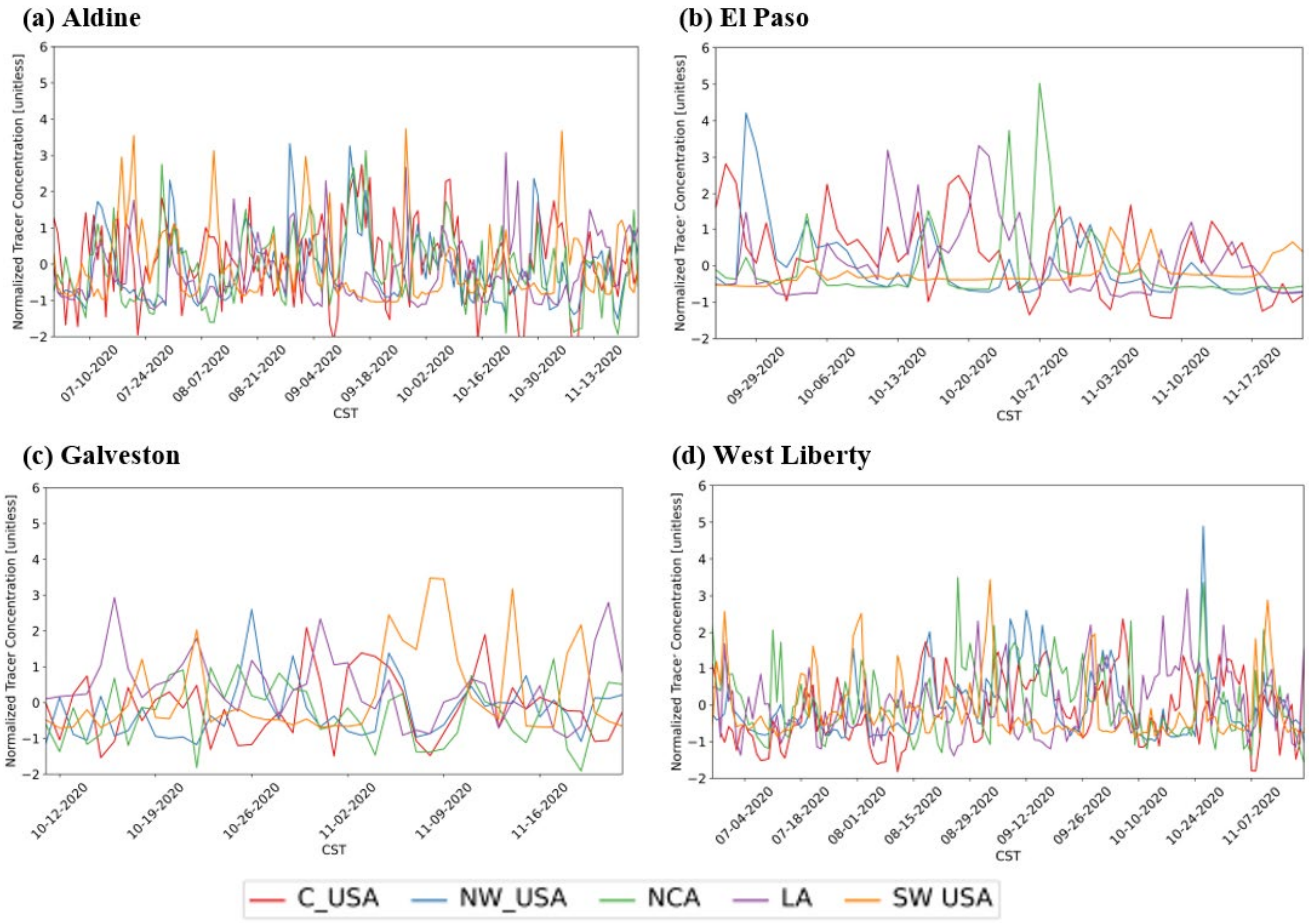

Figure 3. Time series of select normalized tracers (C_USA: Central USA, NW_USA: Northwest USA, NCA: Northern California, LA: Louisiana, SW_USA: Southwest USA) affecting the (a) Aldine, (b) El Paso, (c) Galveston, (d) West Liberty targeted grids.

4. Results

4.1. Time Series Data

4.1.1. Aerosol Absorption and Scattering Coefficients

The $(BC)^2$ monitoring sites operated in 2020. Figures in this section portray the measured aerosol absorption and scattering coefficients for each site. As each site had a different operating schedule, the time series vary by site. These figures combine to highlight the high data recovery for the $(BC)^2$ network. They also illustrate the wide range in the absorption and scattering coefficients for each site. A wider range in absorption coefficient can be seen at the more urban sites, Aldine and El Paso, while a narrower range is evident at Houston's upwind site, West Liberty. Galveston is dominated by lower absorption coefficients until the mid-November biomass burning events. A higher background absorption coefficient is evident at the more urban sites (Aldine and El Paso) which is likely associated with a consistent traffic source of black carbon.

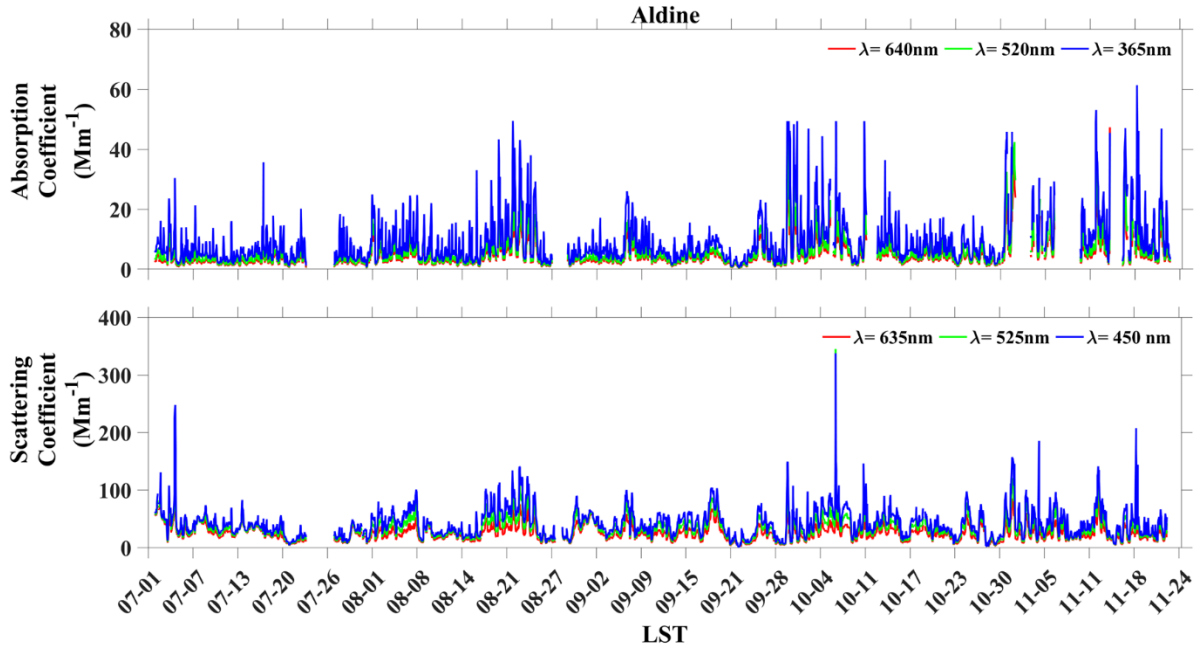

Figure 4. Time series (hourly average) of absorption coefficient (σ_{abs}) and scattering coefficient (σ_{scat}) observed at Aldine during the month of July through November 2020.

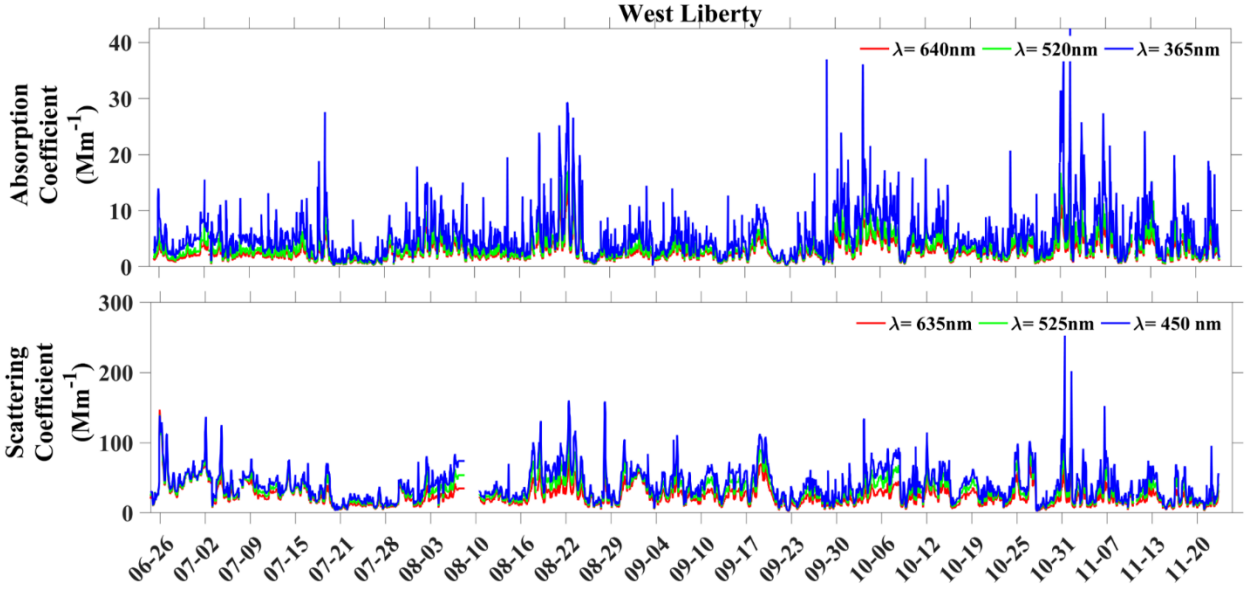

Figure 5. Time series (hourly average) of absorption coefficient (σ_{abs}) and scattering coefficient (σ_{scat}) observed at West Liberty during the month of June through November 2020.

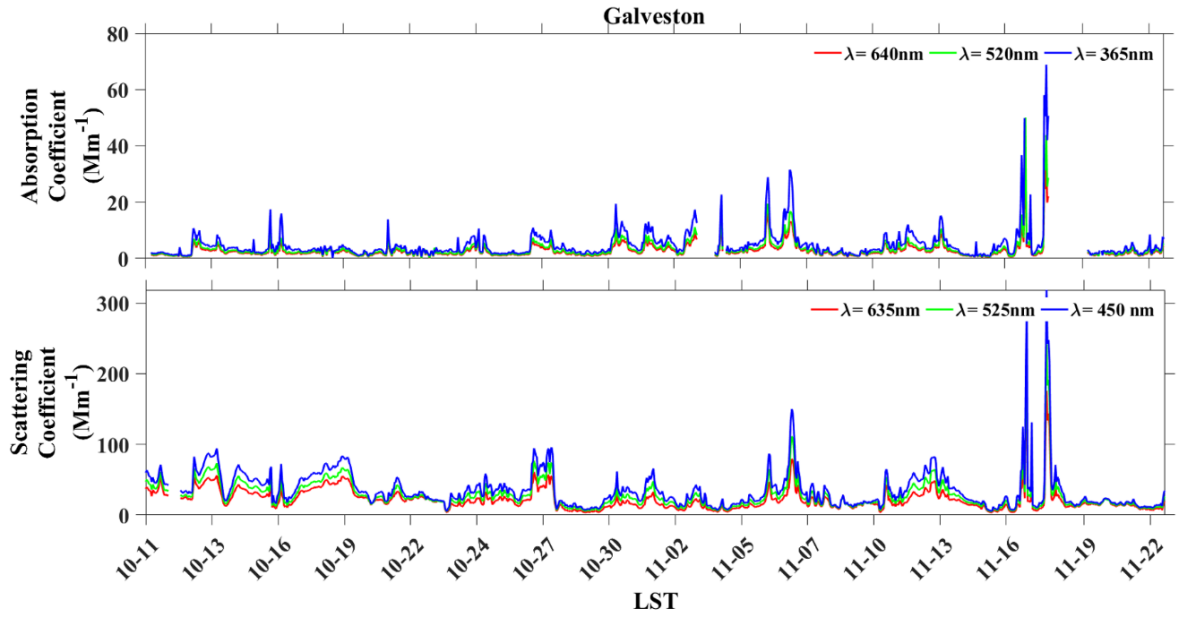

Figure 6. Time series (hourly average) of absorption coefficient (σabs) and scattering coefficient (σscat) observed at Galveston during the month of October through November 2020.

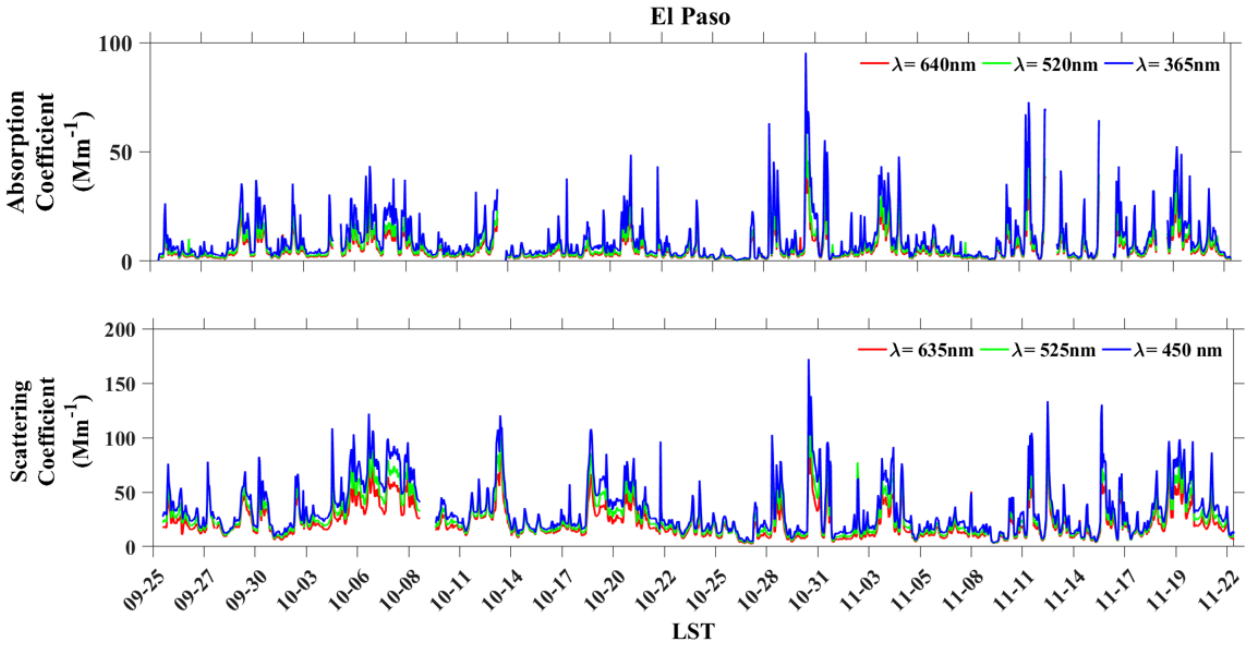

Figure 7. Time series (hourly average) of absorption coefficient (σabs) and scattering coefficient (σscat) observed at El Paso during the month of October through November 2020.

The diel variation plots below illustrate the time-of-day impacts of absorbing and scattering aerosol. All days are averaged together here, although, some change might be expected between weekday and weekend. The more urban sites (Aldine and El Paso), have a more defined rush hour impact on absorption, likely from motor vehicle exhaust. All the sites do show mid-day decreases with the increasing boundary height. Galveston and El Paso are an interesting comparison in evening aerosol impacts. Galveston has no increase in aerosol absorption in the evening which is likely due to the on-shore breeze in the evening which switches to off-shore breeze in the early morning. This change in marine (on-shore) and continental (off-shore) is clearly seen in the hourly averages for the aerosol absorption coefficient in Galveston. In contrast, El Paso has a very strong increase in aerosol absorption in the evening. This may be due to the evening decrease in boundary height which could trap emissions at the surface, while the local mountains limit horizontal transport. It is not clear what is driving the later night decrease in absorption. More work is needed to understand these local atmospheric dynamics in El Paso and the Houston sites. These are the baseline conditions onto which wildfire and dust events are overlaid.

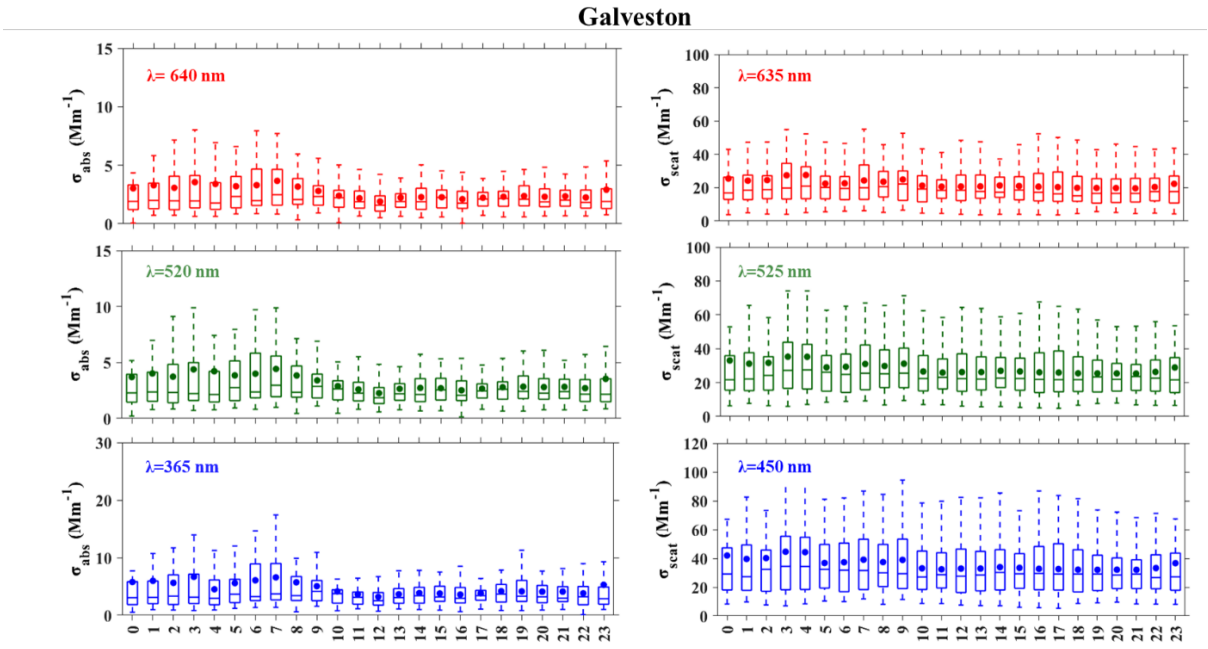

Figure 8. Diel variation in absorption coefficient (σabs) and scattering coefficient (σscat) observed at Galveston for October-November. The circle represents the average, and the line represents the median values of σabs and σscat, respectively.

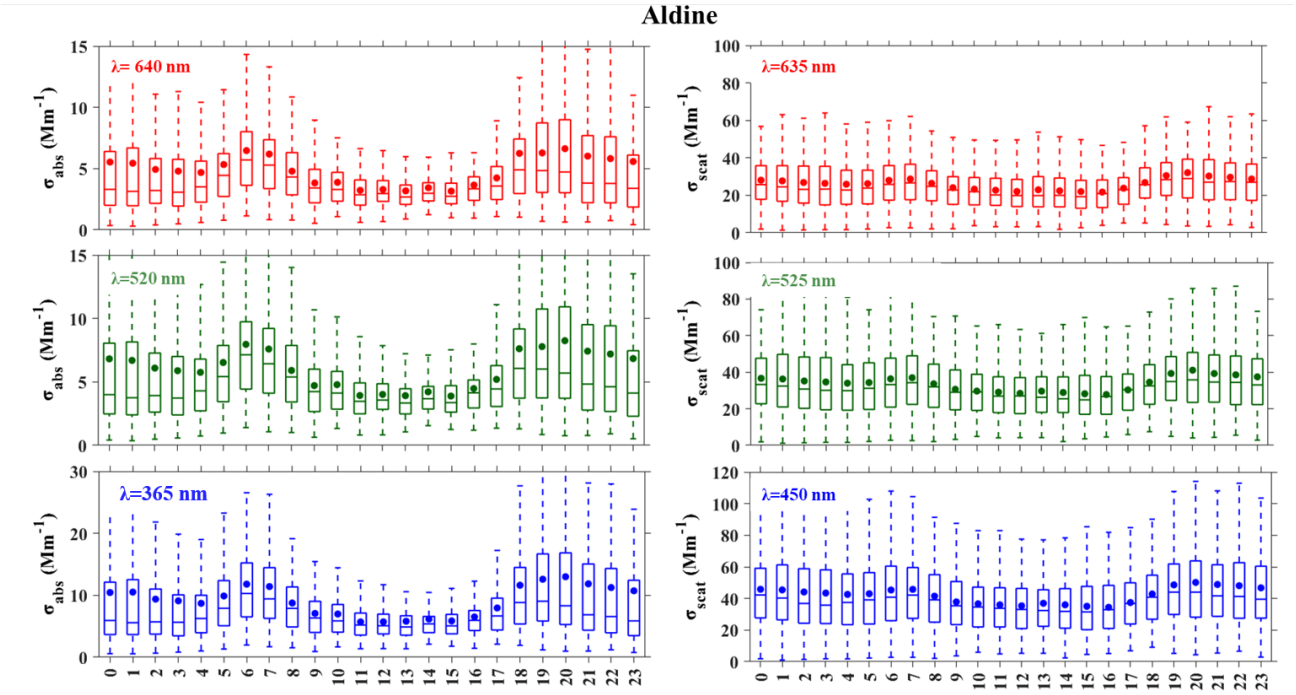

Figure 9. Diel variation in absorption coefficient (σabs) and scattering coefficient (σscat) observed at Aldine. The circle represents the average, and the line represents the median values of σ_{abs} and σ_{scat}, respectively.

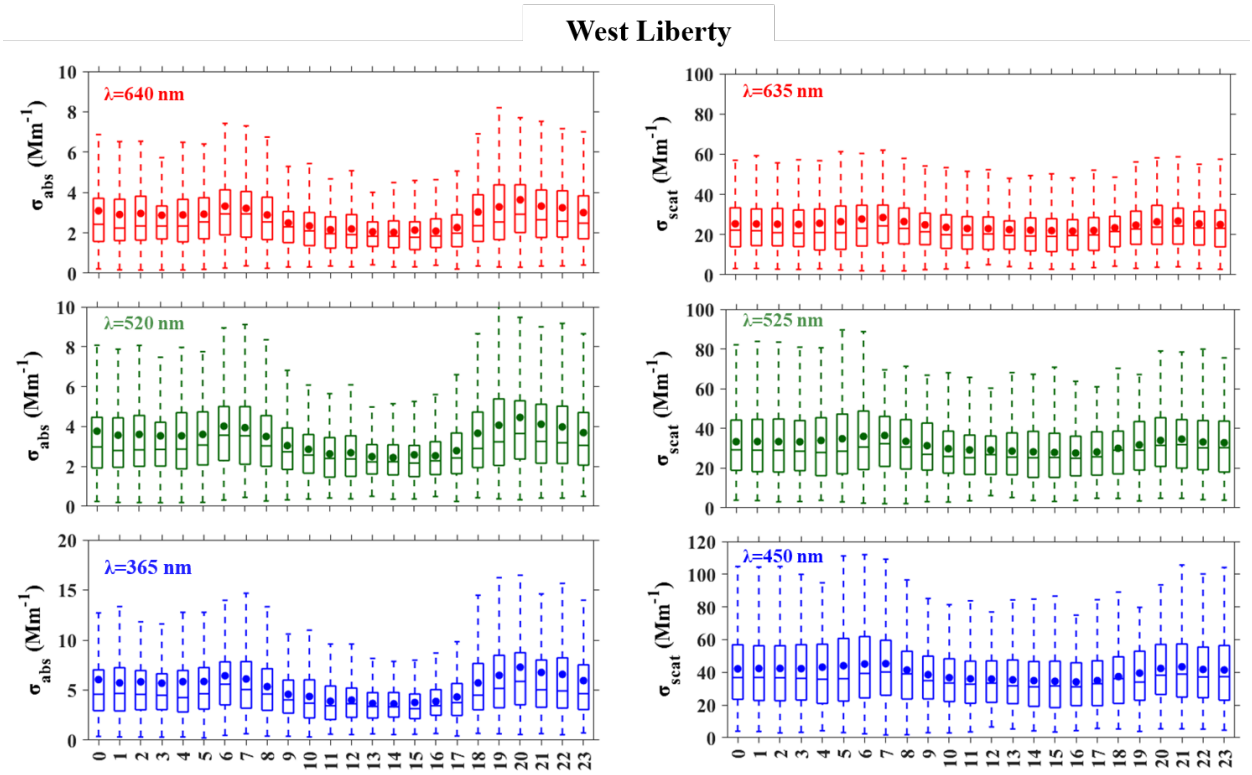

Figure 10. Diel variation in absorption coefficient (σabs) and scattering coefficient (σscat) observed at West Liberty. The circle represents the average, and the line represents the median values of σ_{abs} and σ_{scat}, respectively.

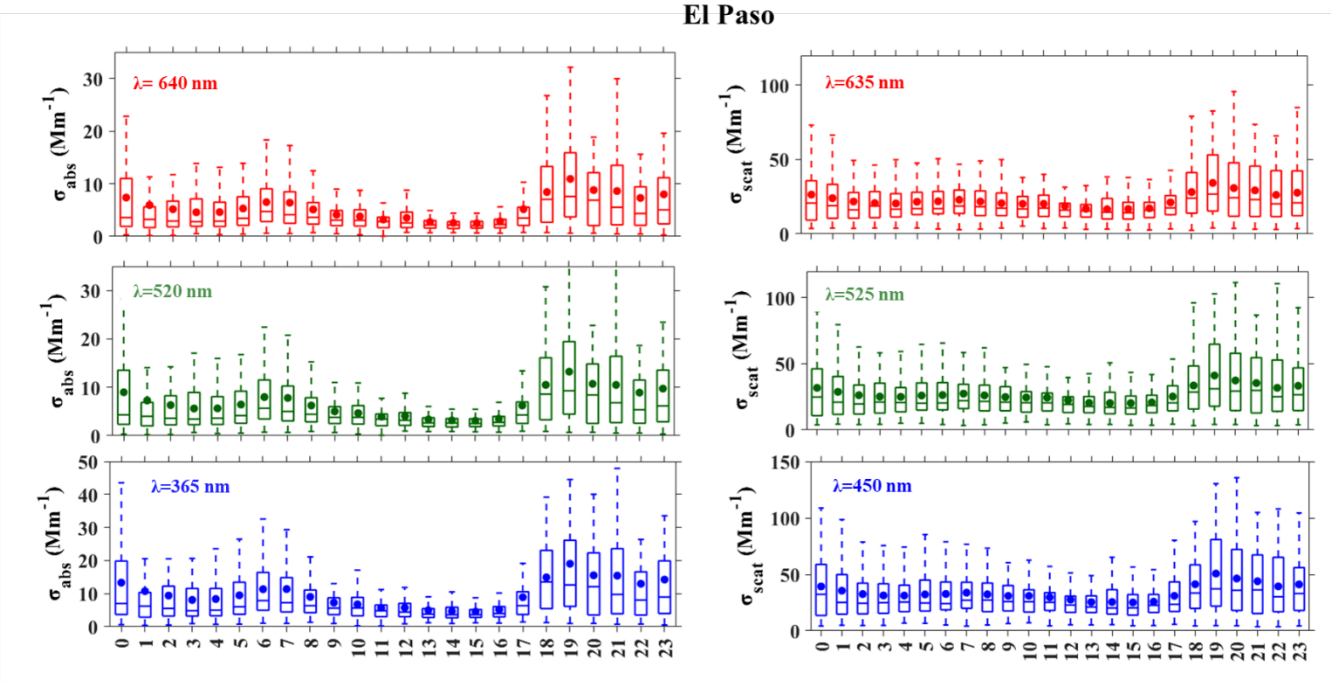

Figure 11. Diel variation in absorption coefficient (σabs) and scattering coefficient (σscat) observed at El Paso. The circle represents the average, and the line represents the median values of σ_{abs} and σ_{scat}, respectively.

4.1.2. Optical properties – Ångström exponents and single scattering albedo

The calculated AAE and SAE show much more limited variability than the corresponding absorption and scattering coefficients. By removing the high variability associated with the concentration-based measurements, the impact of biomass burning, and dust can be seen through the noise. The site figures below include yellow and blue shaded regions for dust and biomass burning influence, respectively. The SSA is also depicted as a time series. This value indicates the relative importance of scattering (high SSA) vs absorption (lower SSA). For West Liberty, the SSA as close to one in the early campaign, dipped during a biomass burning event in early October and then gradually decreased near the end of the campaign in November. This trend was similar in Aldine, however, the overall SSA was lower, indicative of the greater black carbon concentrations in this more urban location. El Paso had an even lower average SSA, while Galveston was dominated by scattering aerosol and had a very high SSA due to the influence of marine aerosols.

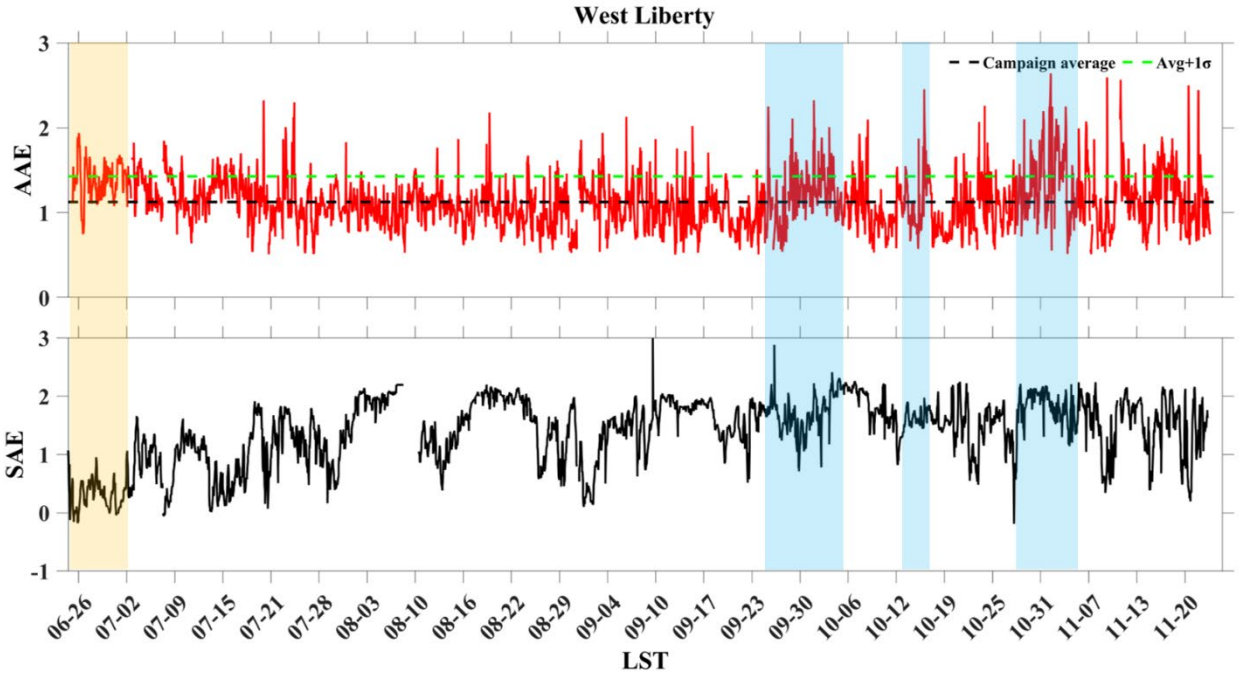

Figure 12. Time series (hourly average) of Absorption Ångström Exponent (AAE) and Scattering Ångström Exponent (SAE) observed at West Liberty during the month of June through November 2020.

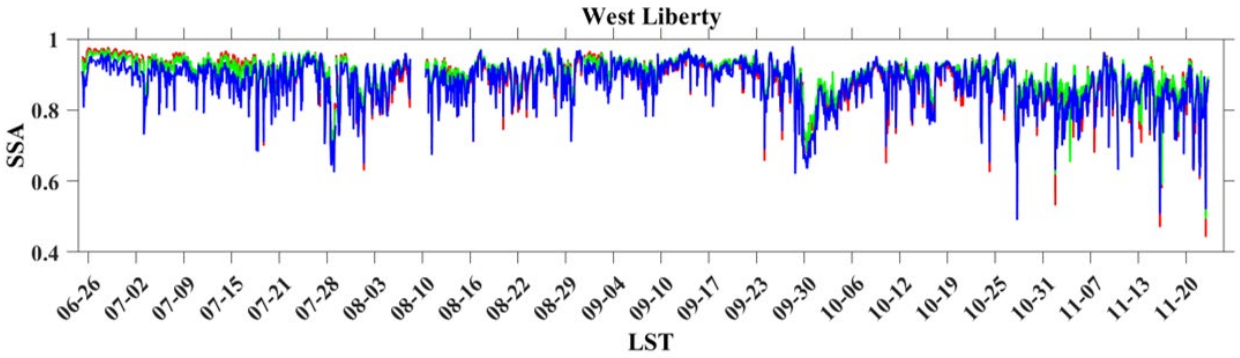

Figure 13. Time series (hourly average) of Single Scattering Albedo (SSA) observed at West Liberty during the month of June through November 2020.

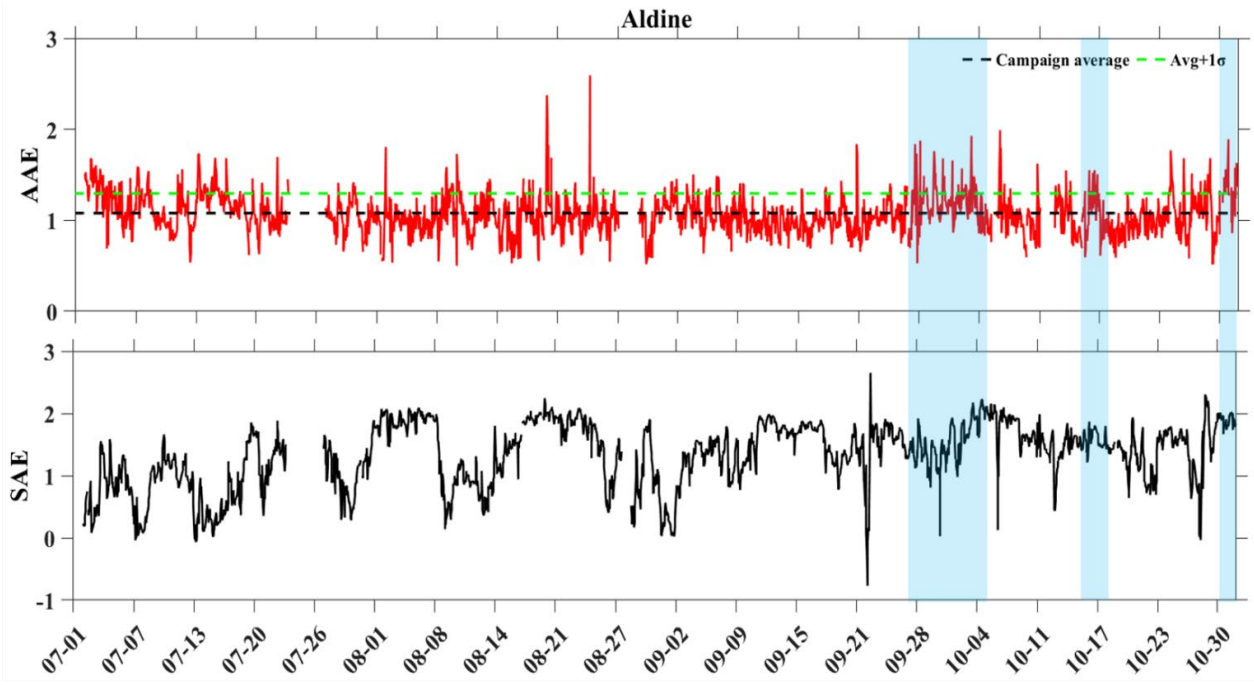

Figure 14. Time series (hourly average) of Absorption Ångström Exponent (AAE) and Scattering Ångström Exponent (SAE) observed at Aldine during the month of July through November 2020.

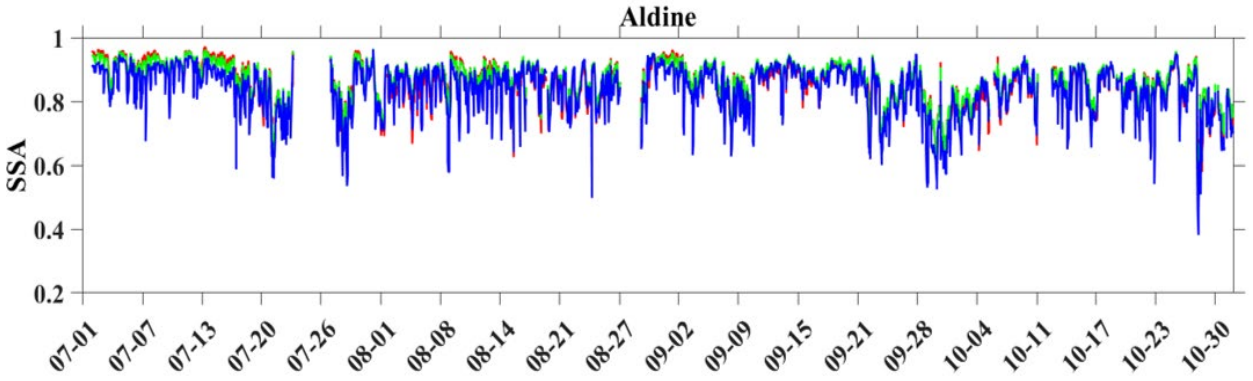

Figure 15. Time series (hourly average) of Single Scattering Albedo (SSA) observed at Aldine during the month of July through November 2020.

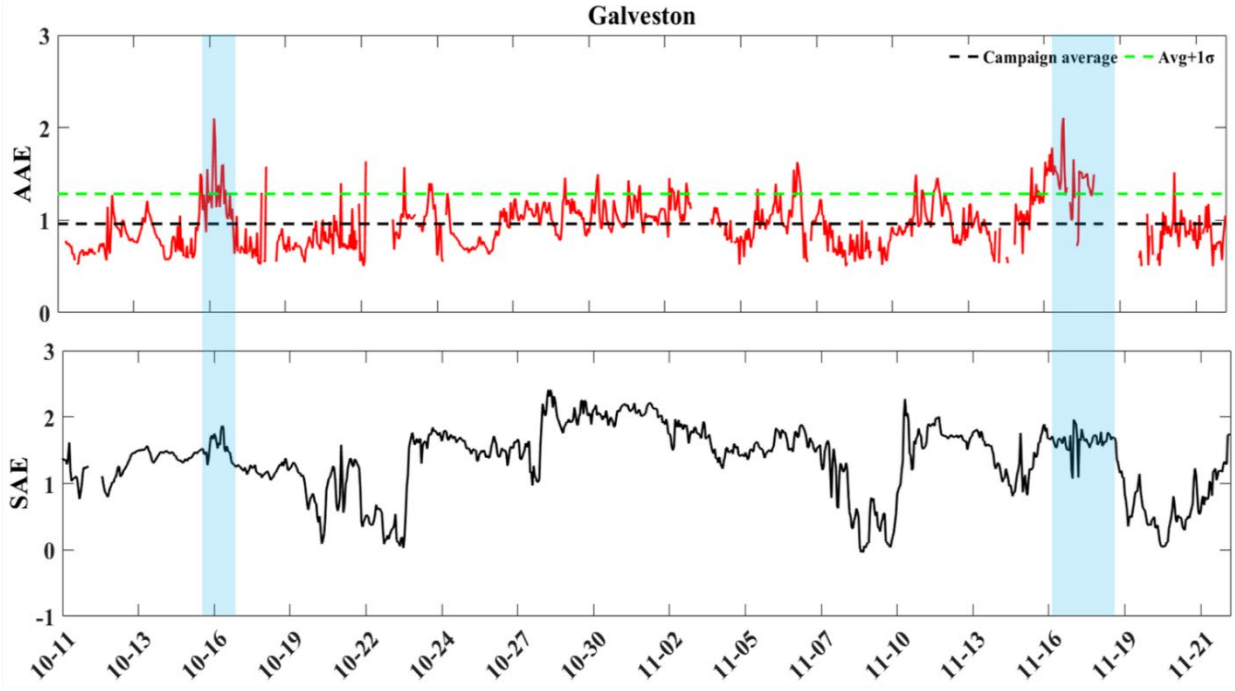

Figure 16. Time series (hourly average) of Absorption Ångström Exponent (AAE) and Scattering Ångström Exponent (SAE) observed at Galveston during the month of October

through November 2020. The missing data in November is associated with a delay in the filter change.

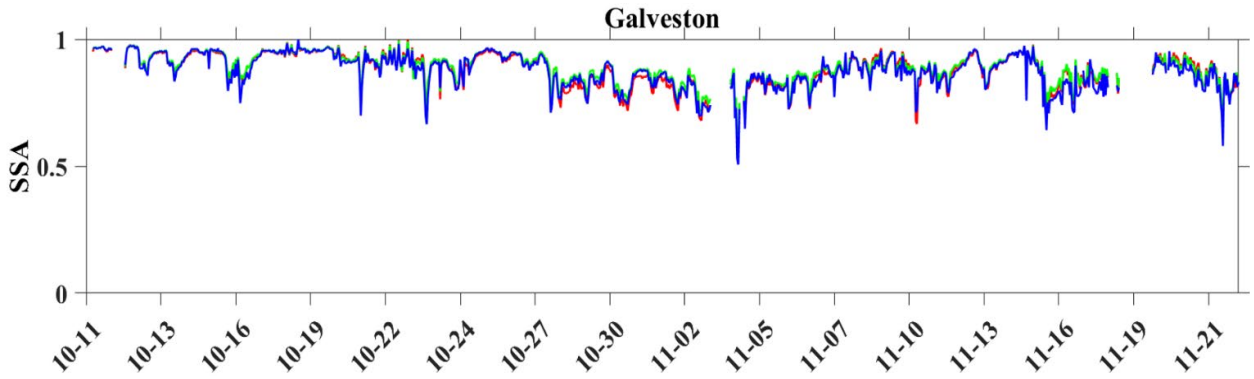

Figure 17. Time series (hourly average) of Single Scattering Albedo (SSA) observed at Galveston during the month of October through November 2020.

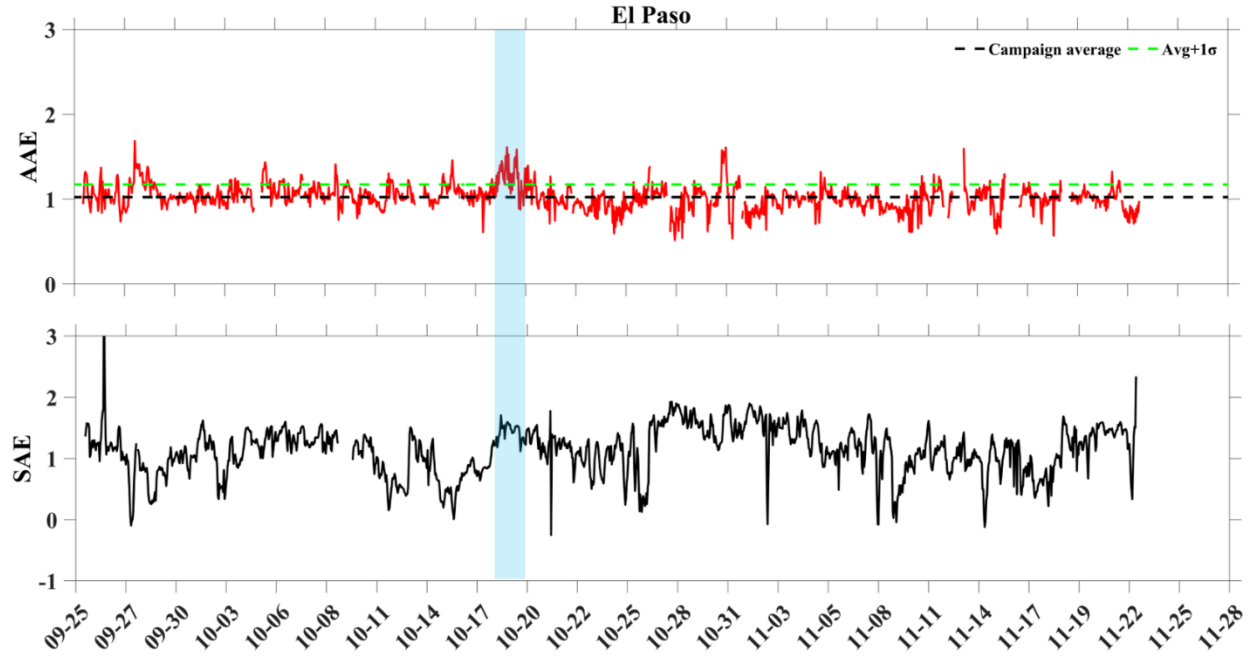

Figure 18. Time series (hourly average) of Absorption Ångström Exponent (AAE) and Scattering Ångström Exponent (SAE) observed at El Paso during the month of September through November 2020.

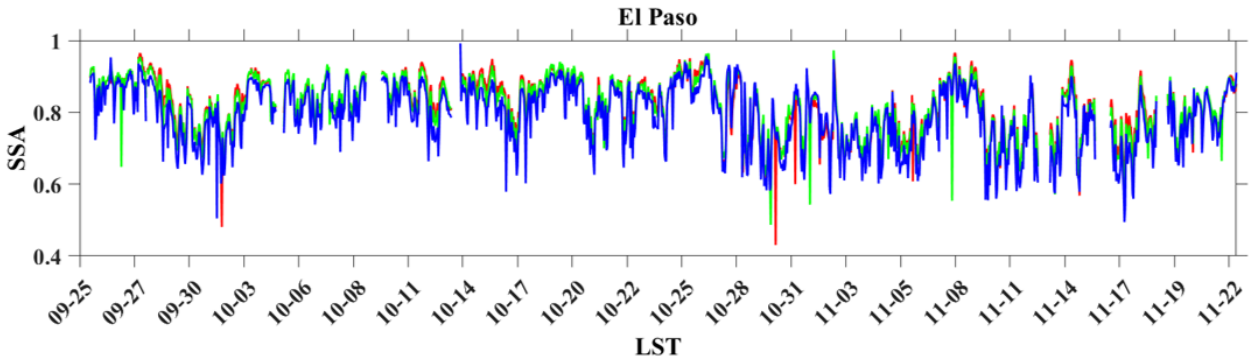

Figure 19. Time series (hourly average) of Single Scattering Albedo (SSA) observed at El Paso during the month of September through November 2020.

4.1.3. Site statistics

The site statistics reveal differences in the baseline conditions at each site. From the absorption coefficient, which varies with the concentration of absorbing aerosol, the two most urban-influenced sites, UTEP in El Paso and Aldine in Houston, have the highest campaign average. West Liberty and Galveston are distinctly lower than their more urban counterparts. The AAE is highest at West Liberty for this campaign, while Galveston has an average AAE for Oct and Nov of < 1. An AAE average below 1 has previously been reported for clean marine conditions (e.g. low absorption) [41].

The scattering coefficients and SAE are similar across the sites, however, it should be remembered that West Liberty and Aldine include the Saharan dust season in July, while Galveston and El Paso do not include a full season.

For the 2019 vs 2020 comparison, both absorption and scattering coefficients were lower in 2019, while the AAE and SAE were higher in 2019.

Table 1. Campaign averages for aerosol optical properties by site. All are listed as average ± standard deviation. σ_{abs} and σ_{scat} represents absorption and scattering coefficients, respectively measured at three different wavelengths.

Site	σ_{abs_640}	σ_{abs_520}	σ_{abs_365}	AAE	σ_{scat_635}	σ_{scat_525}	σ_{scat_450}	SAE
West Liberty	2.77 ± 1.96	3.38 ± 2.39	5.33 ± 4.15	1.13 ± 0.3	24.7 ± 15.55	31.86 ± 18.85	39.84 ± 23.57	1.40 ± 0.56
Aldine	4.44 ±3.71	5.45 ± 4.63	8.24 ± 7.59	1.07 ± 0.21	26.21 ± 15.64	33.74 ± 19.92	41.80 ± 24.59	1.33 ± 0.52
Galveston	2.58 ± 1.89	3.09 ± 2.33	4.46 ± 3.8	0.94 ± 0.32	22.56 ± 12.87	28.9 ± 16.51	36.59 ± 21.47	1.40 ± 0.49
El Paso (2019)	2.6 ± 3.3	3.3 ± 3.3	4.8 ± 4.7	1.1 ± 0.1	10.1 ± 10.5	13.6 ± 11.5	18.3 ± 12.6	1.4 ± 0.5
El Paso (2020)	5.37 ± 6.07	6.54 ± 7.38	9.53 ± 10.76	1.04 ± 0.2	22.45 ± 15.89	27.05 ± 19.49	33.45 ± 24.26	1.13 ± 0.4

Table 2. Monthly averages of aerosol optical properties by site. [1] incomplete month. σ_{abs} and σ_{scat} represents absorption and scattering coefficients, respectively measured at three different wavelengths.

Site	Month	σ_{abs_640}	σ_{abs_520}	σ_{abs_365}	AAE	σ_{scat_635}	σ_{scat_525}	σ_{scat_450}	SAE
West Liberty	Jun-20[1]	1.85 ± 0.77	2.38 ± 1.08	3.97 ± 2.13	1.30 ± 0.25	40.89 ± 28.15	42.71 ± 27.49	46.32 ± 28.24	0.51 ± 0.52
West Liberty	Jul-20	2.09 ± 1.4	2.58 ± 1.71	4.15 ± 2.7	1.21 ± 0.26	25.64 ± 15.98	29.28 ± 17.06	34.01 ± 19.24	0.92 ± 0.48
West Liberty	Aug-20	3.12 ± 2.36	3.75 ± 2.85	5.68 ± 4.56	1.04 ± 0.23	24.98 ± 13.2	34.72 ± 19.8	45.48 ± 27.07	1.61 ± 0.46
West Liberty	Sep-20	2.36 ± 1.54	2.86 ± 1.89	4.36 ± 3.07	1.05 ± 0.27	24.51 ± 14.12	32.26 ± 17.06	40.45 ± 20.68	1.51 ± 0.43
West Liberty	Oct-20	3.26 ± 1.94	3.97 ± 2.38	6.19 ± 4.13	1.11 ± 0.31	23.46 ± 12.51	32.47 ± 16.94	42.08 ± 22	1.68 ± 0.38
West Liberty	Nov-20[1]	3.38 ± 2.28	4.18 ± 2.81	7.03 ± 5.77	1.22 ± 0.4	19.62 ± 13.81	26.78 ± 19.16	34.58 ± 25.43	1.54 ± 0.47
Aldine	Jul-20	3.10 ± 1.99	3.85 ± 2.45	5.85 ± 3.74	1.14 ± 0.21	27.84 ± 15.73	31.91 ± 18.07	36.78 ± 21.11	0.86 ± 0.45
Aldine	Aug-20	4.91 ± 3.94	5.99 ± 4.84	8.91 ± 7.68	1.03 ± 0.22	25.87 ± 13	35.04 ± 19.38	44.85 ± 26.18	1.46 ± 0.52
Aldine	Sep-20	4.14 ± 3.71	5.08 ± 4.69	7.68 ± 7.94	1.05 ± 0.18	25.41 ± 15.3	32.75 ± 18.75	40.39 ± 22.59	1.38 ± 0.44

Aldine	Oct-20	5.49 ± 4.24	6.74 ± 5.32	10.31 ± 8.92	1.07 ± 0.23	25.94 ± 17.96	35.01 ± 22.68	44.46 ± 26.69	1.56 ± 0.36
Galveston	Oct-20[1]	2.19 ± 1.31	2.59 ± 1.6	3.65 ± 2.57	0.92 ± 0.37	25.65 ± 13.14	32.28 ± 16.31	40.57 ± 20.75	1.37 ± 0.48
Galveston	Nov-20[1]	3.19 ± 2.4	3.86 ± 2.97	5.69 ± 4.89	0.96 ± 0.22	18.26 ± 11.13	24.17 ± 15.6	31.03 ± 21.2	1.44 ± 0.5
El Paso	Sep-20[1]	4.31 ± 4.36	5.29 ± 5.26	7.66 ± 7.49	1.10 ± 0.20	23.12 ± 11.75	26.90 ± 12.69	32.41 ± 14.99	0.99 ± 0.46
El Paso	Oct-20	5.48 ± 5.99	6.66 ± 7.27	9.76 ± 10.55	1.05 ± 0.19	25.12 ± 16.47	30.42 ± 20.52	37.72 ± 25.79	1.14 ± 0.39
El Paso	Nov-20[1]	5.56 ± 6.73	6.78 ± 8.22	9.77 ± 12.12	0.98 ± 0.19	16.86 ± 14.5	20.34 ± 17.56	25.25 ± 21.49	1.16 ± 0.38

4.1.4. Filter-based PM composition

The filters collected at each of the four sites were all analyzed for OC, EC, inorganic ions (K^+, Na^+, Ca^{++}, Mg^+, NH_4^+, SO_4^{--}, NO_3^-, NO_2^-, Cl^-) and methane sulfonic acid (MSA). This analysis can reveal source impacts and potentially quantify source contributions to PM mass. Filters were collected periodically to characterize events and local background at West Liberty and Aldine. As the campaign started later in the season at El Paso and Galveston, filters were collected for the entire available time in October (October 12-31 for Galveston and September 25 – November 2 for El Paso). However, for Galveston, the inorganic ions were below the detection limit except for October 13 – 20, 2020. Although OC and EC were measured for all filters, only the dates which had all data above detection limit were included in the figures.

The Na^+ is acting as a tracer for marine influence at West Liberty and Aldine during the Saharan dust events in late June and early July. As the inorganic fraction that we are measuring is water-soluble, we do not measure the mineral component of the dust unless it extracts into water. The Na^+ is a marker for sea salt and likely is co-transported with the Saharan dust as it travels across the Atlantic and the Gulf of Mexico. Galveston is directly on the Gulf and has this marine/sea salt signal in October as well. The SO_4^{--} is also enhanced in late June and early July at West Liberty, however, marine sources have minimal impact on fine SO_4^{--} in the Houston area. Sea salt calculations confirm that the greatest influence of marine conditions was late June/early July.

Although K^+ is often a useful tracer for biomass burning, there is a unique source that is apparent in the West Liberty and Aldine datasets: Fourth of July fireworks. An increase in PM and in potassium as previously been reported for the impact of fireworks on local air quality [42]. Fireworks are clearly evident on July 3 and 4.

Early October has higher measured EC concentrations at Aldine and West Liberty. The OC increases over the campaign, with lows in June/July and highs in early October at both sites. Early October had higher AAE, high SAE, all indicating biomass burning influence. Similar to the absorption coefficient (which is driven by EC absorption), the EC is higher in El Paso and Aldine than in West Liberty and Galveston.

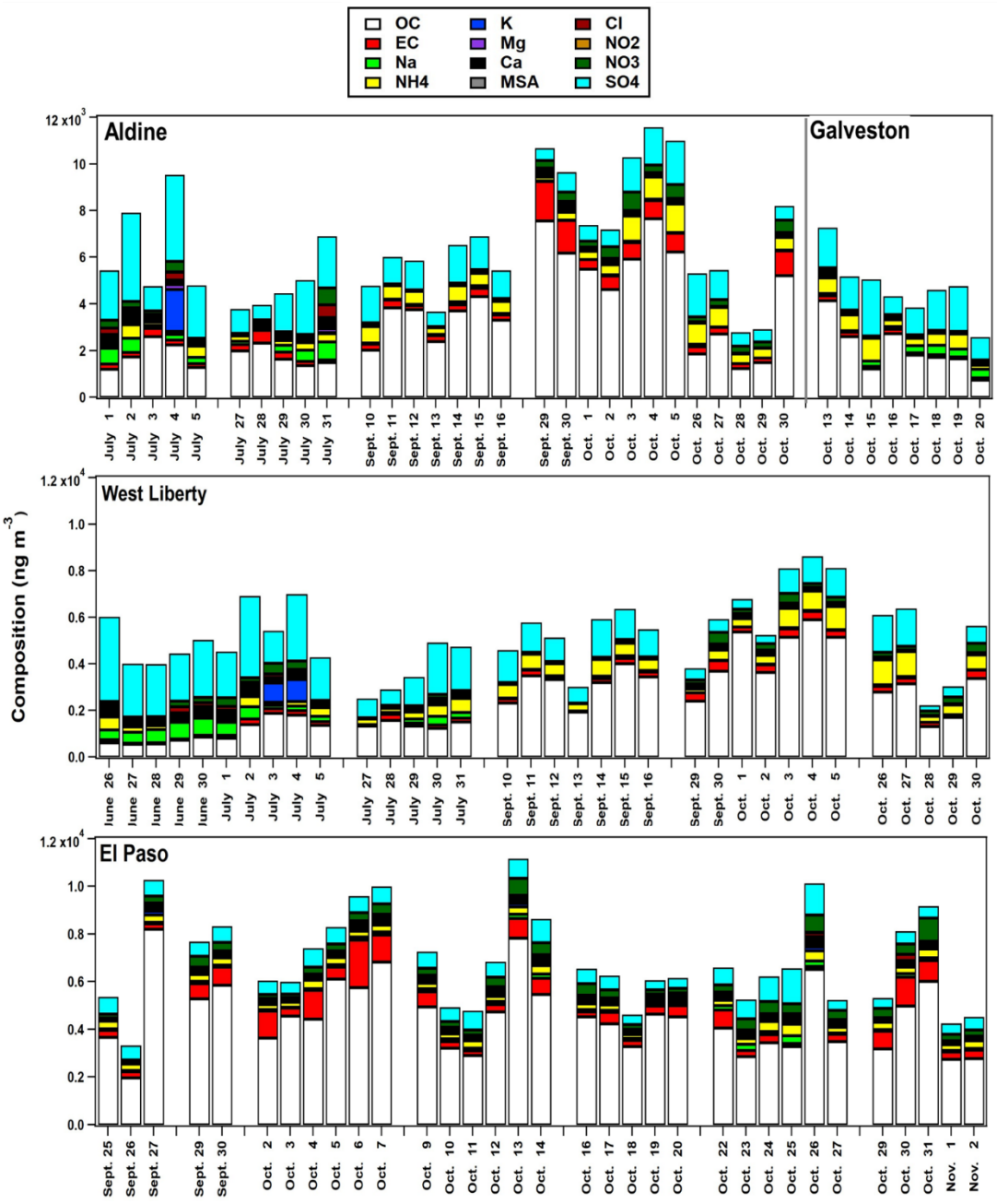

Figure 20. Time series of aerosol composition by site. This composition does not include insoluble minerals. Only dates with most of the data above detection limit were included in the figure.

Select days were chosen for radiocarbon analysis. This was based off the AAE events, supporting data, and the availability of filters. Additional days were analyzed around events, if available. The filter analysis does reveal some of the baseline differences among the sites. For example, the baseline fraction contemporary (which would include both biomass burning and biogenic sources) is well above 60% for the Houston sites, while El Paso routinely dips below 50%. Previous radiocarbon analysis for Houston in Sept 2013 had lower contemporary carbon at the downtown site (Moody Tower) and higher contemporary carbon south of the downtown (Manvel Croix) [43, 44].

Additionally, for the periods of biomass burning event in West Liberty and Aldine (Sept 29- Oct 04), the fraction contemporary increases by ~ 20% from Sept 30 to Oct 1 at West Liberty and 15% at Aldine. Similar to the AAE, the fraction contemporary for Galveston and West Liberty are higher than Aldine. For the biomass burning event in El Paso in mid-October, the fraction contemporary carbon increases by nearly 30%, while the fraction contemporary during the dust event (Sept 29), was < 50%.

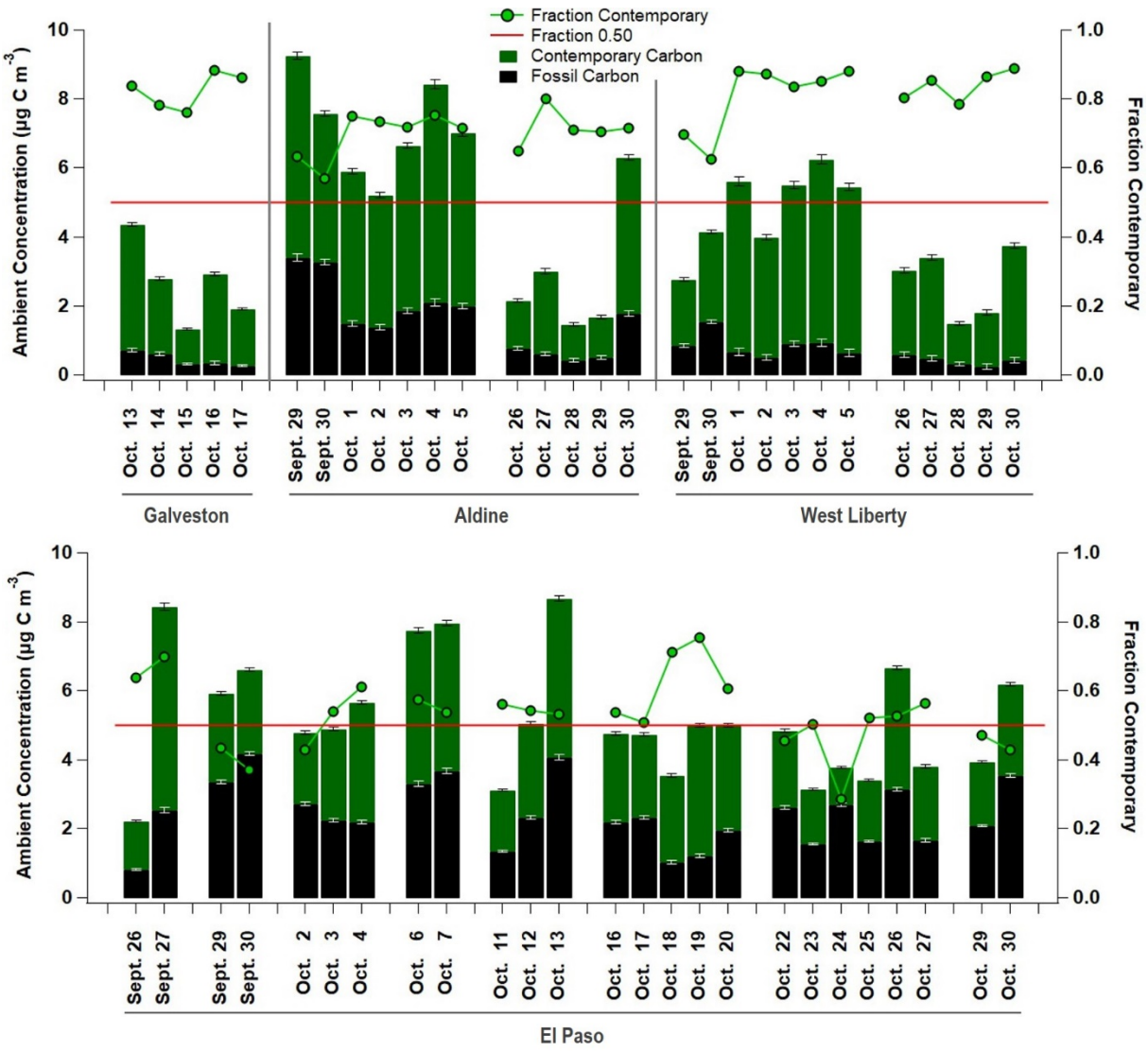

Figure 21. Filter-based radiocarbon measurements from West Liberty, Aldine, and Galveston (top panel) and El Paso (bottom panel).

Because the contemporary carbon includes both biogenic carbon (e.g. secondary organic aerosol from biogenic precursors) and biomass burning carbon, the relationship with soluble potassium can be used to estimate the carbon (OC + EC) from biomass burning alone. This relationship varies by site, with the TOC to potassium ratio at 56 for Aldine, 40 for West Liberty, 37 for Galveston and 27 for El Paso. A previous TCEQ study (San Antonio Field Study PGA Number: 582-18-82485-03 https://www.tceq.texas.gov/airquality/airmod/project/pj_report_oth.html) reported a TOC:K ratio of 10 for San Antonio in May 2017. These ratios can be used to calculate the TOC associated with biomass burning for these events, but more results are needed to determine if these values vary by season or by site. The source signature can cause a change in this ratio (e.g. forest fires vs. grass fires) and long-range transport may decrease the ratio due to loss of OC by reaction and volatilization. Only the days when the nss-potassium is above MDL are included in the correlation. In future years, this dataset will grow to allow more detailed characterization and investigation of the impact of sources and processes on this relationship.

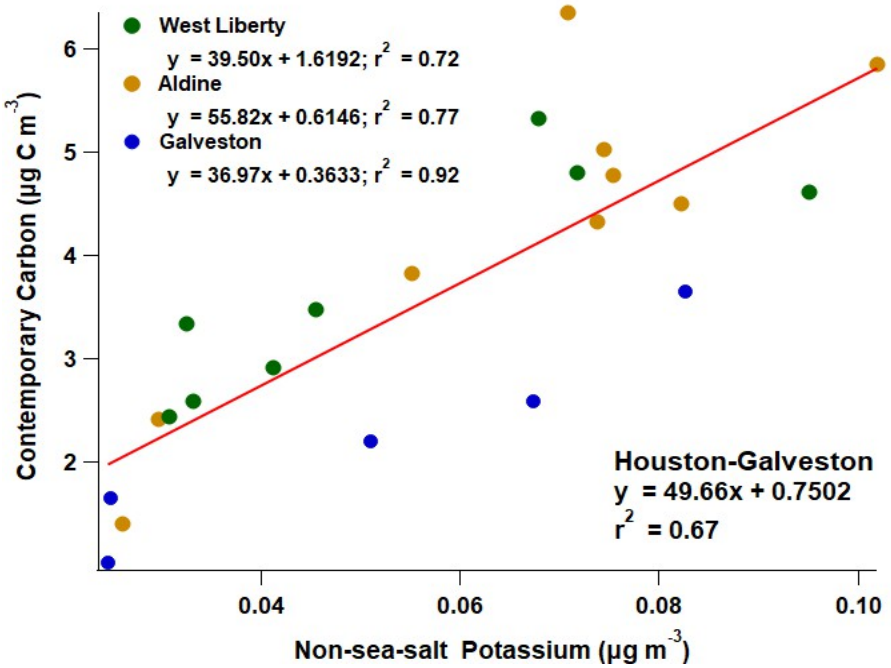

Figure 22. Filter-based potassium vs contemporary carbon across the three Houston- Galveston sites (n = 22).

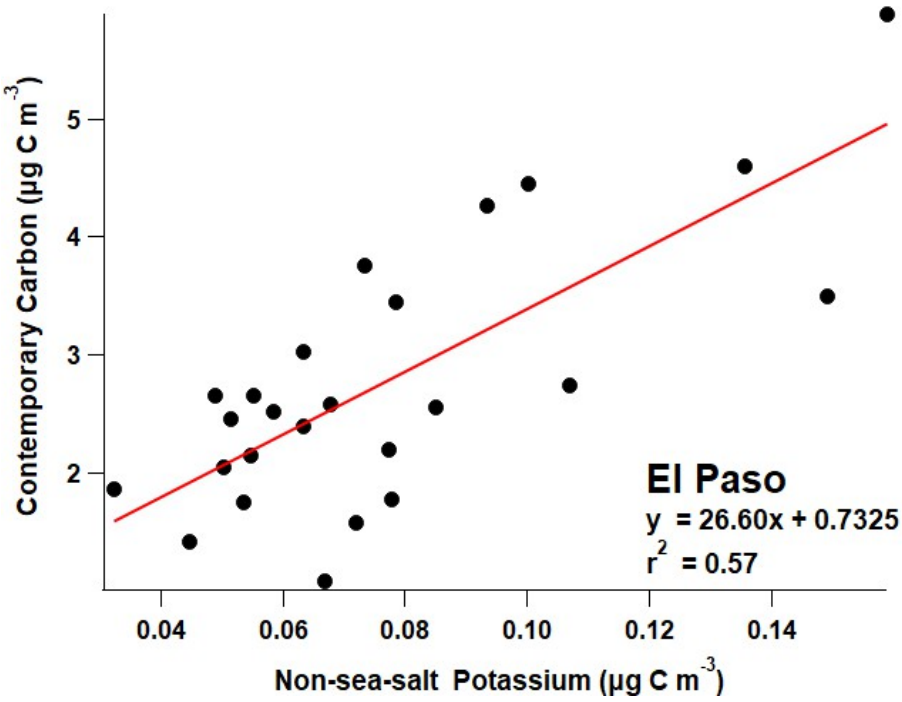

Figure 23. Filter-based Potassium vs contemporary carbon for El Paso (n = 25).

4.1.5. Supporting measurements including Trace Gas and realtime PM

To improve aerosol classification and begin to understand potential impacts of fire and dust events, select trace gas and PM are included in the campaign analysis. The source of the data varies by site, with TCEQ – CAMS data available for West Liberty (CO and NO_2), Aldine (NO_2), El Paso (CO, NO_2, PM_{10}, and $PM_{2.5}$). As it was not available at the adjacent TCEQ site, the (BC)^2 trailers included CO measurement at both Aldine and Galveston. The source of the supporting measurements is included in each figure. The urban vs background assignment is also clear in the trace gas data, with the max CO and NO_2 values at Aldine and El Paso distinctly higher than the background sites (West Liberty and Galveston).

The comparison between the PM_{10} and $PM_{2.5}$ is particularly useful at El Paso where frequent dust events are observed. The early October increases in AAE were accompanied by decreases in

SAE and increases in both PM_{10} and $PM_{2.5}$, while the mid-October increase in AAE only showed an increase in $PM_{2.5}$ and little change in SAE or PM_{10}. These all confirm biomass burning or wildfire impacts rather than a dust event. The PM_{10} time series does show events that only impact the coarse fraction (e.g. no discernable increase in $PM_{2.5}$) and frequent events that may be of interest.

Trace gas data used for West Liberty is from the TCEQ site is from the HNET dataset which is at 95% QAQC, but may still include artifacts that need to be removed prior to finalization and publication.

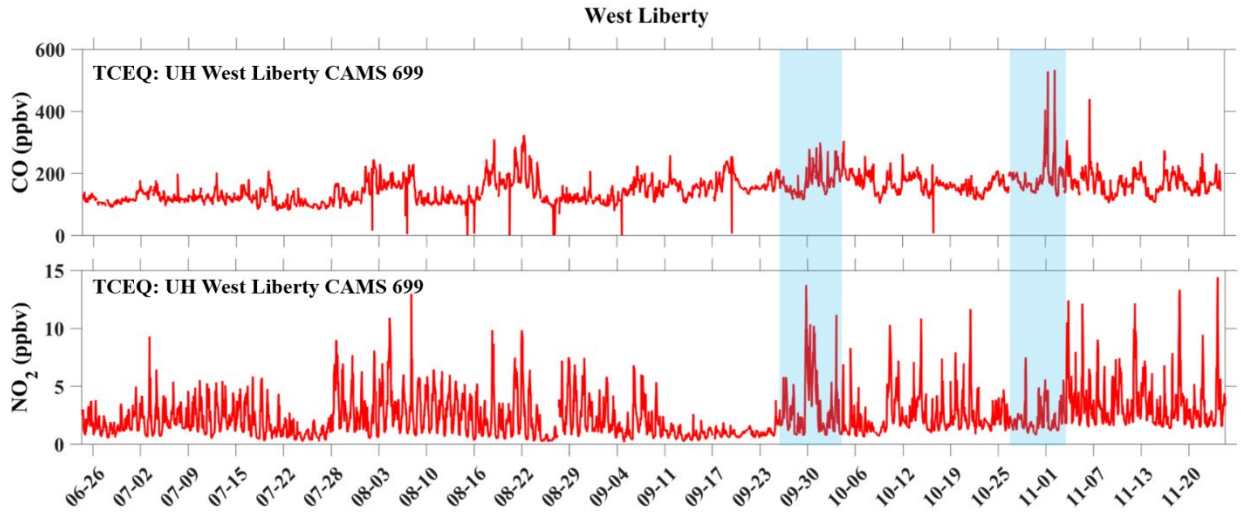

Figure 24. Time series (hourly average) of trace gases (CO and NO_2) observed at West Liberty during the month of June through November 2020. The CO and NO_2 concentrations were taken from TCEQ CAMS 699 (UH- West Liberty) site.

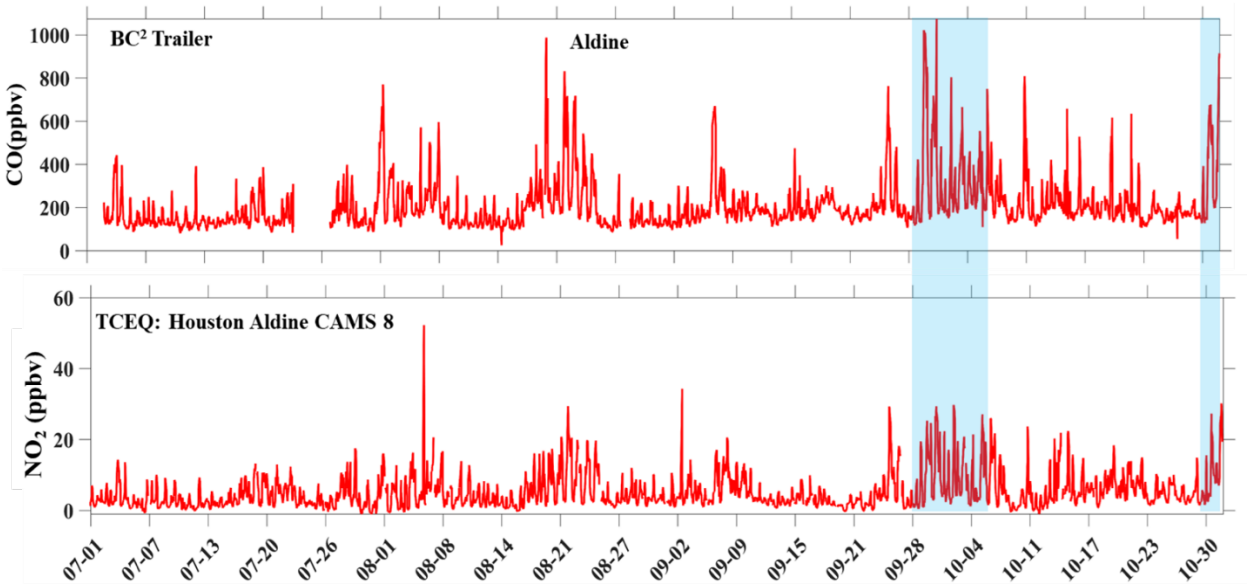

Figure 25. Time series (hourly average) of trace gases (CO and NO2) observed at Aldine during the month of July through November 2020. The CO concentrations was taken from the BC2 trailer and NO_2 concentrations were taken from TCEQ CAMS 8 (Aldine, Houston) sites.

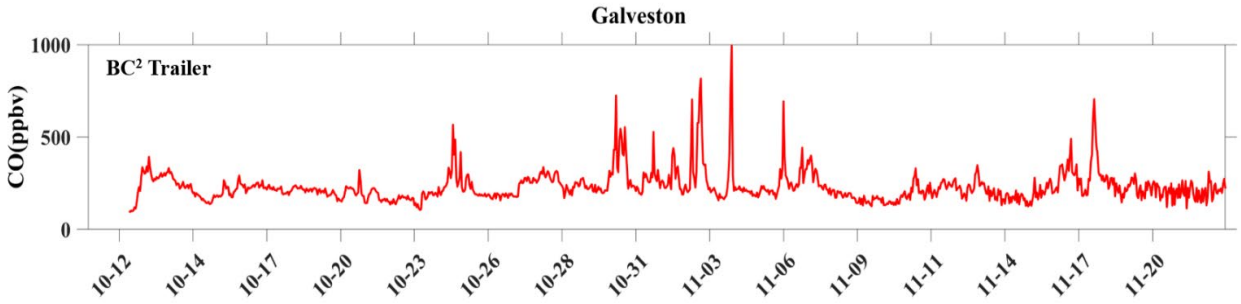

Figure 26. Time series (hourly average) of trace gases (CO) observed at Galveston during the month of October through November 2020.

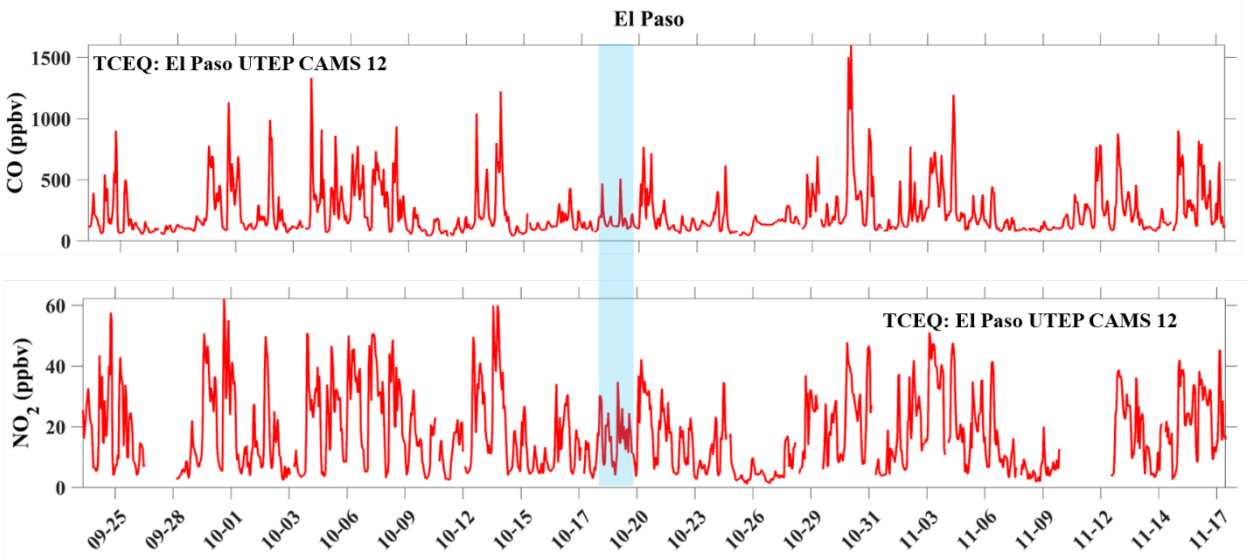

Figure 27. Time series (hourly average) of trace gases (CO and NO_2) observed at El Paso during the month of September through November 2020. The CO and NO2 concentrations were taken from TCEQ CAMS 12 (UTEP) site.

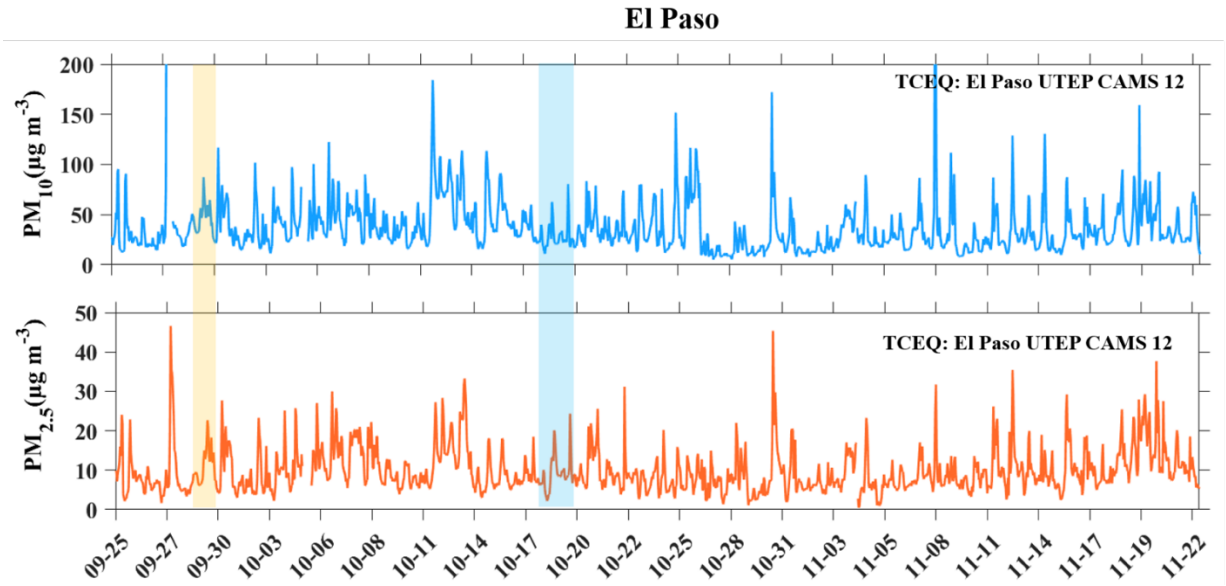

Figure 28. Time series (hourly average) of $PM_{2.5}$ and PM_{10} observed at El Paso during the month of September through November 2020. The $PM_{2.5}$ and PM_{10} concentrations were taken from TCEQ CAMS 12 (UTEP) site.

4.2. Biomass Burning and Dust Events

4.2.1. Definition of BB event for each site

One of the goals of this project is to identify and characterize fire events impacting the $(BC)^2$ sites and therefore the cities of Houston and El Paso. As the project and network of sites accumulates data, the campaign averages and standard deviations can help define the baseline by location and eventually, by season as well. For now, the project defines a biomass burning event as:

1. AAE > site average + 1 standard deviation
2. > 4 hour duration of enhanced AAE
3. SAE > 1

By using the site average, we also are allowing for different baseline conditions for aerosol optical properties at different sites. The time limitation and the SAE limitation were included after preliminary analysis of AAE using all datapoints and an SAE cutoff of 0.5. The preliminary and final analysis are included below for comparison.

Figure 29 (upper panel) represents the percentage of the datapoints falling into the category of BB burning events during different months of sampling at each site based on conditions: AAE > site average +1standard deviation and SAE > 0.5 (rather than considering SAE > 1). The SAE dust aerosols can also have lower SAE and higher AAE due to enhanced absorption in the UV spectrum depending on the composition (Ealo et al., 2016). Notably, no time limitation is included. Thus, the analysis is likely to provide a false indication of BB burning events at the sites.

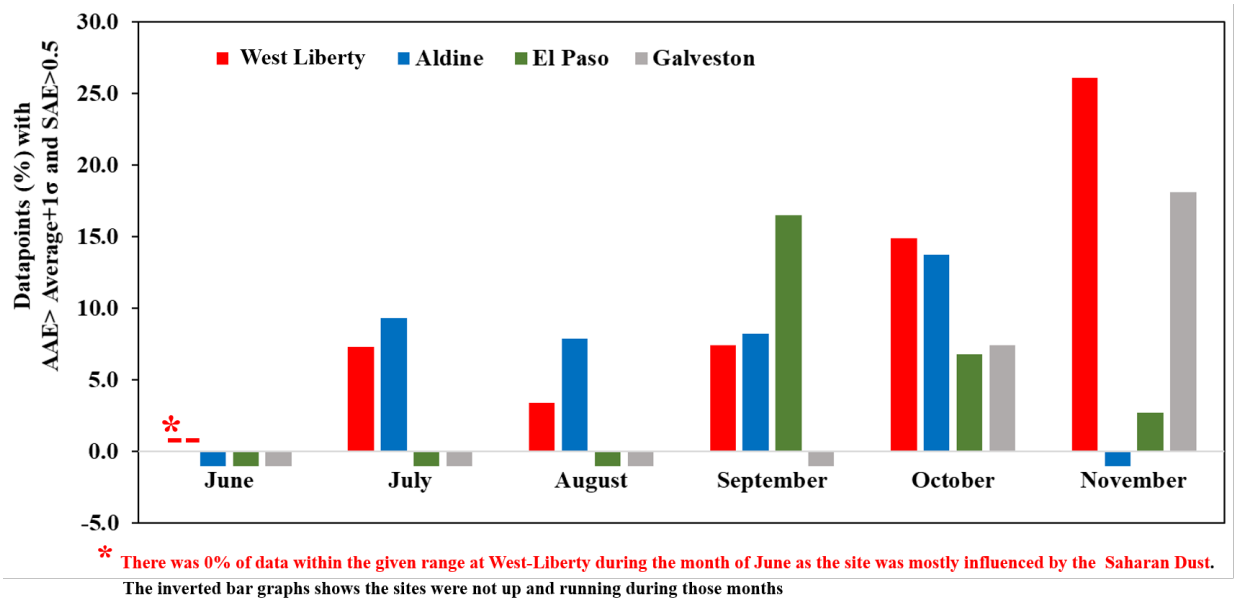

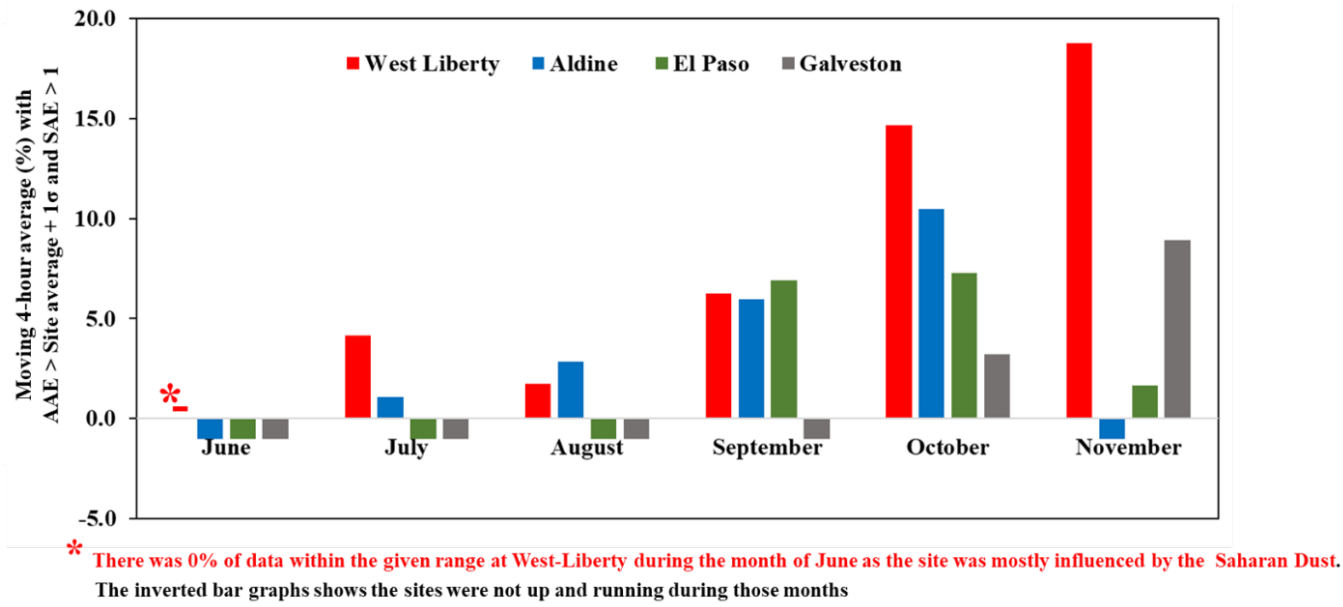

Figure 29. Monthly percentage of datapoints with AAE > specific site average + 1σ and SAE > 0.5 at each site, an indicator of biomass burning influence (upper panel). The El Paso September bar represents data from Sept 25. Lower panel represents percentage of moving 4 hour average AAE > specific site average + 1σ and SAE > 1.0 at each site.

The analysis was further updated and the monthly data points falling into the category of the BB events were calculated using the conditions: moving average of AAE for 4 hours > site average +1standard deviation and SAE > 1 (Figure 30: lower panel). With SAE>1 we are minimizing the possibility of dust influenced events that may have higher AAE. In addition, taking moving average for 4 hours makes sure that the datapoints does not include any momentarily enhancements in AAE and SAE. These conditions provided more realistic information about the of BB events at each site, with fewer events counted for each site. Note: This event identification method will continue to be improved and the best automated way to identify the BB events based on AAE, SAE and absorption/scattering coefficients will be applied in future work. In the future we will include the possibility to assess events that are influenced by both dust and smoke.

With these parameters, the monthly impact from biomass burning events can be calculated to better evaluate seasonal differences in biomass burning and wildfire impacts.

4.2.2. Definition of dust event for each site (MM + RJS)

One of the goals of this project is to identify and characterize dust events impacting the $(BC)^2$ sites and therefore the cities of Houston and El Paso. As the project and network of sites accumulates data, the campaign averages and standard deviations can help define the baseline by location and eventually, by season as well. For now, the project defines a dust event as:

1. SAE < 0.5
2. > 4 hour duration of depressed SAE
3. Scattering Coefficient > monthly average at all the three wavelengths

These limitations help to minimize assignment of sea salt spray impacts on SAE as dust events at site like Galveston (discussed below). Preliminary analysis with only the SAE < 0.5 is included

in the upper panel, while the full conditions are included in the lower panel. It may be necessary to re-evaluate the time limitation for dust events in El Paso in future campaigns, as haboobs will be shorter duration than 4 hours. These time limitations are set to evaluate impacts from global scale dust events like the Saharan dust impacts in June – July.

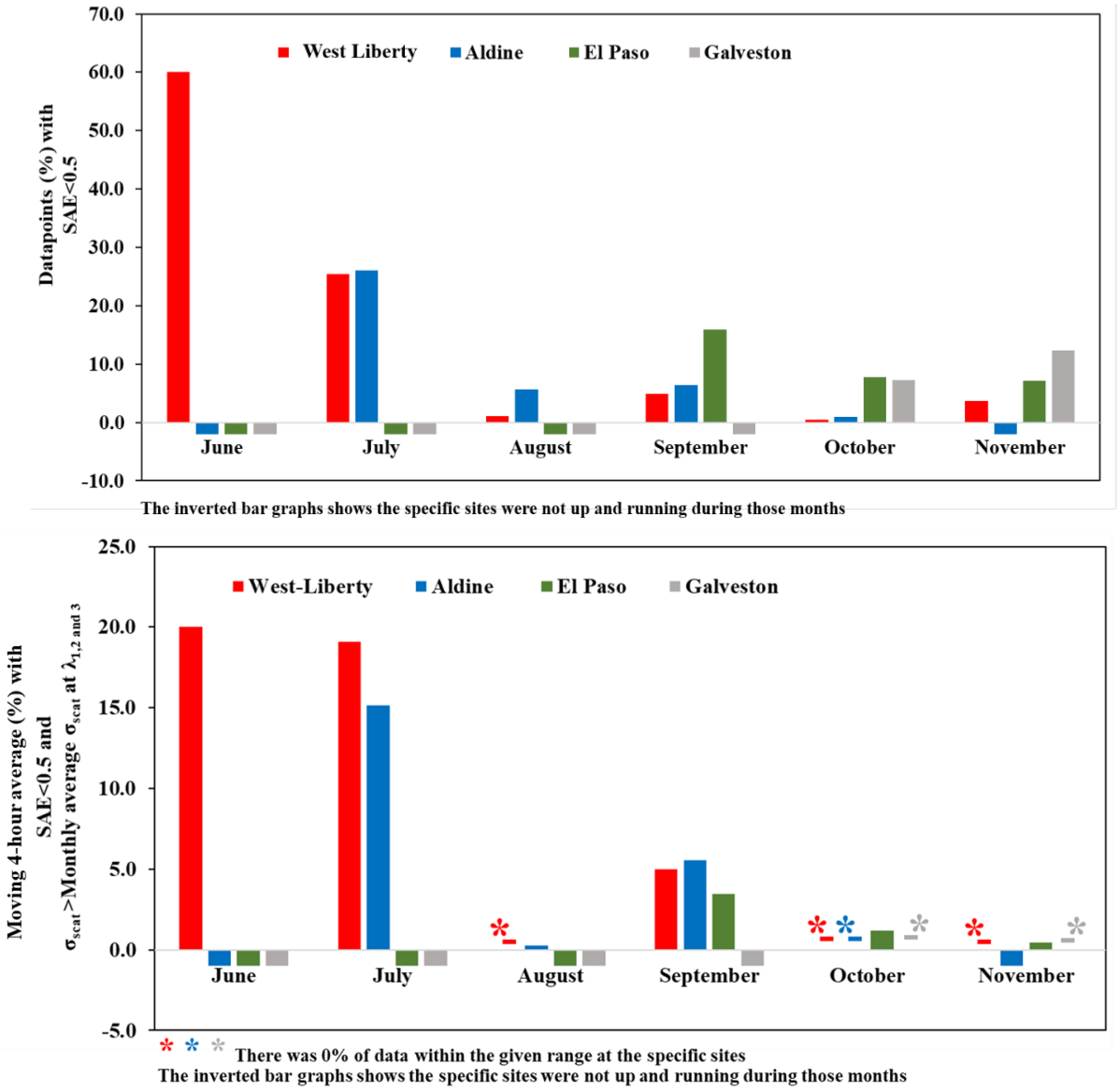

Figure 30. Monthly percentage of datapoints with SAE < 0.5 at each site, an indicator of dust influence (upper panel). Lower panel represents percentage of moving 4 hour average SAE > 0.5 and scattering coefficients > monthly average.

Figure 30 (upper panel) presents the datapoints falling into the category of dust events during different months of sampling at each site based only on the condition: SAE < 0.5. The coastal site like Galveston experiences sea salt spray which have relatively larger size than the urban or BB aerosols and hence results in lower SAE (even <0.5). This therefore can give an erroneous

indication of dust while using only SAE as the conclusive parameter for identifying dust events. Hence, we updated the conditions used for identifying dust events (i.e., moving average of SAE for 4 hours <0.5 and scattering coefficients > monthly average) which can better identify the dust events and differentiates it from the sea salt spray (Figure 31: (lower panel). It should be noted that due to the geographical and meteorological conditions (desert climate), El Paso may experience local dust events that are shorter in duration than the current condition chosen to identify the events (4 hours), but with high scattering coefficients. Thus, the algorithm for identifying dust events at the specific sites may have systematic updates in future work. Note: This event identification method will be improved and the best automated way to identify the dust events based on SAE and scattering coefficients will be applied in future work.

4.2.2.1. Supporting data: 3D modeling

Shown in Figure 31 through 35 are the results of the new methodology applied on days which observed a biomass burning event or a dust event, respectively. On an individual day when the daily mean tracer value at the targeted grid exceeds the 75th percentile value of its 7-year distribution of the same month, it is labeled as a potential long-range transport event from that tracer region to the targeted grid, indicated by the black stars in Figure 4 through Figure 8. Further, specific tracers were chosen as they indicated an event on the date(s) of interest for biomass burning and dust events, while aligning with possible source regions identified by the HYSPLIT back trajectories. These tracers shown in Figure 31 through 35 had concentrations which exceeded their 3rd quantile value of the 7-year daily-mean distribution and thus could have influenced the sites of interest at the identified time period. Dust events were observed during late June and early July. These events were sourced in the Saharan Desert in Africa, which is not included in our 3D Tracer modeling (see methods).

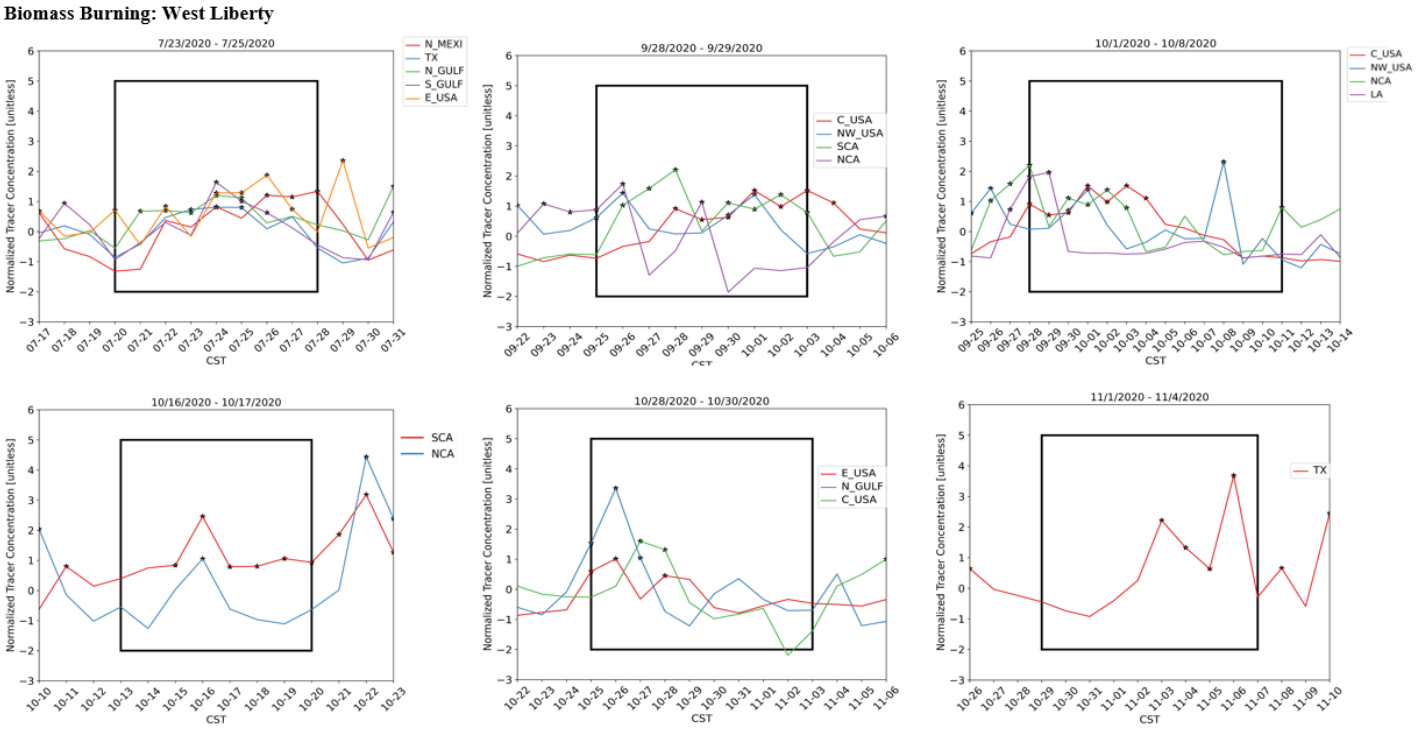

Figure 31. Time series of normalized tracers influencing the biomass burning transport event observed at the West Liberty site's targeted grids. Specific tracers were selected as they indicated an event on the date(s) of interest for biomass burning and aligned with possible source regions identified from back trajectories. Potential long range transport events are shown with black stars. Tracer abbreviations: C_USA: Central USA, NW_USA: Northwest USA, NCA: Northern California, SCA: Southern California, SW_USA: Southwest USA, LA: Louisiana, E_USA: Eastern USA, TX: Texas, N_GULF: Northern Gulf of Mexico, S_GULF: Southern Gulf of Mexico, N_MEXI: Northern Mexico.

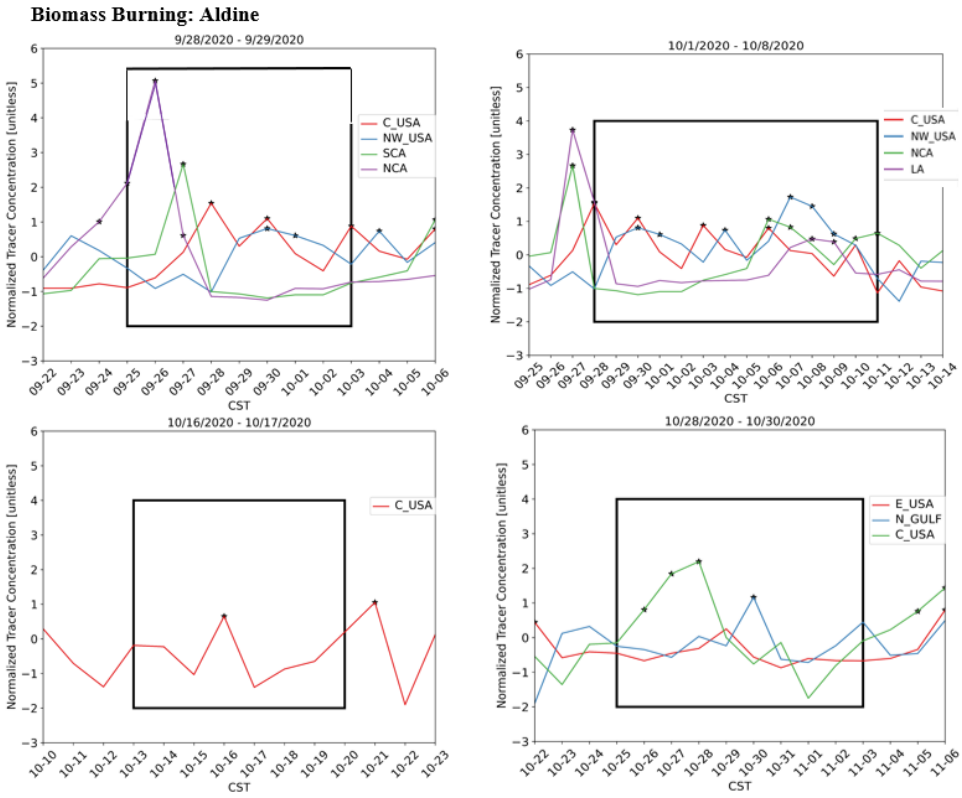

Figure 32. Time series of normalized tracers influencing the biomass burning transport event observed at the Aldine site's targeted grids. Specific tracers were selected as they indicated an event on the date(s) of interest for biomass burning and aligned with possible source regions identified from back trajectories. Potential long range transport events are shown with black stars. Tracer abbreviations: C_USA: Central USA, NW_USA: Northwest USA, NCA: Northern California, SCA: Southern California, LA: Louisiana, E_USA: Eastern USA.

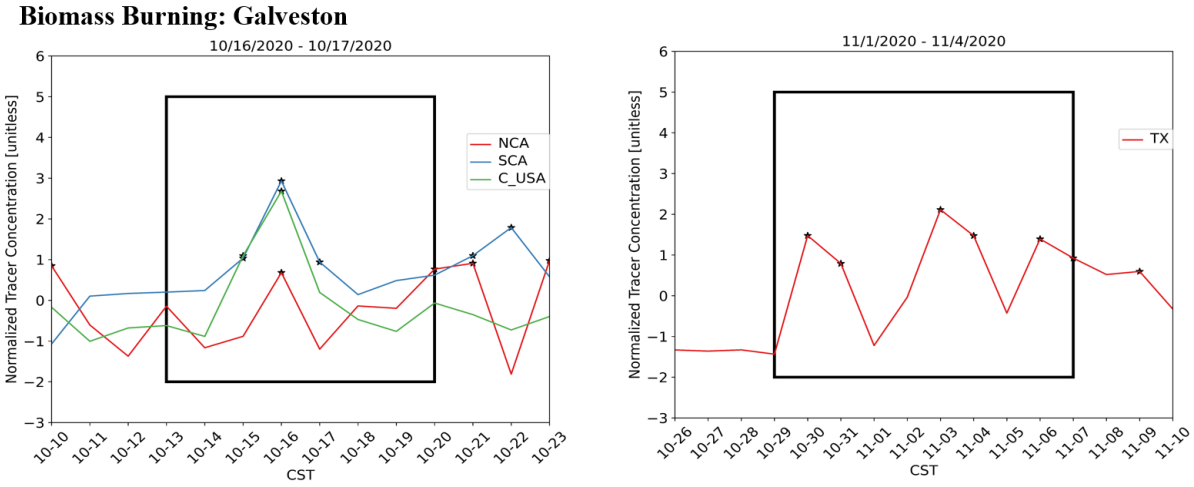

Figure 33. Time series of normalized tracers influencing the biomass burning transport event observed at the Galveston site's targeted grids. Specific tracers were selected as they indicated an event on the date(s) of interest for biomass burning and aligned with possible source regions identified from back trajectories. Potential long range transport events are shown with black stars. Tracer abbreviations: C_USA: Central USA, NCA: Northern California, SCA: Southern California, TX: Texas.

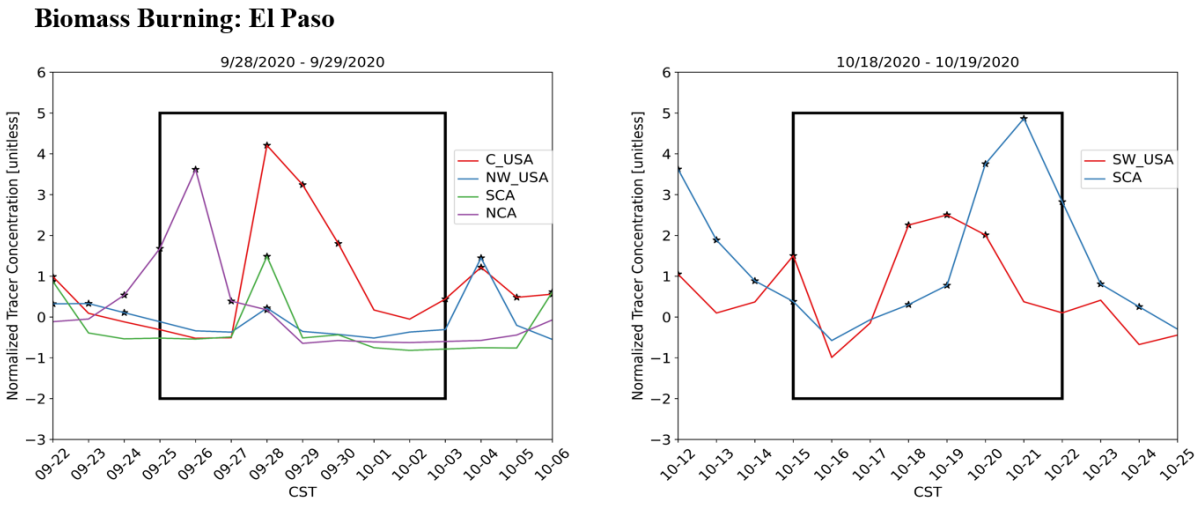

Figure 34. Time series of normalized tracers influencing the biomass burning transport event observed at the El Paso site's targeted grids. Specific tracers were selected as they indicated an event on the date(s) of interest for biomass burning and aligned with possible source regions identified from back trajectories. Potential long range transport events are shown with black stars. Tracer abbreviations: C_USA: Central USA, NW_USA: Northwest USA, NCA: Northern California, SCA: Southern California, SW_USA: Southwest USA.

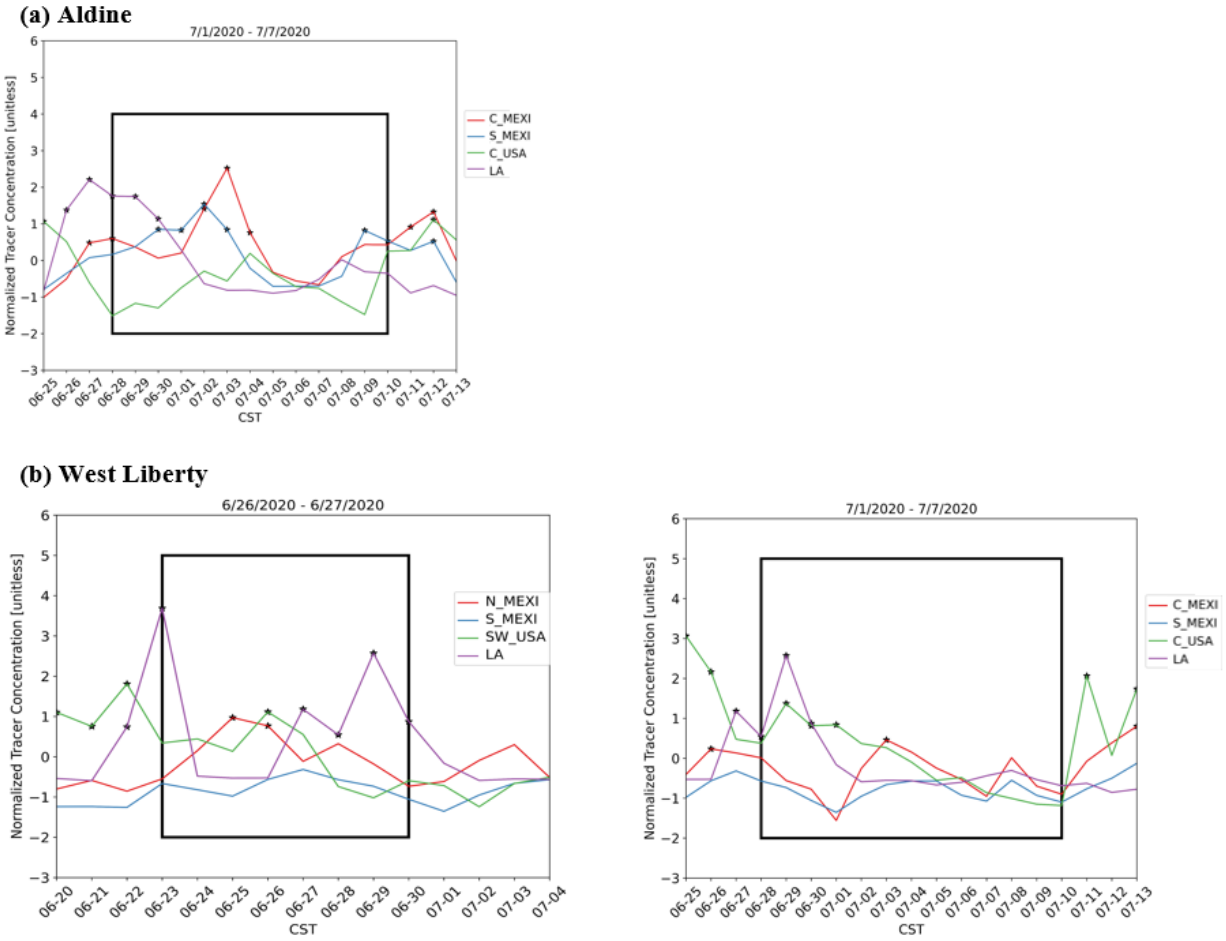

Figure 35. Time series of normalized tracers influencing the dust influenced transport event observed at (a) Aldine, (b) West Liberty targeted grids. Specific tracers were selected as they indicated an event on the date(s) of interest for dust influenced and aligned with possible source regions identified from HYSPLIT back trajectories. Potential long range transport events are shown with black stars. Tracer abbreviations: C_USA: Central USA, NW_USA: Northwest USA, NCA: Northern California, SCA: Southern California, LA: Louisiana, E_USA: Eastern USA, TX: Texas, N_MEXI: Northern Mexico, C_MEXI: Central Mexico, S_MEXI: Southern Mexico.

Figure 36 illustrates the influence of the central USA tracer experienced by the targeted grids on four different days: Aldine site on October 3, 2020, El Paso on September 29, 2020, Galveston on October 16, 2020, and West Liberty on October 28, 2020. The specific tracer and the individual days were chosen here for illustration purpose. This individual tracer and selected

days clearly show the influence of the tracer on the sites of interest. One can observe the increased concentration of the central USA tracer compared to background levels across the state of Texas. Figure 33 helps to confirm the tracer's influence on the sites and could have contributed to the events experienced at each site and day.

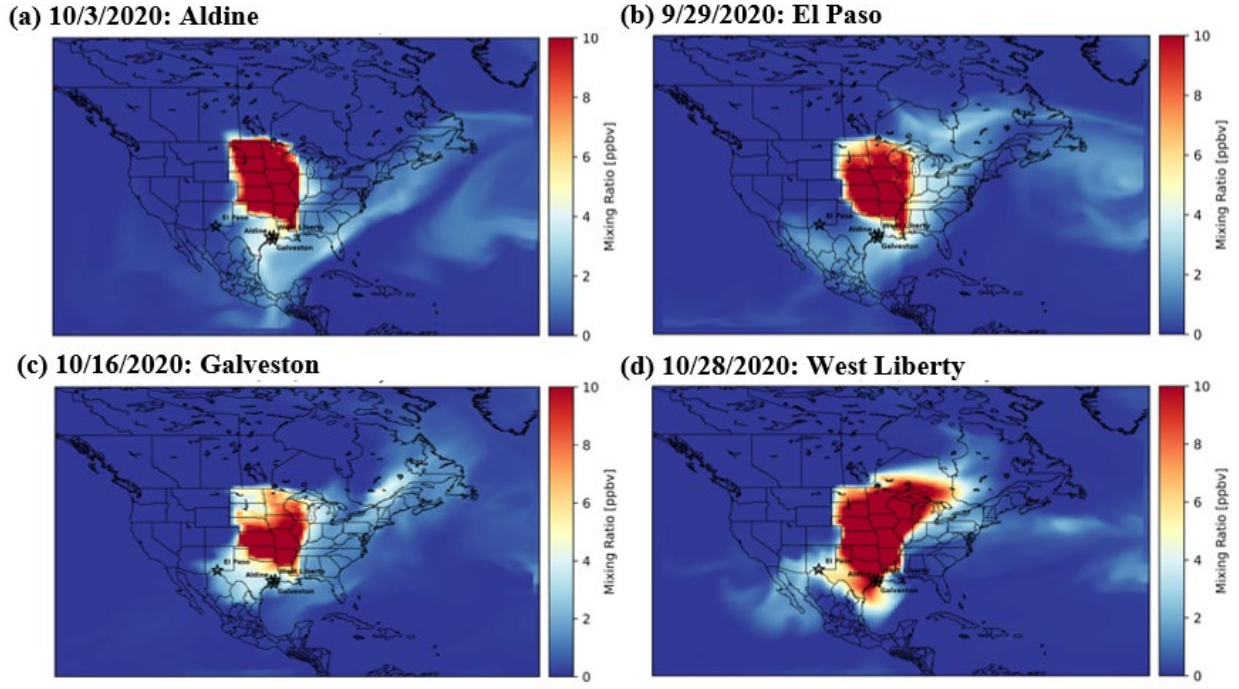

Figure 36. Daily mean concentration maps of the central USA tracer for the targeted grids on identified event days. The maps for (a) Aldine on 10/3/2020, (b) El Paso on 9/29/2020, (c) Galveston 10/16/2020, and (d) West Liberty on 10/28/2020 confirms the central USA tracer's influence on the sites for these individual days. Black stars and site name labels indicate the location of the targeted grids for Aldine, El Paso, Galveston, and West Liberty, employed in the study.

The results of this modeling study aided in determining the possible source regions for the biomass burning and dust influenced events observed during June – November 2020. Each individual site, Aldine, El Paso, Galveston, and West Liberty, experienced influences from various tracers throughout the study period. We find that the area experienced the most influence from the central USA, northwest USA, eastern USA, Texas, southern and northern California, Louisiana, north Gulf of Mexico, northern, central, and southern Mexico tracer.

4.2.3. Timeline of events – Houston and El Paso

All the events for each site have been plotted in a box and whisker style to characterize and compare AAE, SAE and SSA by event for each site. In addition, the site average is plotted on the far left for comparison purposes. The SSA indicates how much impact aerosol absorption has on the total aerosol extinction (absorption + scattering). A lower SSA indicates greater absorption and potentially indicates how much the smoke plume is impacting the total aerosol loading, as the smoke plume would likely be more absorbing. The biomass burning events are defined as either local (e.g. effecting only one site) or Houston (e.g. effecting all Houston sites) in terms of the spatial extent of impact within the Houston network of $(BC)^2$ sites.

A table of the 3D Tracer modeling results is included at the end of this section. This table compares the airmass transport as shown by HYSPLIT back trajectory analysis with the 3D Tracer model which compares the modeled transport with transport climatology for each site to look for transport events or anamolies. If the transport pattern is consistent with previous years, it will not be labeled a transport event by this model. The 3D model does confirm event transport during the early and mid – October biomas burning events.

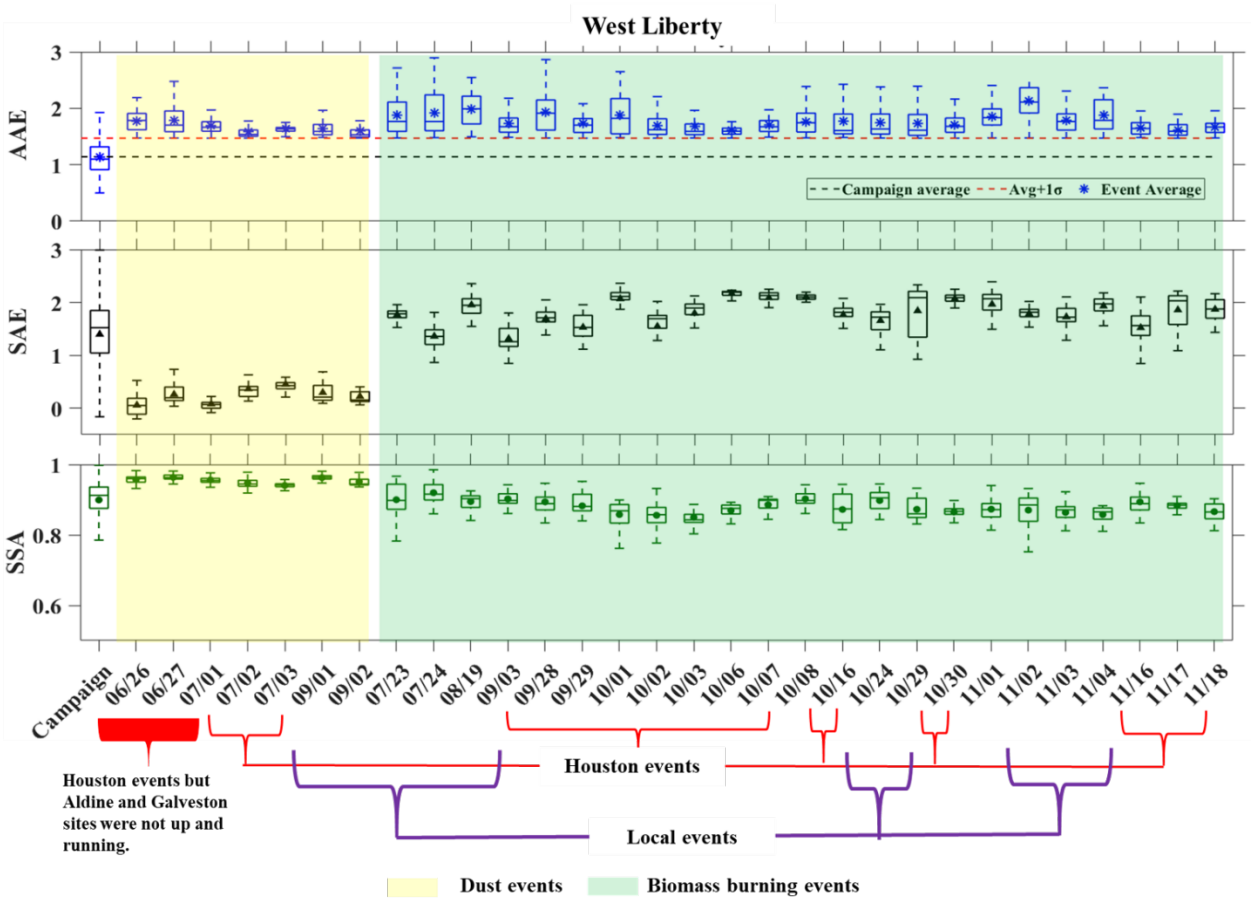

Figure 37. Box and whisker plot for the AAE, SAE and SSA for the campaign average and the different dust and biomass burning events at West Liberty. The asterisk, triangle and the circle represent the average AAE, SAE and SSA values, respectively and the line represents the median values observed during the entire campaign and the respective event day.

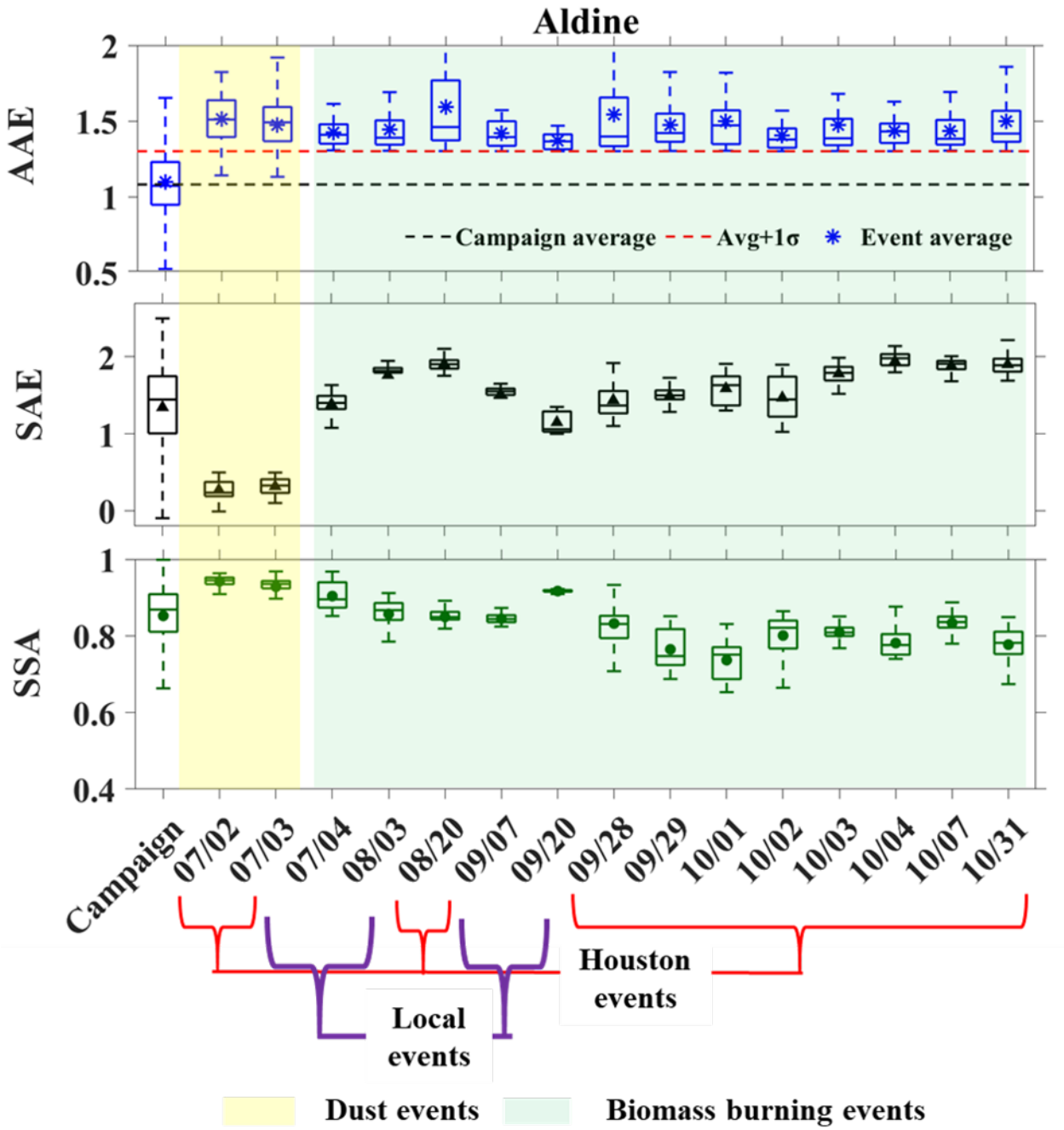

Figure 38. Box and whisker plot for the AAE, SAE and SSA for the campaign average and the different dust and biomass burning events at Aldine. The asterisk, triangle and the circle represent the average AAE, SAE and SSA values, respectively and the line represent the median values observed during the entire campaign and the respective event day.

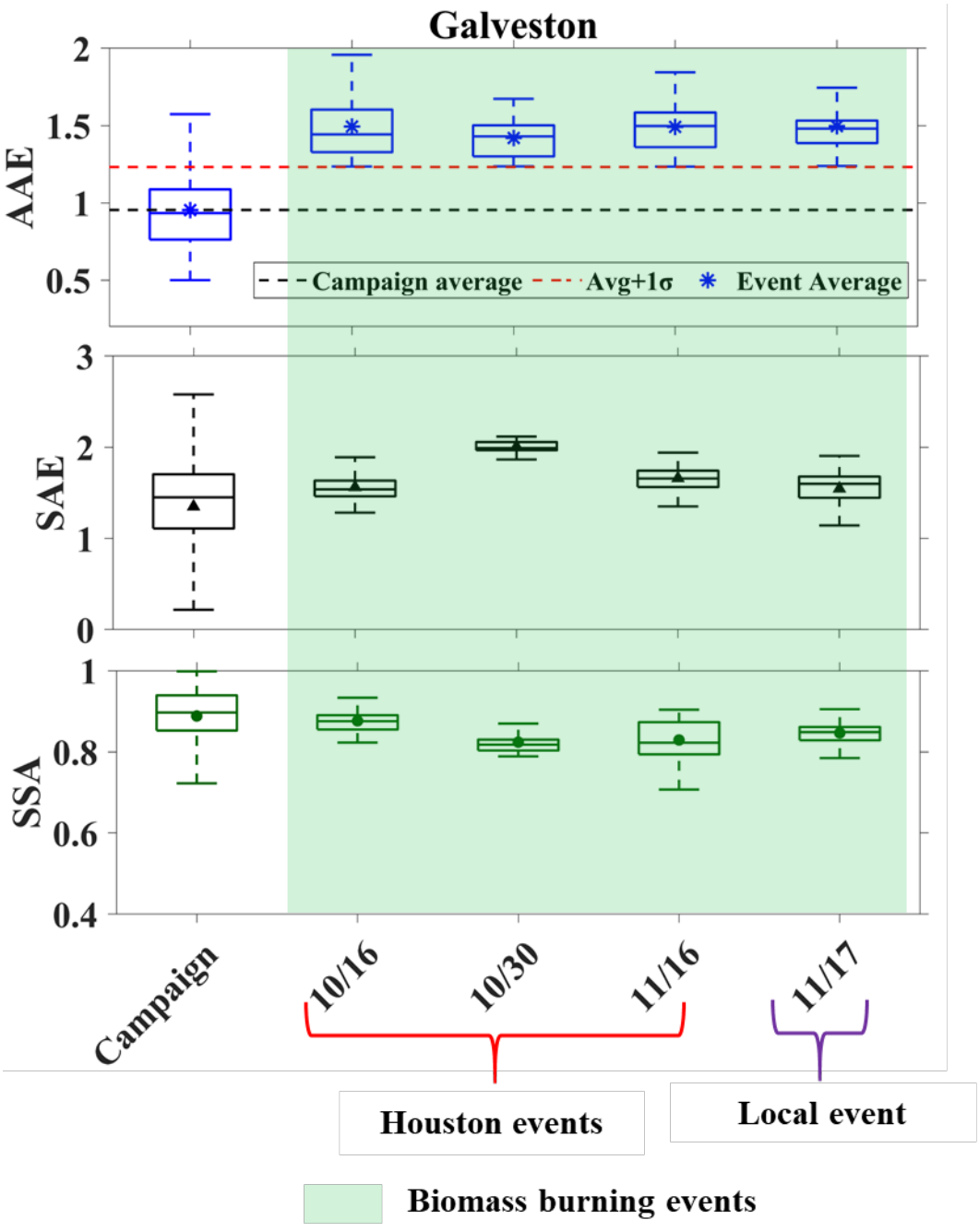

Figure 39 . Box and whisker plot for the AAE, SAE and SSA for the campaign average and the different dust and biomass burning events at Galveston. The asterisk, triangle and the circle represent the average AAE, SAE and SSA values, respectively and the line represents the median values observed during the entire campaign and the respective event day.

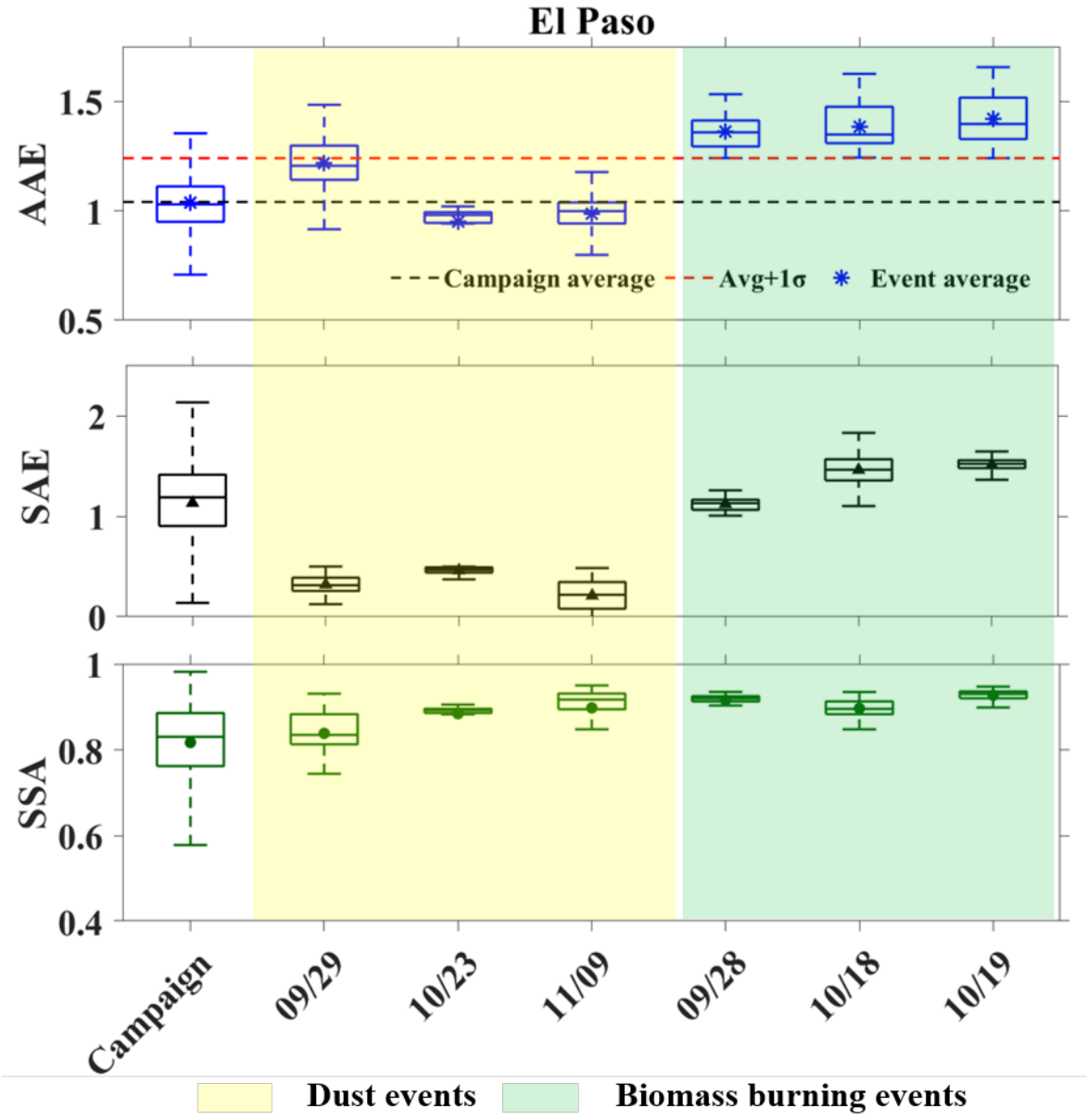

Figure 40. Box and whisker plot for the AAE, SAE and SSA for the campaign average and the different dust and biomass burning events at El Paso. The asterisk, triangle and the circle represent the average AAE, SAE and SSA values, respectively and the line represents the median values observed during the entire campaign and the respective event day.

Table 3. List of biomass burning influenced days

Start date	End date	Site	BT source regions	3D Tracer Modeling - Defined Event (on Date)	Tracer which matches BT source regions
23-Jul-20	25-Jul-20	West-Liberty	Unknown	E USA, SA, N GULF, S GULF, HOU, TX, S MEXI, N MEXI	C USA, NW USA, SCA, NCA,
28-Sep-20	29-Sep-20	West-Liberty, Aldine	California, Colorado, Louisiana	West Liberty: NW USA, DFW, N GULF, HOU, NCA, SCA Aldine: NPC, NW USA, N GULF, SCA	C USA, NW USA, SCA, NCA,
1-Oct-20	8-Oct-20	West-Liberty/ Aldine	California, Colorado, Louisiana	West Liberty: DFW, C USA, NW USA, NPC, E USA, SA, TX, NCA, LA Aldine: C USA, NW USA, E USA, NPC, DFW, HOU, SA, TX, NCA, SW USA, N MEXI	C USA, NW USA, NCA, LA
16-Oct-20	17-Oct-20	West-Liberty/ Aldine/ Galveston	California, Colorado, Central US,	West Liberty: NCA, SCA Aldine: C USA Galveston: NCA, N MEXI	SCA, NCA, C USA
28-Oct-20	30-Oct-20	West-Liberty/ Aldine	Texas, East US, Louisiana, Central US	West Liberty: NW USA, NPC, E USA, N GULF, SW USA Aldine: E USA, NW USA, C USA, S GULF, C MEXI, SW USA, SCA	E USA, N GULF, C USA
1-Nov-20	4-Nov-20	West-Liberty/ Galveston	Louisiana, Central US, Texas	West Liberty: NPC, TX, SA, S GULF, S MEXI, C MEXI, NCA, N MEXI, RCA, Galveston: NCA, S MEXI, TX, SA, HOU, DFW, NPC, SCA, RCA	TX

28-Sep-20	29-Sep-20	El Paso		El Paso: NPC, NW USA, C USA, N MEXI	
18-Oct-20	19-Oct-20	El Paso	SW US, California, N. Mexico	El Paso: DFW, NPC, NW USA, C USA, SCA, C USA, N MEXI, SW USA	SCA, SW USA

Houston: HOU; Dallas-Fort Worth: DFW; San Antonio: SA; The rest of Texas: TX; Northwest US: NW USA; Southwest US: SW USA; Central USA: C USA; East USA: E USA; North Pacific Coast: NPC; North California: NCA; South California: SCA; North Mexico: N MEXI; Central Mexico: C MEXI; South Mexico: S MEXI; North Gulf of Mexico: N GULF; South Gulf of Mexico: S GULF; Central America: RCA, Louisiana: LA.

4.2.4. Select Biomass burning events– Houston and El Paso

4.2.4.1. Houston - Late September and October

The Houston sites Aldine and West Liberty had intermittent influence from biomass burning in late September and early October 2020 (Sept 29 – Oct 9). The SAE confirmed no contribution from dust during these periods of enhanced AAE. Back trajectory analysis combined with the NOAA HMS mapping confirmed a large-scale smoke event (only select days are displayed). The HMS product highlights smoke coverage that extends to wildfires in Colorado, and the West Coast. This smoke was transported to Texas following a northern frontal system that moved through the region.

Both sites have similar back trajectories, however, the impact is more pronounced on the West Liberty aerosol. This may be associated with differences in transport but may also be due to the higher baseline loading of aerosol at Aldine. The transport modeling also indicates enhanced transport from the West Coast and the Northwest US during early October.

Similarly, an additional event in mid-October (Oct 16-17) was evident across the three Houston sites (West Liberty, Aldine and Galveston). HMS and back trajectories indicate potential influence from the central and western US. The transport modeling indicates transport anomalies for transport from the Central US and California.

There is often not a clear connection between increased AAE and increases in PM compared to the background. For some events, like Oct 16 and 17, the PM decreases. This may be due to the mixing with higher altitude air that includes a long-range smoke plume.

Figure 41. Time series (hourly average) of AAE and SAE values observed at West Liberty and Aldine sites during late September and early October 2020 at Houston.

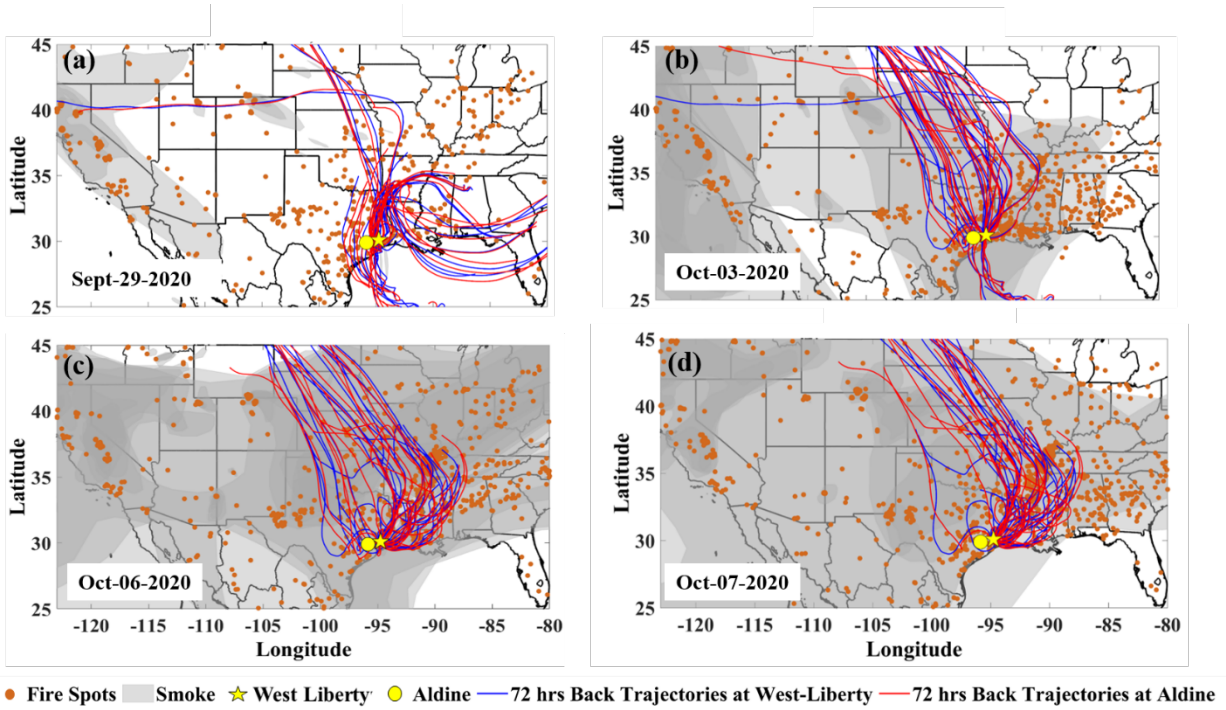

Figure 42. Spatial distribution of fire spots (retrieved from VIIRS), smoke cover (retrieved from NOAA fire and Hazard mapping model) during the biomass burning events at West Liberty and Aldine. The blue and red lines represent the 72 hours back trajectories obtained from the HYSPLIT model for the specific days at West Liberty and Aldine, respectively.

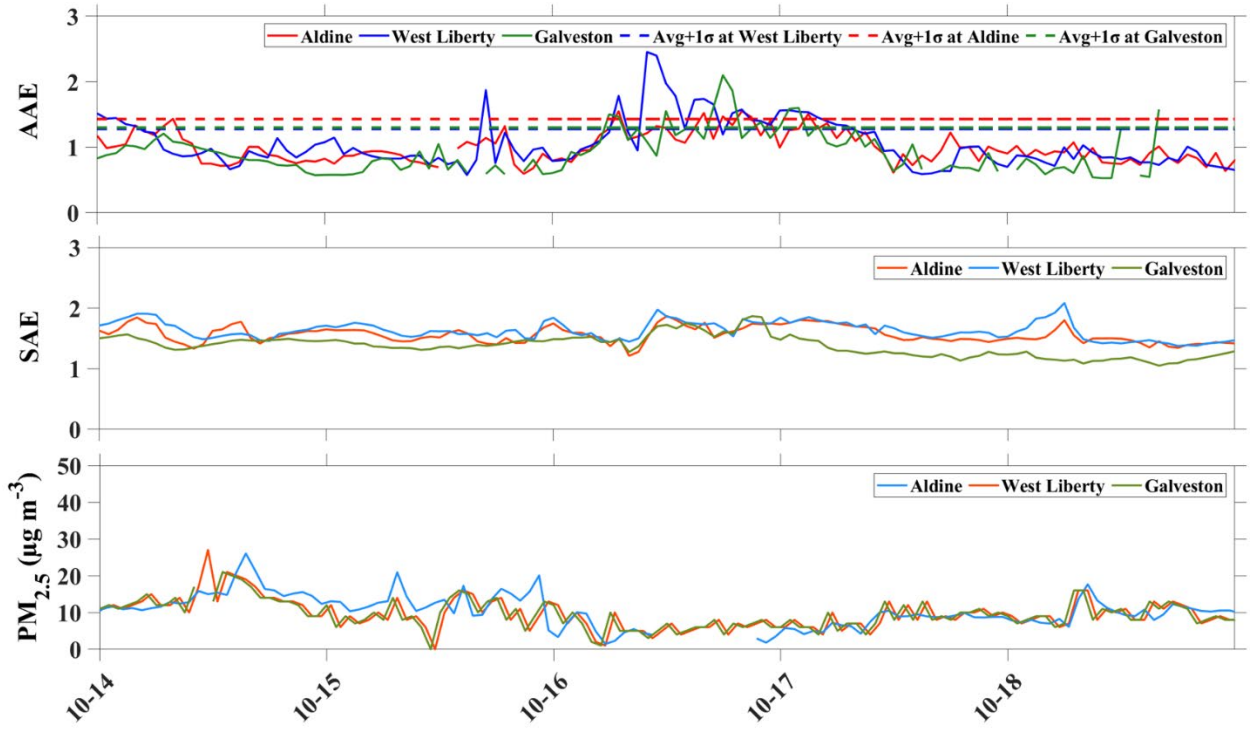

Figure 43. Time series (hourly average) of AAE and SAE values observed at West Liberty, Aldine, and Galveston sites during mid-October 2020 in Houston.

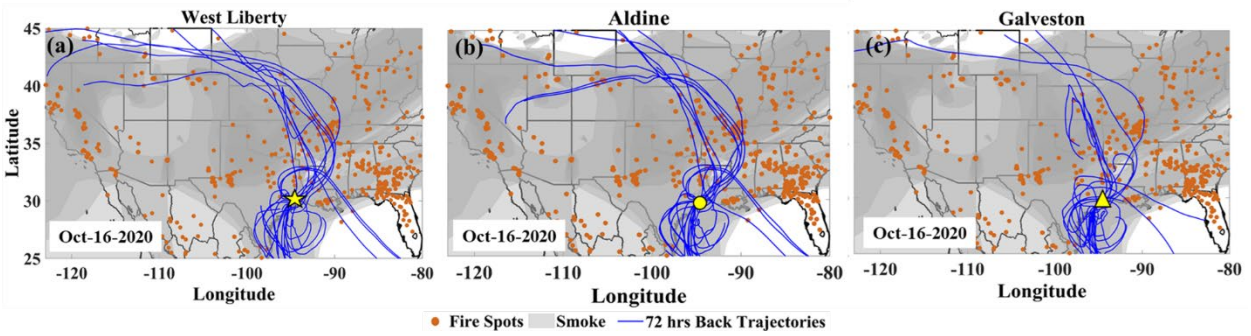

Figure 44. Spatial distribution of fire spots (retrieved from VIIRS), smoke cover (retrieved from NOAA fire and Hazard mapping model) during the biomass burning events at West Liberty, Aldine, and Galveston. The blue lines represent the 72 hours back trajectories.

4.2.4.2. Late October

The late October and November fire events for Houston were potentially more local in origin. The HMS for Oct 30, Nov 2 and Nov 3 does not show any regional smoke, but VIIRS indicates many close fires. Galveston AAE and SAE do not indicate smoke influence, while Aldine and

West Liberty do show smoke influence for Oct 30-31. The back trajectories are scattered from many directions and the transport modeling indicates event transport from the Central US, Texas and the Northern Gulf transport.

For mid-Nov (Nov 16-18), there was smoke impact at both West Liberty and Galveston. This may be local or Louisiana as there is no evident smoke in HMS, but the back trajectories do pass over fires along the Gulf coast and Louisiana.

Although the biomass burning events earlier in October did not have a clear relationship to PM, the early November events do align with large increases in PM. These events may be more regional in nature.

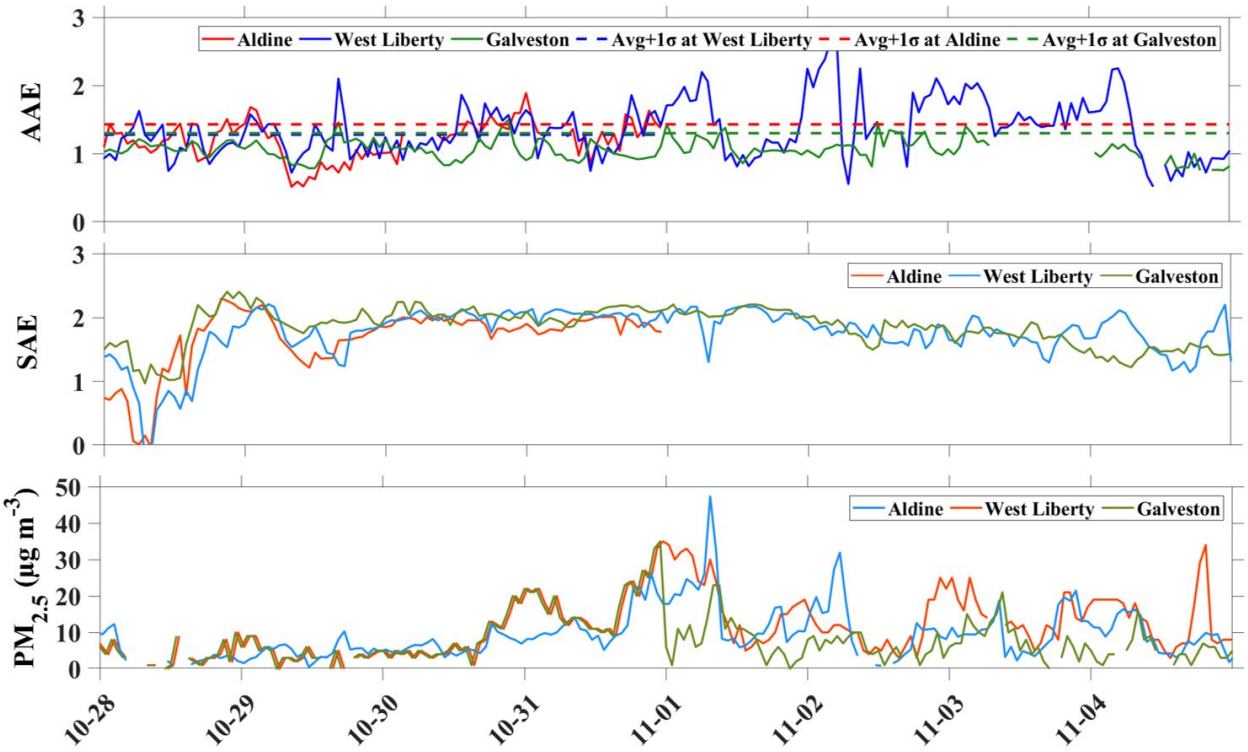

Figure 45. Time series of AAE and SAE for Aldine, West Liberty, and Galveston in late October.

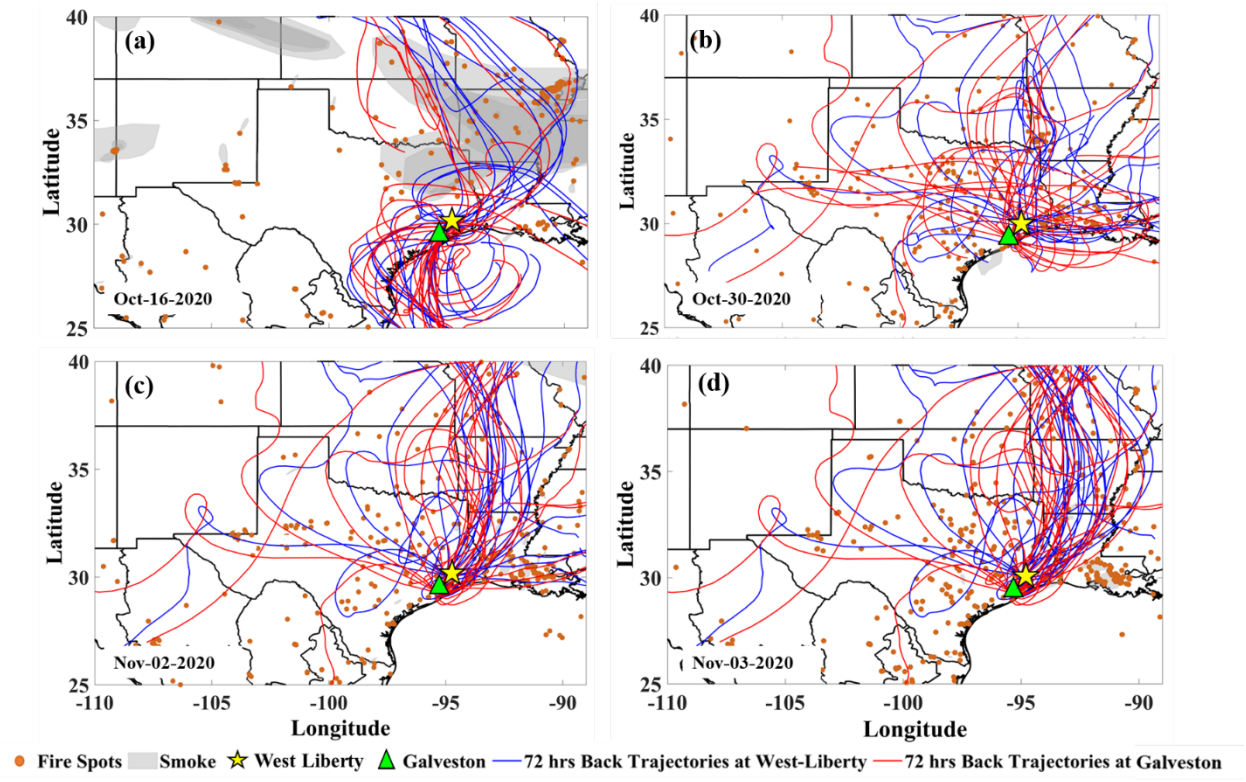

Figure 46. Spatial distribution of fire spots (retrieved from VIIRS), smoke cover (retrieved from NOAA fire and Hazard mapping model) during the biomass burning events at West Liberty and Galveston. The blue and red lines represent the 72 hours back trajectories obtained from the HYSPLIT model for the specific days at West Liberty and Galveston, respectively.

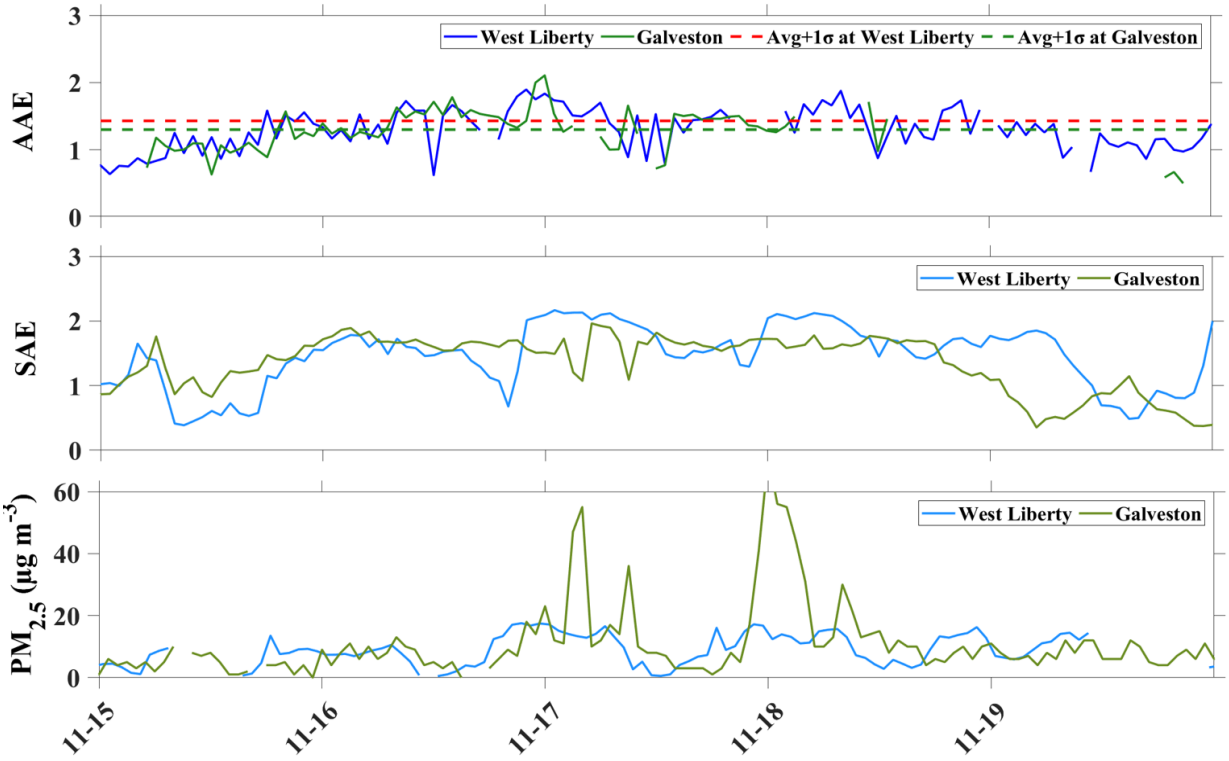

Figure 47. Time series of AAE and SAE for West Liberty and Galveston in mid-November.

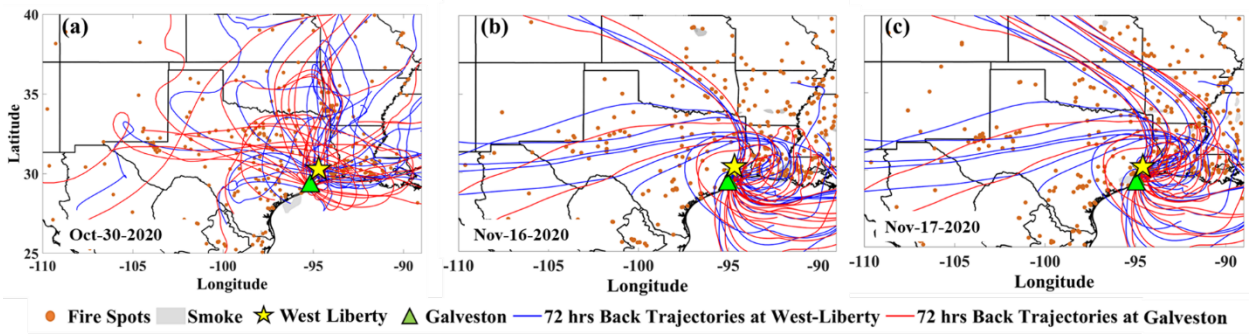

Figure 48. Spatial distribution of fire spots (retrieved from VIIRS), smoke cover (retrieved from NOAA fire and Hazard mapping model) during the biomass burning events at West Liberty and Galveston. The blue and red lines represent the 72 hours back trajectories obtained from the HYSPLIT model for the specific days at West Liberty and Galveston, respectively.

There is a unique event in the early days of the 2020 campaign in El Paso, where there were periods of intermittent dust and biomass burning over two days (Sept 28 and 29). 24hr analysis would struggle to separate these events, while the realtime optical measurements show a clear

distinction between dust and biomass burning. For this event, the dust component increases the PM, while the biomass burning component does not.

The time series for El Paso highlighted an event in $PM_{2.5}$ and AAE for October 18 and 19. The HMS and back trajectories for those days show smoke over the region and fires across the southwest (VIIRS fire spots in West Texas are associated with oil and gas flares, not wildfires). The transport modeling does show event transport from Northern Mexico and California, but there are also fires and smoke in the transport path in Arizona and New Mexico. This event does appear to coincide with an increase in PM.

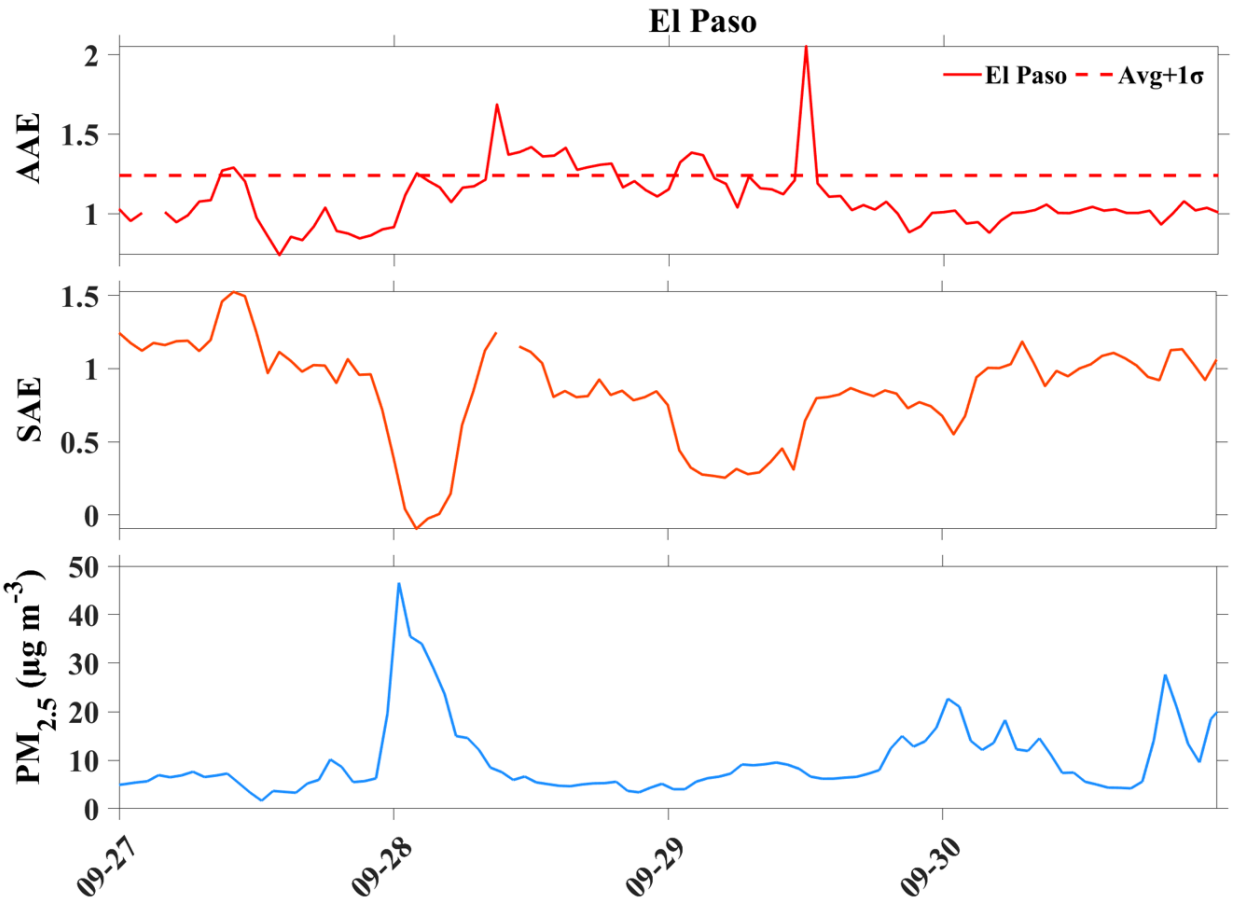

Figure 49. Time series of AAE and SAE for West Liberty and Galveston in late September. NOTE: This include both dust and BB events over the course of two days.

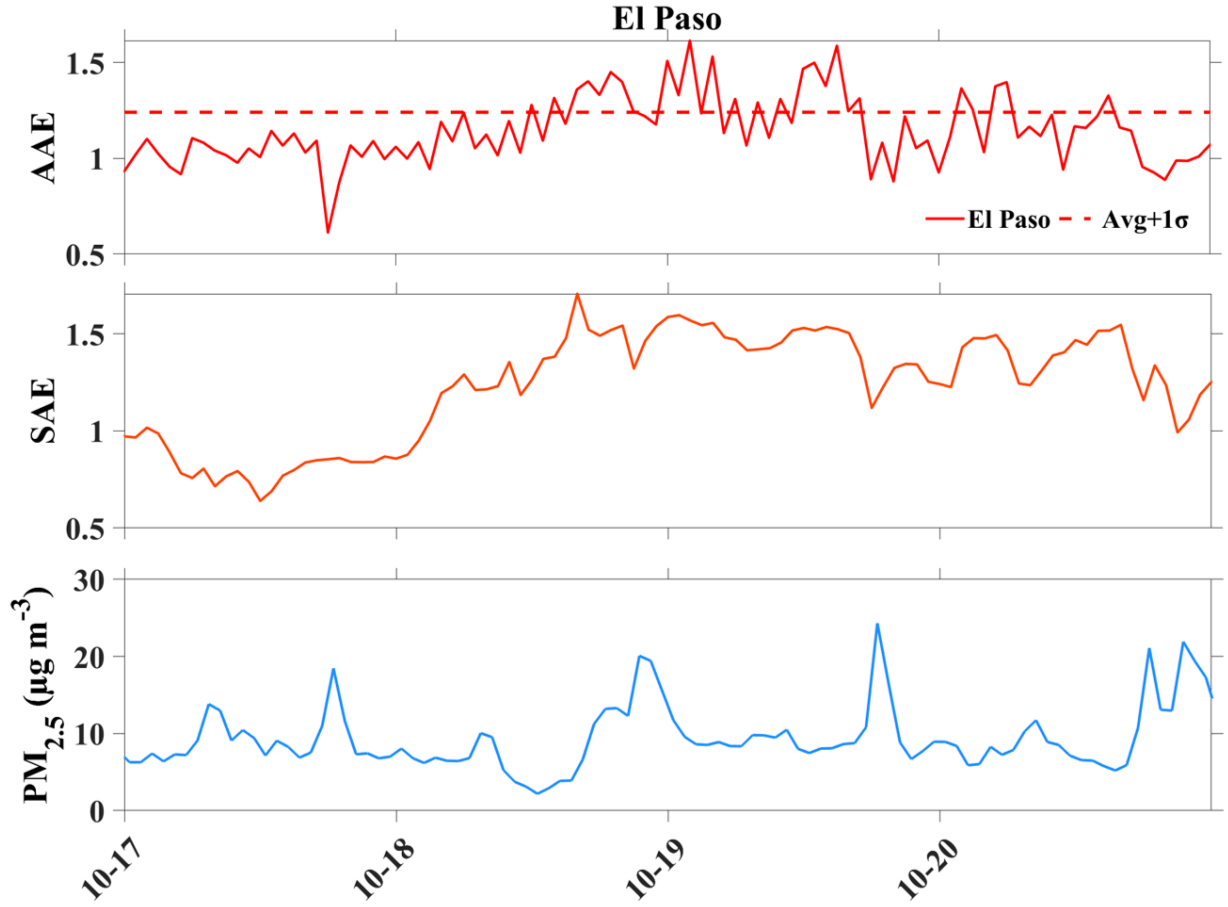

Figure 50. Time series of AAE and SAE for West Liberty and Galveston in mid-October.

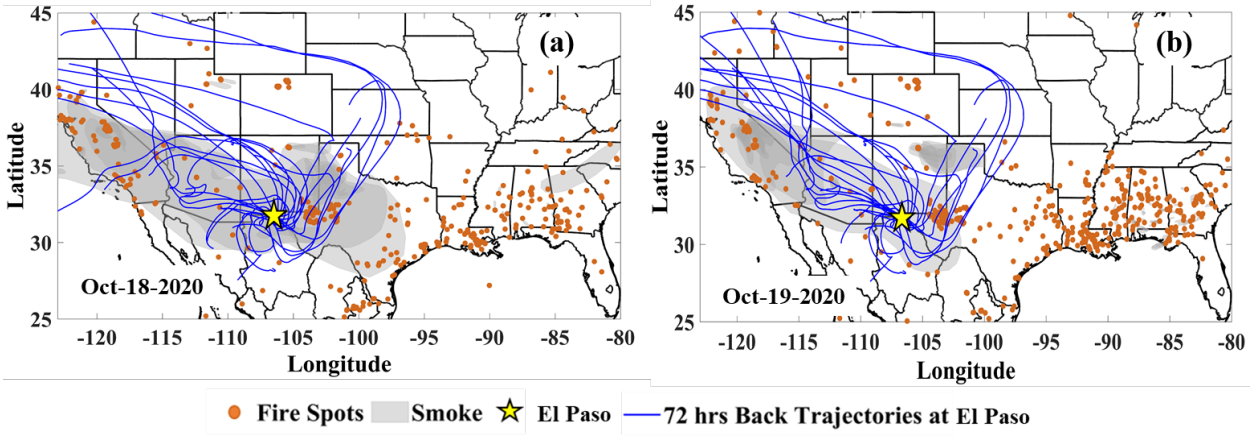

Figure 51. Spatial distribution of fire spots (retrieved from VIIRS), smoke cover (retrieved from NOAA fire and Hazard mapping model) during the biomass burning events at El Paso. The blue

lines represent the 72 hours back trajectories obtained from the HYSPLIT model for the specific days at El Paso.

4.2.4.3. Trace gas enhancement ratios – CO

To define potential gas and particle phase impacts of fire plumes, enhancement ratios (ER) were calculated for the biomass burning and dust events at each site. ER is calculated as

$$ER = \Delta X / \Delta Y$$

Where, $\Delta X = [X_{ambient} - X_{Background}]$ and $\Delta Y = [Y_{ambient} - Y_{Background}]$

These ratios were all calculated with respect to CO as it is the most conserved tracer and is an indication of boundary height impacts. The ERs for the absorption coefficients, scattering coefficients, AAE and SAE were calculated for the biomass burning and the dust events. The background values/concentrations that we used for calculating the ERs are the monthly median value/concentrations of each parameter at 1300 local solar time (LST). The time 1300 was chosen as this time reflects the maximum atmospheric mixing and lower values of σ_{abs}, σ_{sact}, AAE, SAE and CO concentration during a day (Figure 9-12). This method has previously been used by the Briggs et al., 2016; Liang et al 2016. The background value is included for reference.

For dust events, the SAE enhancement ratio clearly shows a decrease in the enhancement ratio, which is related to the definition that dust events have an SAE approaching zero. The scattering coefficient often does show enhancement, and this varies by the intensity of the dust impacts. The highest scattering coefficient enhancement is seen at West Liberty during the Saharan dust event in early July. There was not a uniform enhancement in the absorption coefficient or in the AAE with respect to CO for the dust events. More work is needed to understand how the source and intensity of the dust impacts the absorption and AAE for dust events.

During the BB events the enhancement in the absorption coefficients is observed at all the three wavelengths. Notably, relatively higher ER is observed in the blue wavelength than the red and green during the BB events. This enhancement in σ_{abs} at blue wavelength is the result of enhanced absorption by the light absorbing organic compounds emitted during the BB activities. The enhancement in σ_{abs} at blue wavelength is also resulted in the concurrent enhancement in the AAE. There was not a uniformity in the enhancement ratios of absorption coefficients or the

AAE between and within the local and regional BB events. More work is needed to understand how the source and intensity of the BB impacts the absorption and AAE. Note: This event identification method will be improved and the best automated way to identify the BB events based on ER will be applied in future work.

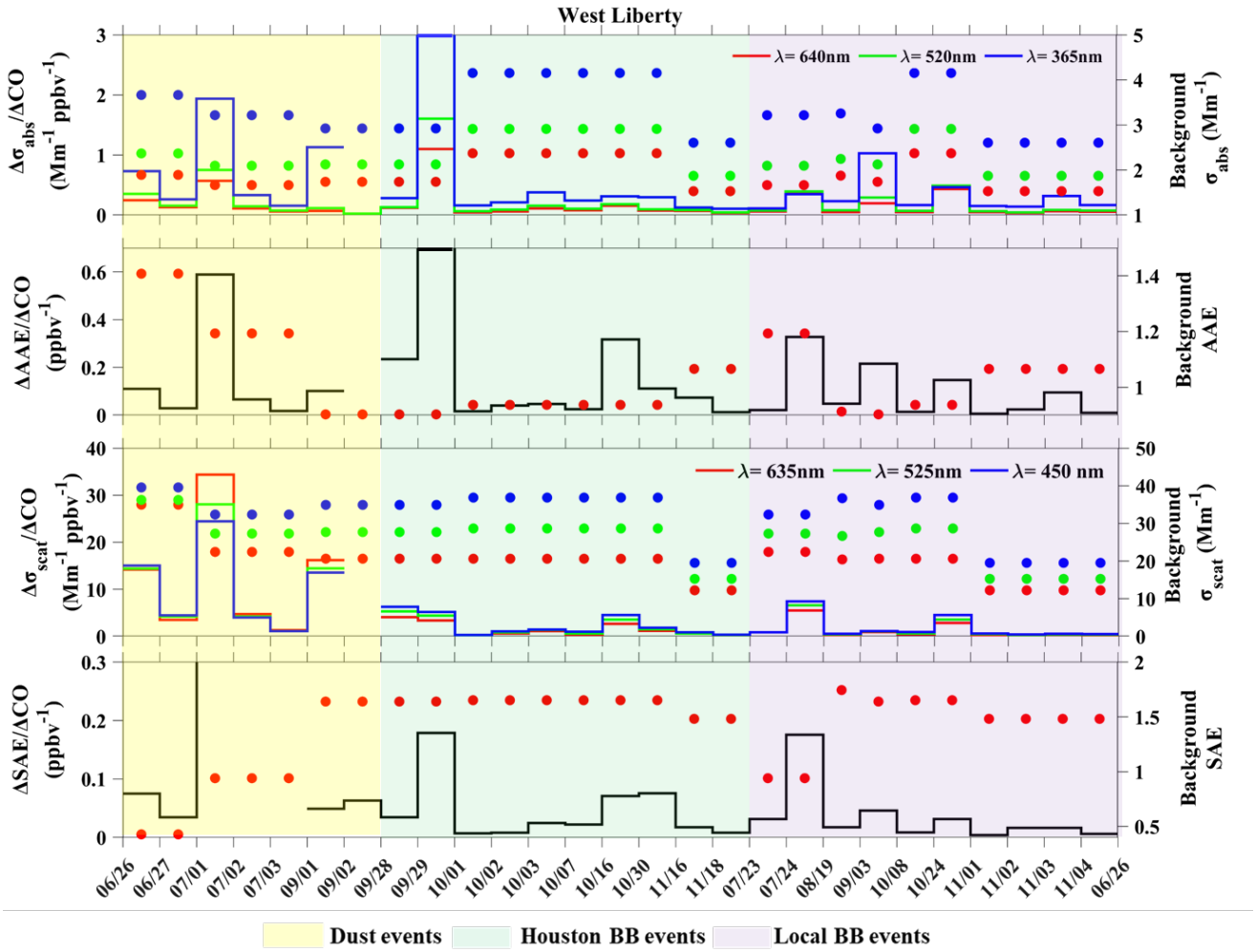

Figure 52. Enhancement ratios observed during the dust and biomass burning events at West Liberty. The circle (right y axis) shows the background values of the absorption/scattering coefficients at red, green and blue wavelengths, AAE and SAE taken for the calculation of the ER.

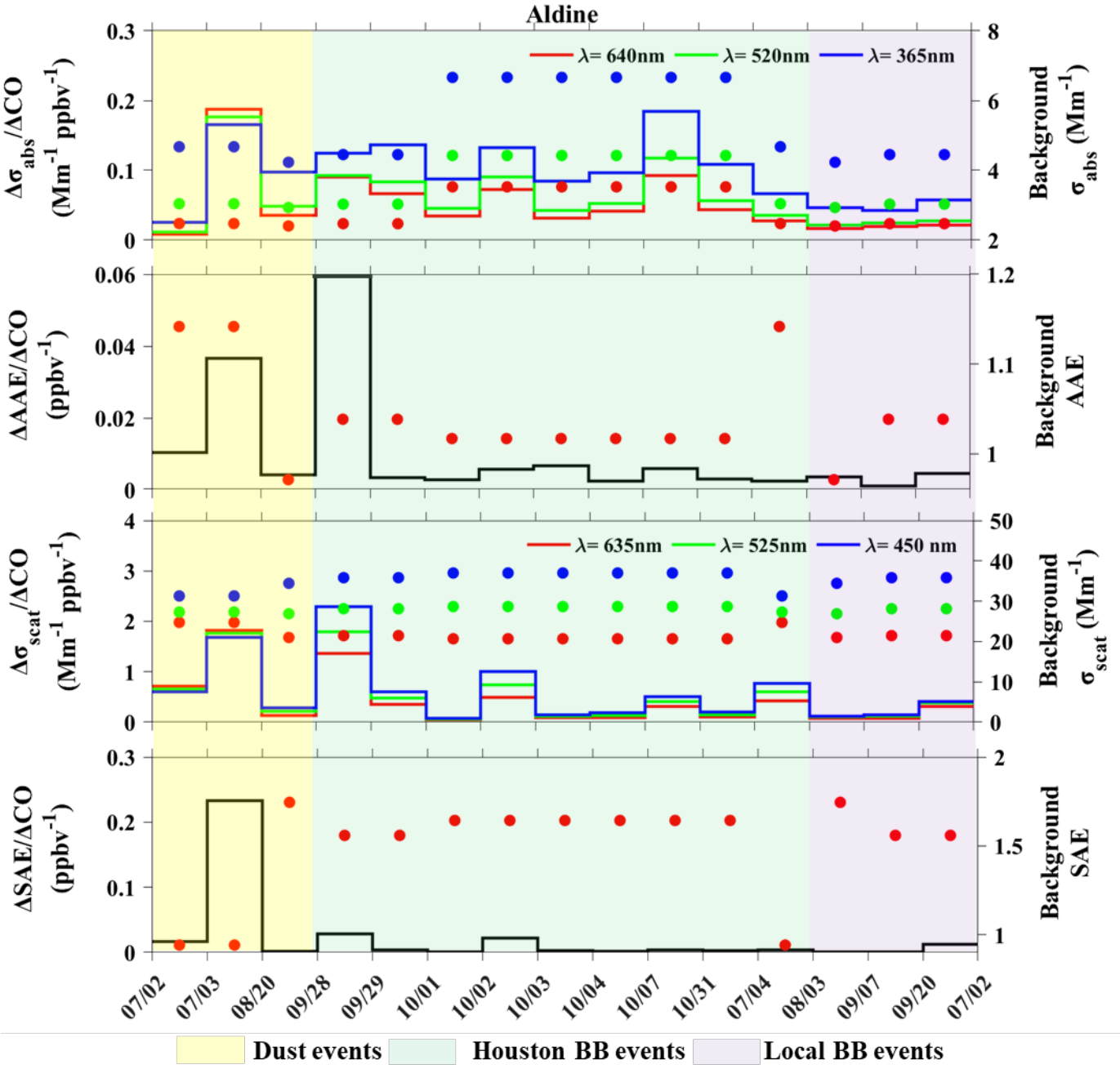

Figure 53. Enhancement ratios observed during the dust and biomass burning events at Aldine. The circle (right y axis) shows the background values of the absorption/scattering coefficients at red, green, and blue wavelengths, AAE and SAE taken for the calculation of the ER.

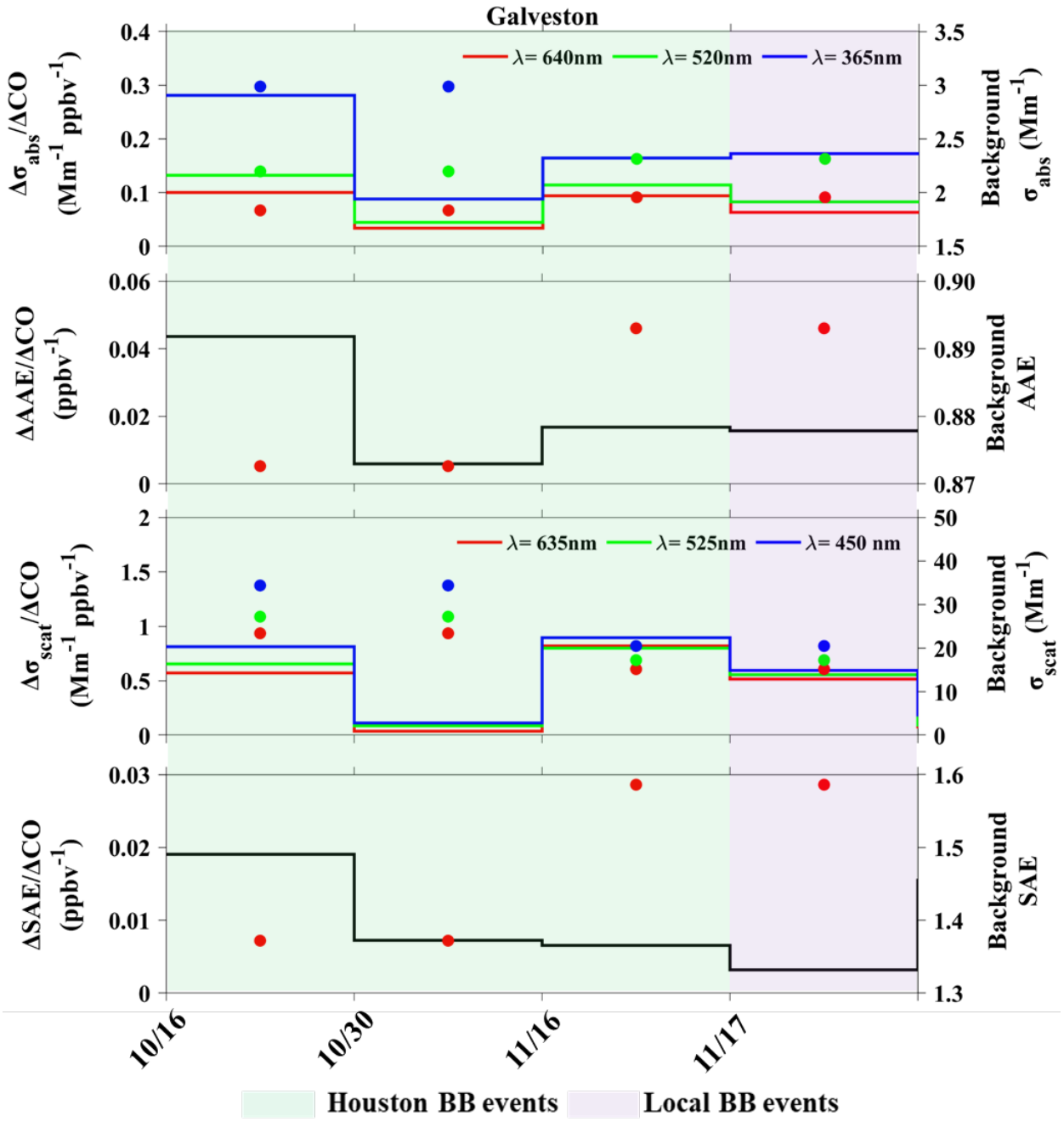

Figure 54. Enhancement ratios observed during the biomass burning events at Galveston. The circle (right y axis) shows the background values of the absorption/scattering coefficients at red, green, and blue wavelengths, AAE and SAE taken for the calculation of the ER.

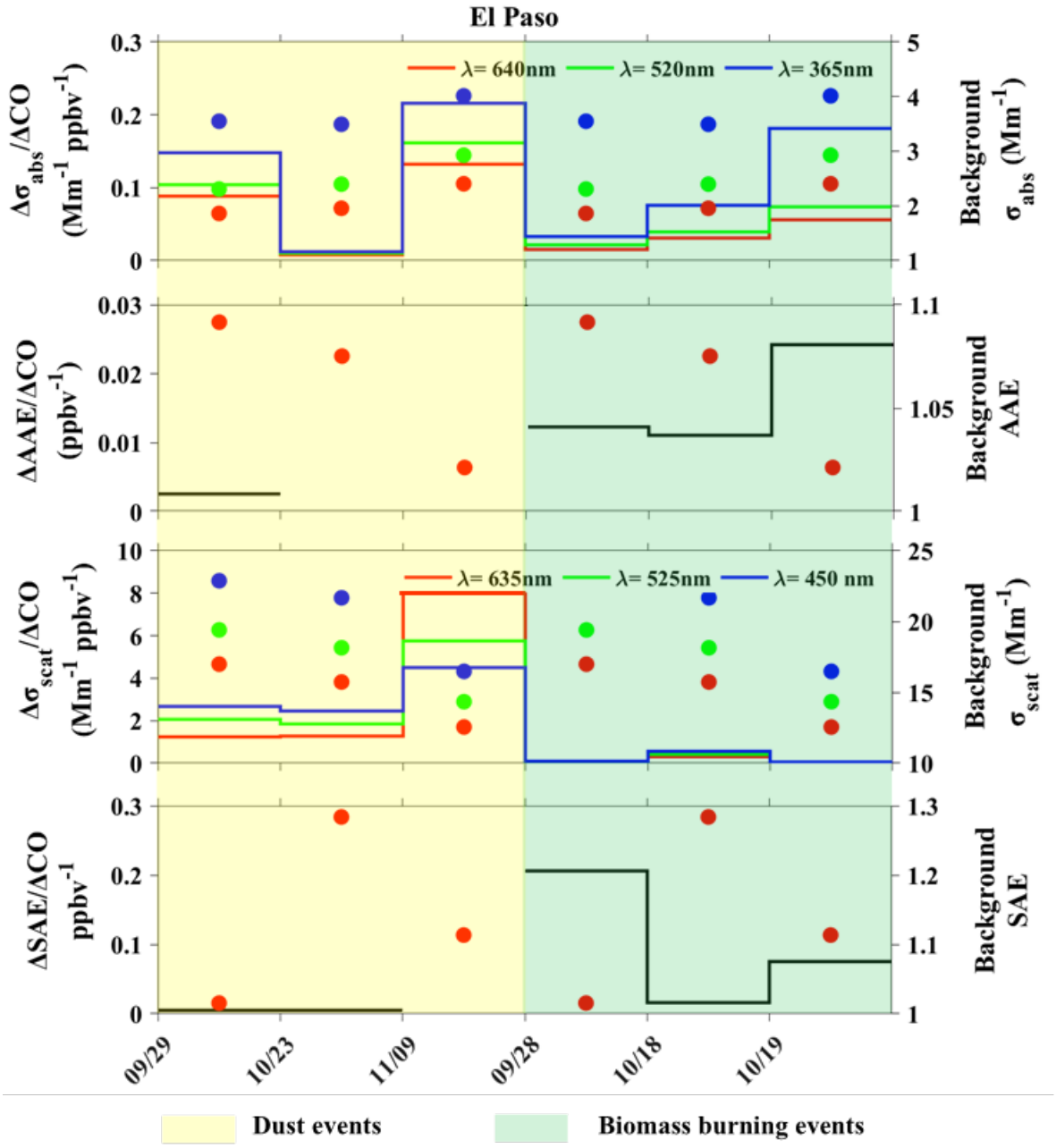

Figure 55. Enhancement ratios observed during the dust and biomass burning events at El Paso. The circle (right y axis) shows the background values of the absorption/scattering coefficients at red, green, and blue wavelengths, AAE and SAE taken for the calculation of the ER.

June-July Saharan dust – Houston + NOAA

In June – July 2020, dust originating in the Sahara was transported across the Atlantic impacting air quality and visibility in the continental United States, starting in Texas and moving into the Midwest and Appalachia. Though Saharan dust has annual impacts in the Caribbean and Texas, the June 2020 event was particularly impactful. Satellite images revealed the initial transport,

while a series of ground-based monitoring stations captured the surface impacts as the dust storm made landfall in Puerto Rico and then moved on to Texas, Illinois, and North Carolina. With a similar set of instrumentation, these sites offer a real-time assessment of the aerosol optical properties as this massive dust plume is transported across the US. The Puerto Rico, Illinois and North Carolina sites are part of NOAA's Federated Aerosol Network (NFAN) which monitors aerosol concentration, absorption, scattering and cloud condensation nuclei using a unified protocol and set of instrumentation. The Texas sites are part of the newly constructed Texas Commission on Environmental Quality Black and Brown Carbon $(BC)^2$ network which operates in Houston and El Paso using a similar protocol as NFAN to measure aerosol scattering and absorption. The NFAN and $(BC)^2$ networks utilize three wavelength aerosol photometers (CLAP and TAP, respectively) to monitor aerosol absorption and three wavelength nephelometers (TSI and Aurora, respectively) to monitor aerosol scattering. As the Saharan dust was transported into and through each site, aerosol concentrations increased dramatically with the scattering coefficients while the scattering Angstrom exponent decreased to zero. While the dust arrived in Puerto Rico by June 22 increasing the PM_{10} 550 nm scattering coefficient to over 300 Mm^{-1} , it took several days to travel to the Texas coast, impacting Galveston late on June 25 and then into Houston early on June 26 with hourly $PM_{2.5}$ exceeding 100 $\mu g\ m^{-3}$, and the 525 nm scattering coefficient exceeding 140 Mm^{-1}. The dust arrived in North Carolina and Illinois on the night of June 27 with the 550 nm scattering coefficients for PM_{10} exceeding 200 and 60 Mm^{-1}, respectively.

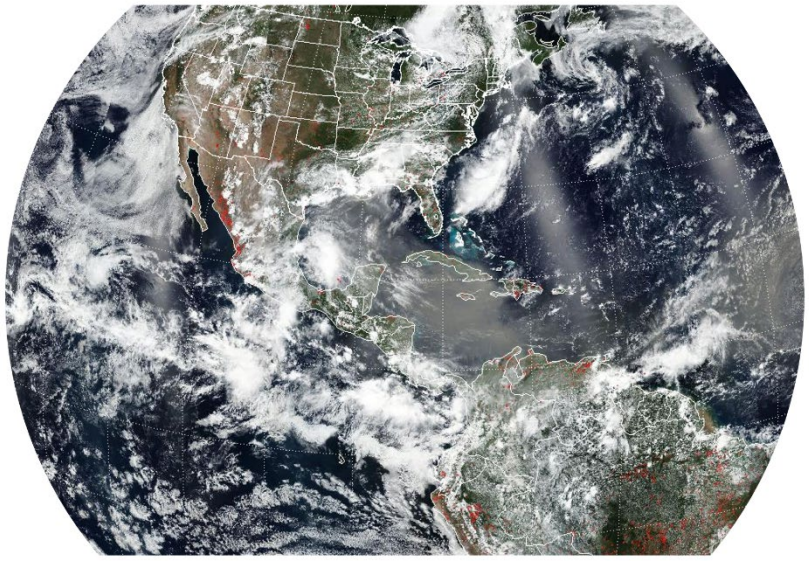

Figure 56. VIIRS (Visible Infrared Imaging Radiometer Suite Instrument) true-color composite image showing blowing dust over the Gulf of Mexico during June 22, 2020.

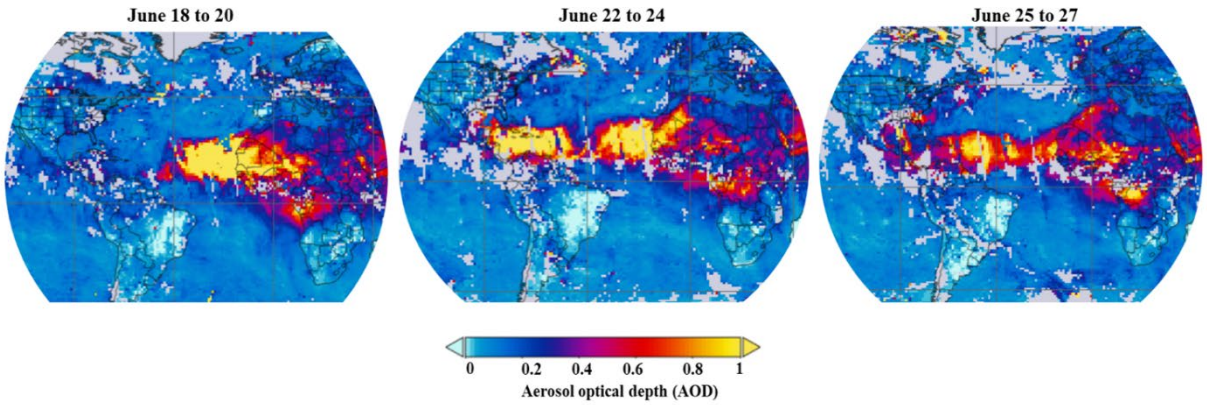

Figure 57. Spatial distribution of mean aerosol optical depth (AOD) at 550 nm derived from MODIS Terra deep blue product showing transport of dust from Sahara Desert to Southern US through Gulf of Mexico from June 18 to June 27, 2020.

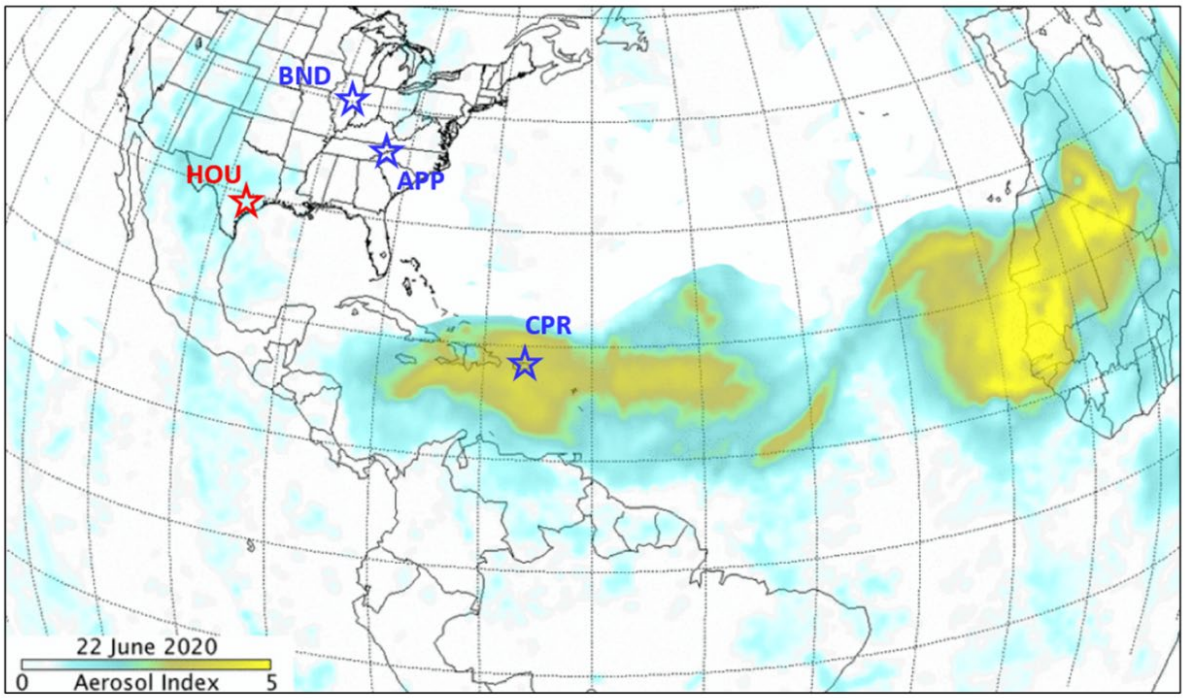

Figure 58. Spatial distribution of aerosol index (AI) over the study sites on June 22, 2020 as retrieved from NASA-NOAA's Suomi NPP satellite.

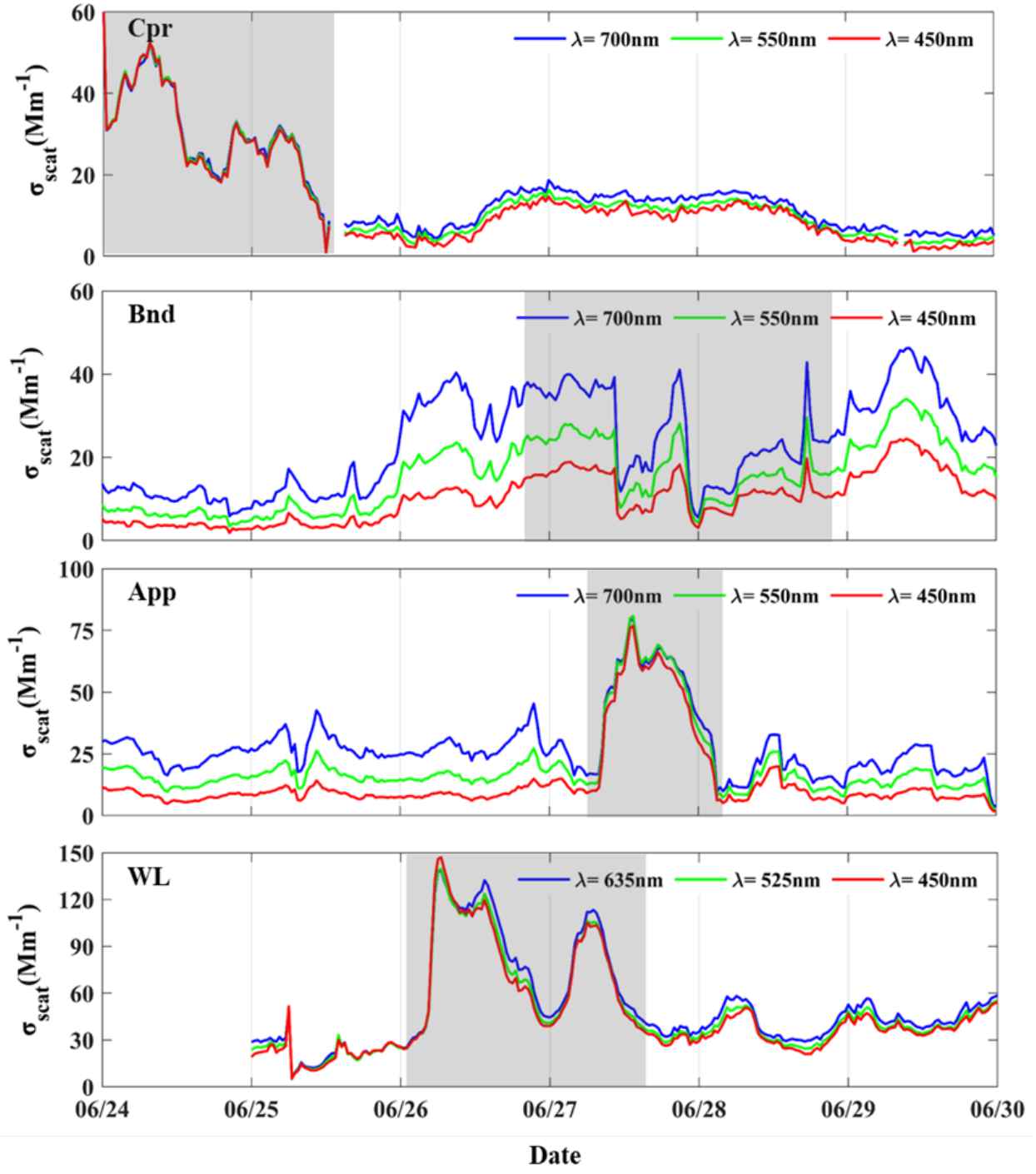

Figure 59. Time series (hourly average) for fine PM scattering coefficient (σ_{scat}) observed at Puerto Rico (CPR), West Liberty (WL), Bondville (BND), and Appalachian State University (APP) during the month of June 2020. The shaded box highlights the dust events at each site.

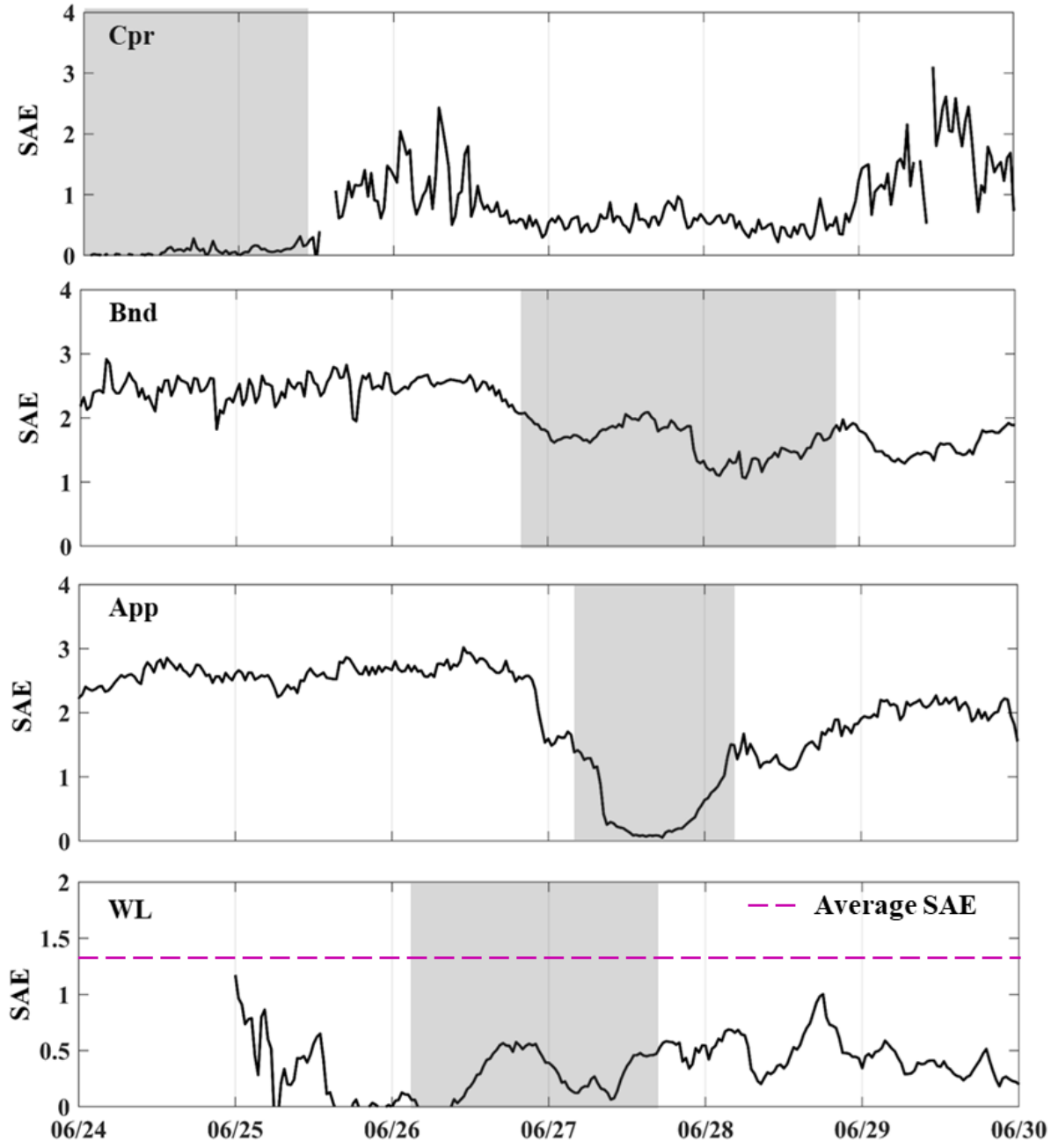

Figure 60. Time series (hourly average) of fine PM scattering Angstrom exponent (SAE) observed at Puerto Rico (CPR), West Liberty (WL), Bondville (BND), and Appalachian State University (APP) during the month of June 2020. The shaded box highlights the dust event at the specific site. The pink dashed line indicates the campaign average SAE (Jun-Oct 2020) for WL.

5. Data Audits and Quality Assurance

5.1. Aerosol absorption – TAP A and TAP B

5.1.1. Data Audit

As part of the project's design to provide a 10% data quality audit, key instruments were deployed in duplication. TAP A and TAP B at all the sites were operated simultaneously for greater than 10% of the total sampling days (Figure 44-47). This allowed for the direct comparison of aerosol absorption between the two TAPs instruments (i.e., TAP A and TAP B) for a wide range of absorption coefficients at each site. Modeling the relationship using a simple linear regression analysis allows for a quick and accurate assessment of the data (greater than 10% for each wavelength). The regression analysis shows strong correlations between the two instruments (for all three wavelengths), with $r^2 >> 0.90$ and a slope >> 0.90 (i.e., nearly 1). The derived AAE data from TAP A and TAP B was also examined using a linear regression model and show a strong agreement between the two instruments ($r^2 >> 0.8$ and a slope >> 0.80; Figure 44-47). A small variability in absorption coefficient results in considerable change in AAE which thereby resulted in slightly lower r^2 for AAE compared to the absorption coefficients. As the comparison data is 5min averages, there are a couple outliers present. These were not an indication of any special case and are not evident in hourly averages.

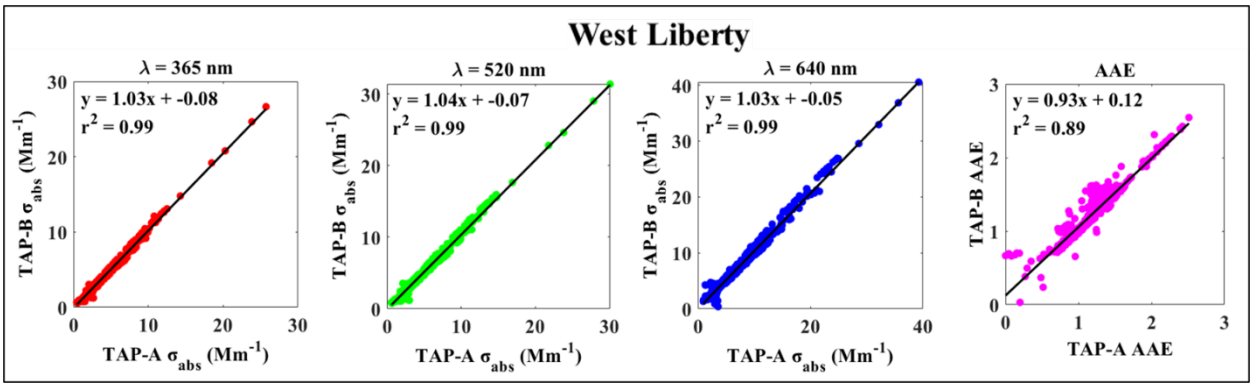

Figure 61. Scatter plot between the aerosol absorption coefficient (Mm-1) measured at 365, 520 and 640 nm and calculated AAE using σabs measured using TAP A and TAP B (five-minute averages) at West Liberty.

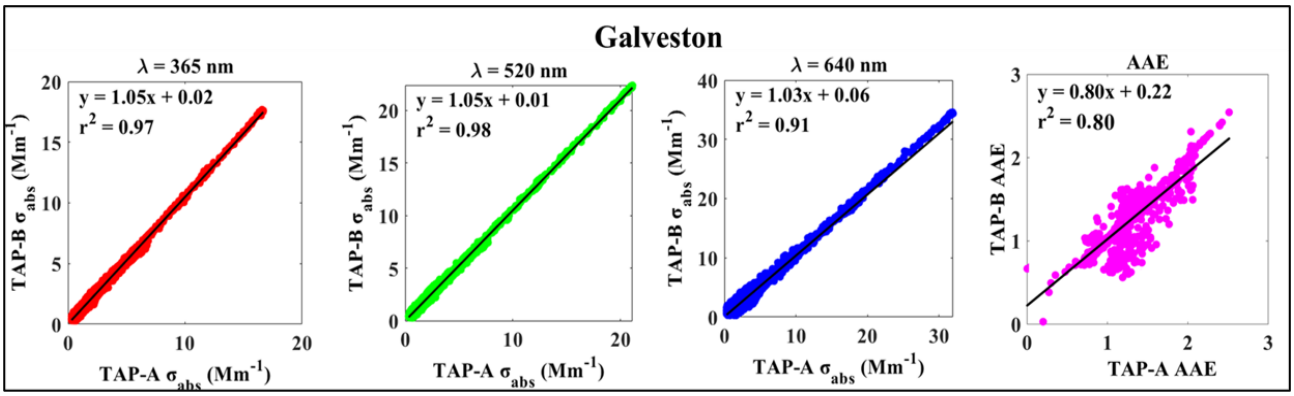

Figure 62. Scatter plot between the aerosol absorption coefficient (Mm-1) measured at 365, 520 and 640 nm and calculated AAE using σabs measured using TAP A and TAP B (five-minute averages) at Galveston.

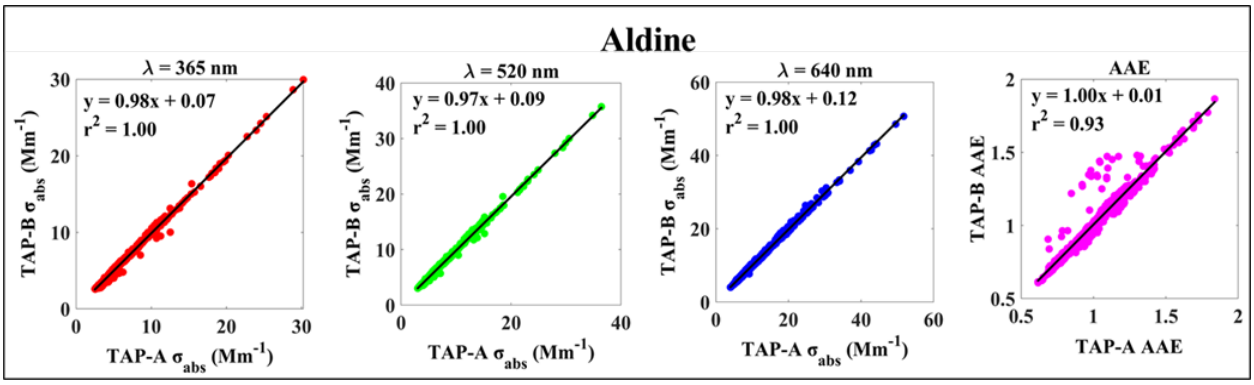

Figure 63. Scatter plot between the aerosol absorption coefficient (Mm^{-1}) measured at 365, 520 and 640 nm and calculated AAE using σ_{abs} measured using TAP A and TAP B (five-minute averages) at Aldine.

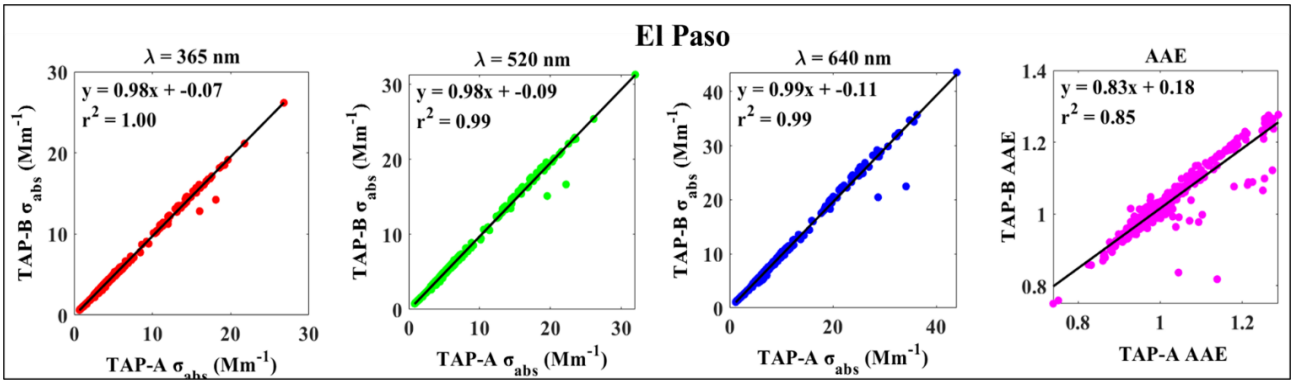

Figure 64. Scatter plot between the aerosol absorption coefficient (Mm^{-1}) measured at 365, 520 and 640 nm and calculated AAE using σ_{abs} measured using TAP A and TAP B (five-minute averages) at El Paso.

5.1.2. TAP intercomparison – all

Prior to field deployment, the TAPs were intercompared. Due to the Covid delays, all eight TAPs were not shipped at the same time. Therefore, in the first batch, four out of eight TAPs were received from Brechtel. Whereas, in the second batch, rest of the four TAPS were received from Brechtel. The TAPs were numbered 1 through 8, and pairs were deployed at West Liberty (TAPs 1 and 2), Aldine (3 and 4), El Paso (5 and 6), and Galveston (7 and 8).

The absorption coefficients at all three wavelengths and the calculated AAE values were compared between the TAPs. Figures below shows the correlation between TAPs 1 through 4 at red (640 nm), green (520 nm), blue (365nm) wavelengths and AAE. Whereas figures 47(b)-50(b) shows the correlation between TAPs 5 through 8 at red (640 nm), green (520 nm), blue (365nm) wavelengths and AAE. The absorption coefficient was highly correlated between the TAPS at all the wavelength with the coefficient of determination (r^2) of above 0.97 and the slopes closer to 1. Whereas the AAE between the TAPs also had good agreement with r^2 above 0.8 and slope closer to 1.

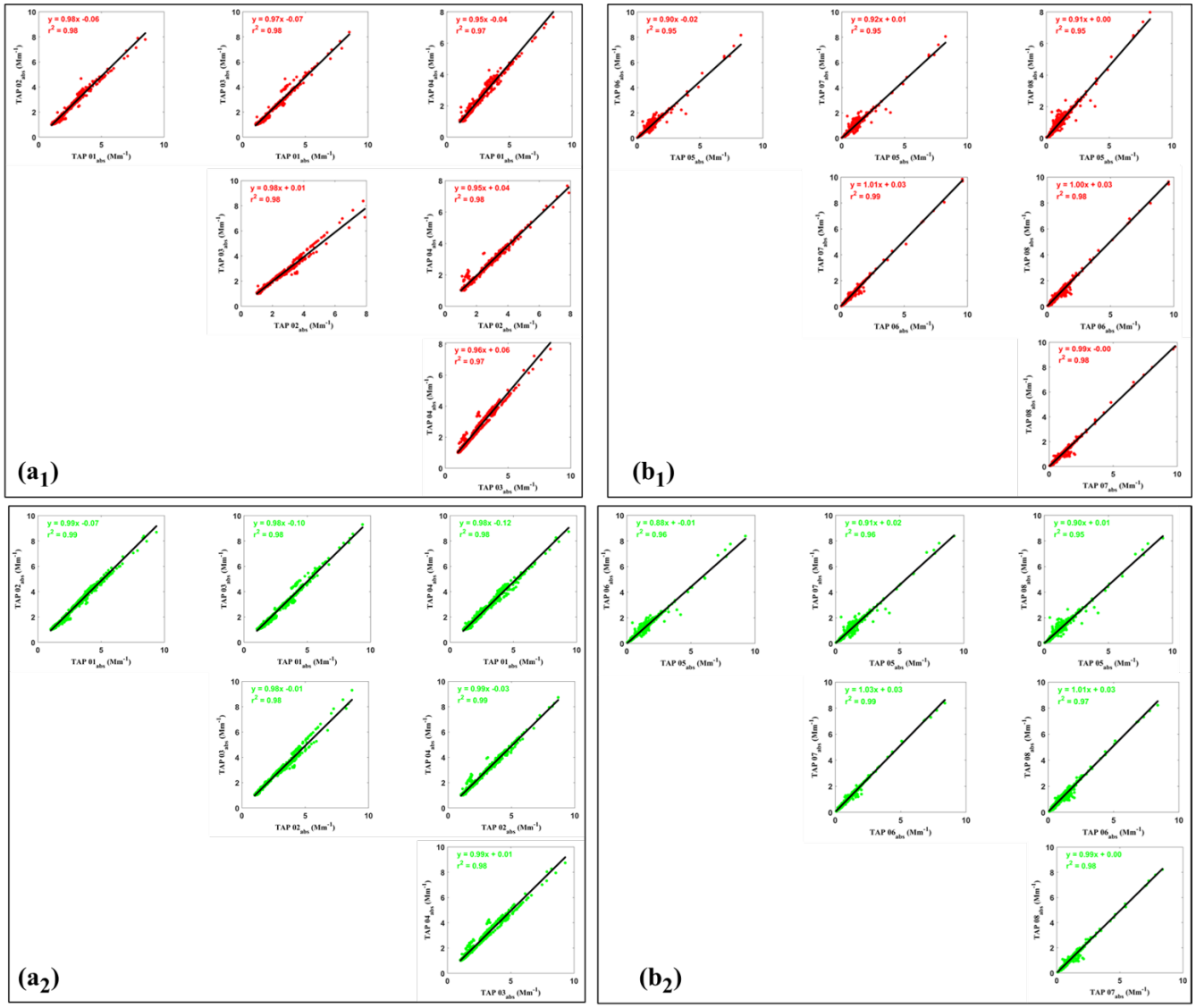

Figure 65. Scatter plot between the aerosol absorption coefficient (Mm^{-1}) at 640 nm and 520 nm wavelengths using measurements from TAP serial numbers 01 to 02 (a_1 to a_2) and TAP 05 to TAP 06 (b_1 to b_2).

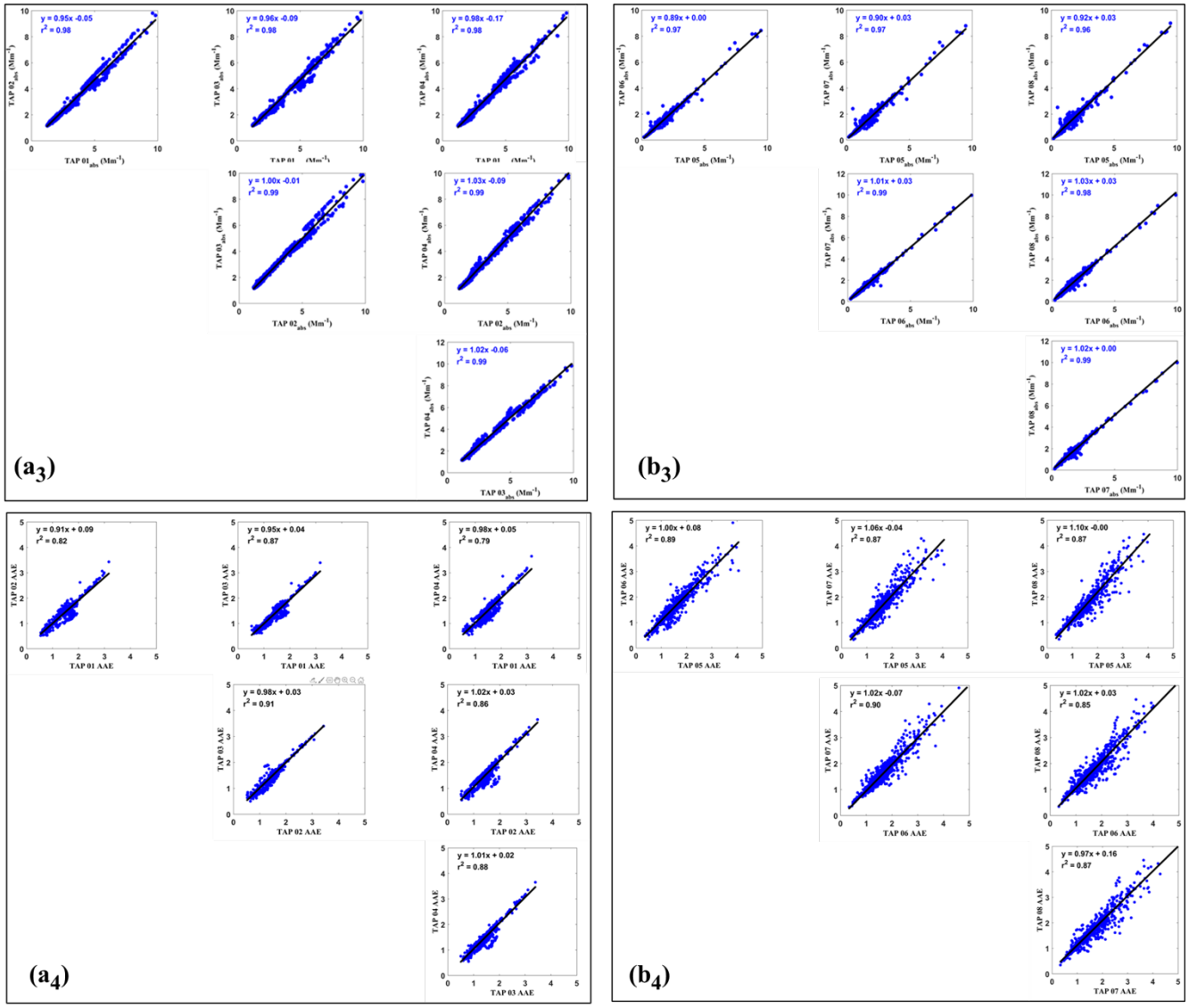

Figure 66. Scatter plot between the aerosol absorption coefficient (Mm^{-1}) at 365 nm wavelengths and calculated AAE using measurements from TAP serial numbers 03 to 04 (a_3 to a_4) and TAP 07 to TAP 08 (b_3 to b_4).

5.1.3. Completeness, precision, and accuracy

Using the two TAP instruments, the completeness of the aerosol absorption measurements for the campaign was greater than 99.9 percent. The scatter plots (above) also suggest a high level of precision and accuracy between the pairs of instruments and overall.

5.2. Aerosol Scattering – Nephelometer

5.2.1. Data Audit

To fulfill the 10% required data audit, nephelometer total scattering data measured during the entire campaign was corrected for angular truncation using Anderson and Ogren (2007) method for all three wavelengths (Figure 49-52). The coefficient of determination (r^2) between the true total scattering coefficient and uncorrected scattering coefficients is greater 0.97 at all the three (635 nm, 525 nm, and 450 nm) wavelengths. The slope of the linear regression shows that the uncorrected total scattering is around 22%, 16% and 13% lower at West Liberty, 17%, 13% and 12% lower at Aldine, 15%, 12% and 10% lower at Galveston and 21%, 17% and 14% lower at El Paso than the corrected total scattering at 635, 525 and 450 nm respectively. The observed bias in present measurement is in the range as reported by Moosmuller and Arnott (2003).

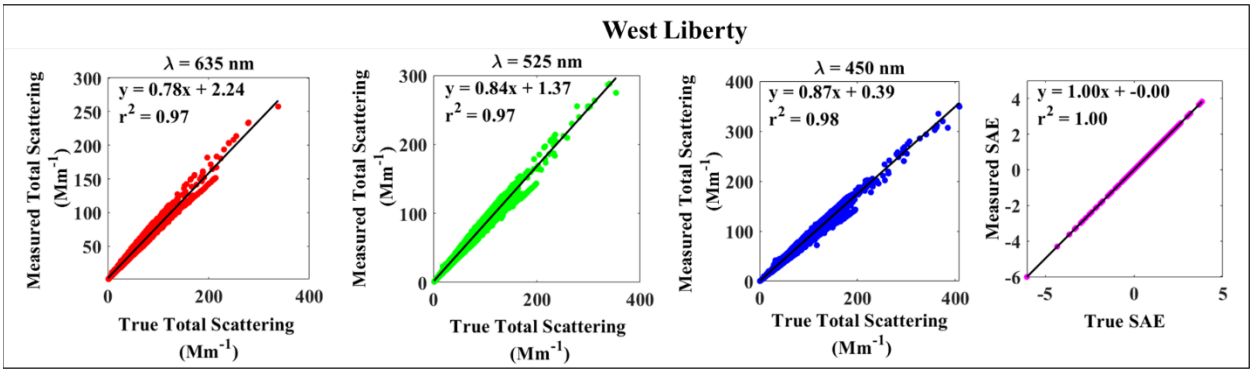

Figure 67. Scatter plot between the measured total aerosol scattering coefficient (Mm^{-1}), total aerosol scattering corrected for angular truncation (true total scattering; Mm^{-1}) and calculated SAE at 635, 525 and 450 nm at West Liberty.

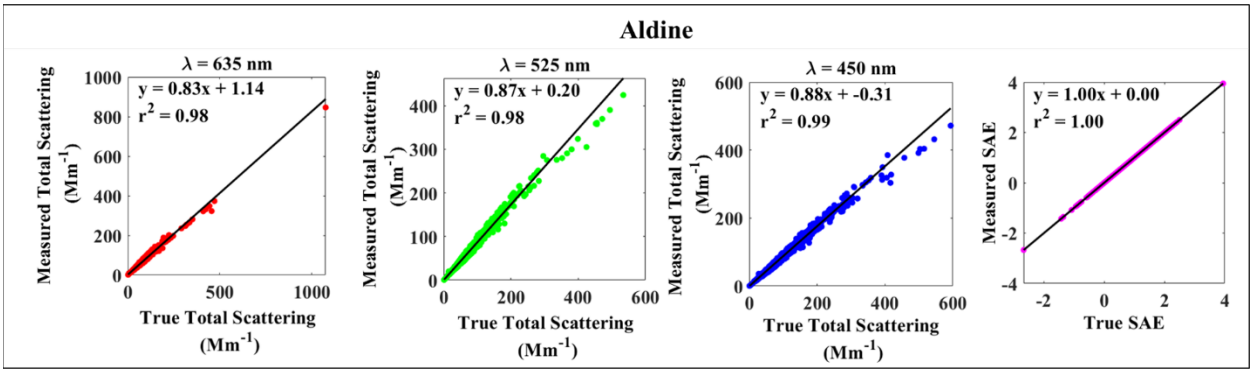

Figure 68. Scatter plot between the measured total aerosol scattering coefficient (Mm^{-1}), total aerosol scattering corrected for angular truncation (true total scattering; Mm^{-1}) and calculated SAE at 635, 525 and 450 nm at Aldine.

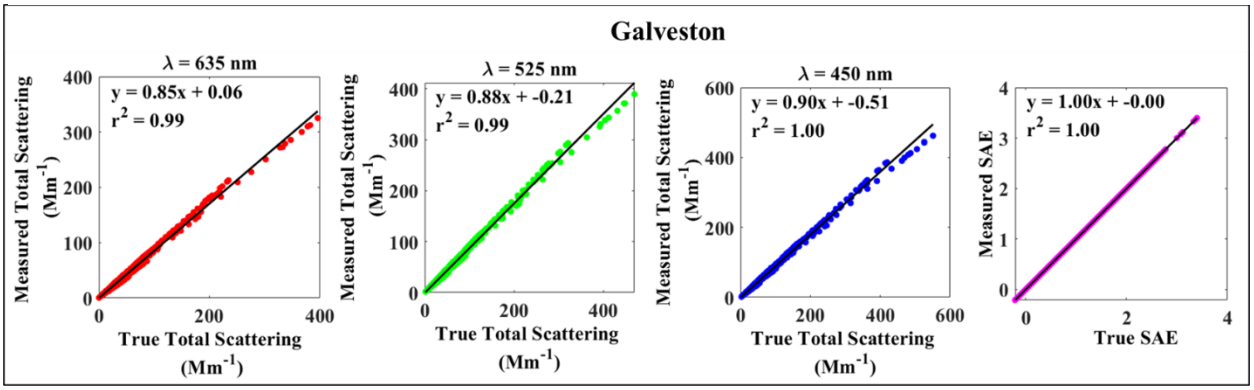

Figure 70. Scatter plot between the measured total aerosol scattering coefficient (Mm^{-1}), total aerosol scattering corrected for angular truncation (true total scattering; Mm^{-1}) and calculated SAE at 635, 525 and 450 nm at Galveston.

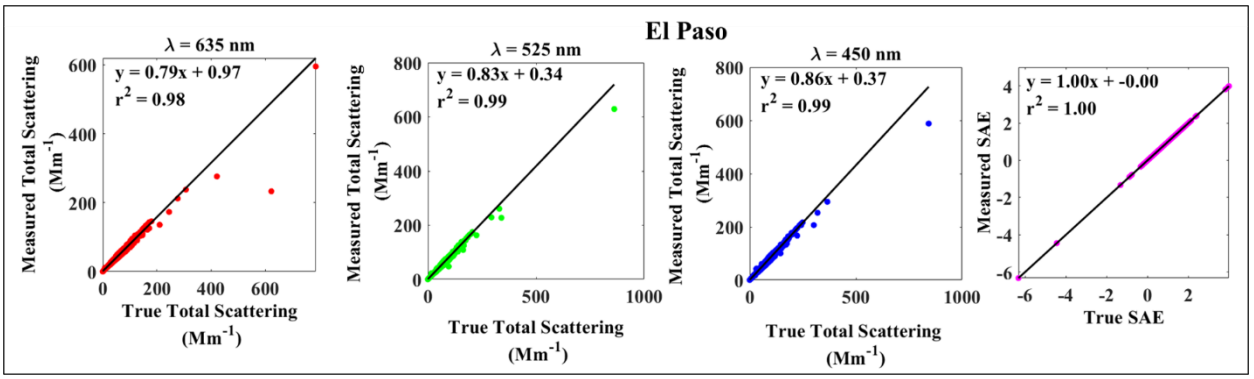

Figure 69. Scatter plot between the measured total aerosol scattering coefficient (Mm^{-1}), total aerosol scattering corrected for angular truncation (true total scattering; Mm^{-1}) and calculated SAE at 635, 525 and 450 nm at Galveston.

5.2.2. Nephelomter intercomparison – all

Similar to the TAPS, nephelometers were also intercompared prior to the field deployment. Four nephelometers were received from Ecotech. The first nephelometer we received had multiple errors including light source failure and calibration offset issues. Although we tried to fix the problems in-house, we were not completely confident in its deployment. Therefore, we requested Ecotech to replace that unit with newer one. Likewise, to the TAPs, the nephelometers were numbered through 1 through 4, of which, nephelometer 1 was deployed at El Paso, 2 at West Liberty, 3 at Aldine and 4 at Galveston. The intercomparison of the scattering coefficients at blue (450 nm), green (525 nm) and red (635 nm) wavelengths and calculated SAE values between the four nephelometers are shown in figure 53(a to d). The intercomparison results show that the scattering measurements between the nephelometers were highly correlated with r^2= 0.99 and slope closer to 1. In addition, the SAE values between the nephelometers were also highly correlated with r^2 above 0.93 and slope closer to 1.

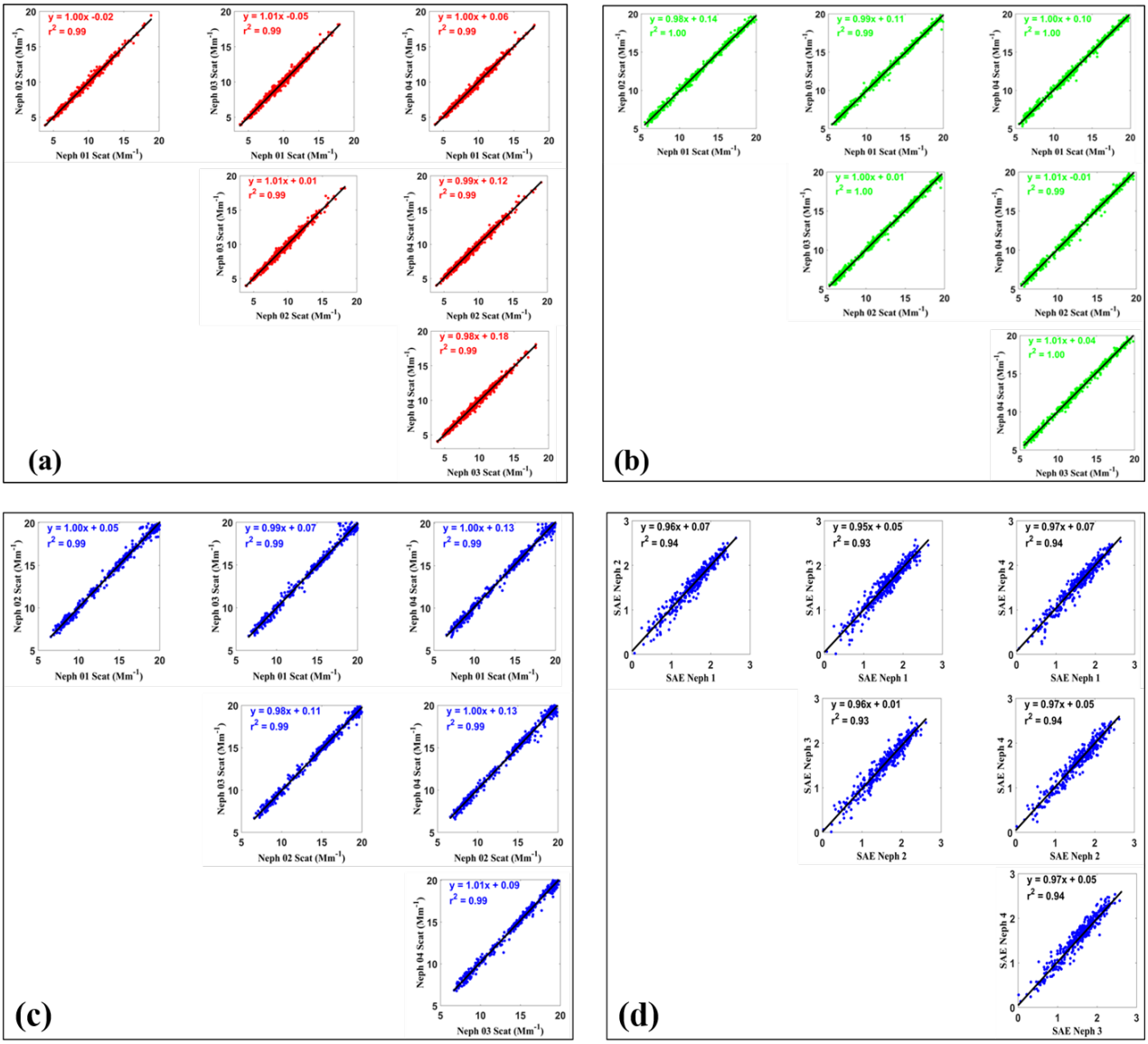

Figure 71. Scatter plot between the aerosol scattering coefficient (Mm-1) at measured (a) 635 nm (b) 525 nm (c) 450 nm and (d) calculated SAE using Nephelometer 01 to Nephelometer 04 (five-minute averages).

5.2.3. Completeness, precision, and accuracy

The completeness of the atmospheric scattering measurements for the campaign was greater than 99.9 percent. The deviation of the slope from 1 (Figures above) suggests a reasonable level of precision and accuracy in the observed ranges reported by Moosmuller and Arnott (2003).

6. **Conclusion**

Major Findings

1. Methodologies that were developed by the PIs in AQRP project 19-031 for El Paso in 2019, were also successfully deployed in Aldine, West Liberty, and Galveston to assess transport and wildfire influence in the Houston metro region.

2. The TAP + nephelometer was used to identify influence of biomass burning events on Houston metropolitan area's air quality. Findings were supported using satellite fire products, back trajectories, and aerosol composition measurements from co-located $PM_{2.5}$ filters.
    a. Filter-based composition provided additional ways to quantify wildfire impact via radiocarbon to soluble potassium ratios. It also illustrated the utility of sodium as an inland tracer for the extent and duration Saharan dust transport during Jun-July.
3. For seasonality during $(BC)^2$ 2020, the Saharan dust in July and Western wildfire in October were identified at multiple $(BC)^2$ 2020 sites. Saharan dust was supported using MODIS aerosol optical depth measurements and aerosol composition. While Western wildfire was supported via NOAA HMS smoke, trajectory analysis and radiocarbon.
    a. The late fire season in October and November provided examples of long range and local biomass burning impacts. The three sites in the Houston metro area were used to better characterize the extent and influence of smoke events and to help better define source regions.
4. The TAP + nephelometer instrument suite provided a relatively low maintenance solution to conducting a long-term BB and dust monitoring campaigns and is sensitive enough to identify BB events when changes in PM concentrations alone are not indicative.
    a. The real-time nature of the aerosol optical measurements allows for better precision in characterizing the transport, intensity, and duration of smoke into these urban areas.

5. The expansion of $(BC)^2$ to include the deployment and remote monitoring of multiple sites (spanning 750 miles along the 1-10 corridor) highlights the strength and flexibility of this approach and the utility of these methodologies even in a complex urban atmosphere, such as El Paso and Aldine as well as coastal and rural sites.

7. **Recommendations for Additional Studies**

1. The continuation of $(BC)^2$ to identify and assess periods of BB and dust influence in the Houston and El Paso metropolitan area. The $(BC)^2$ 2020 dataset will serve as the foundation for future multi-year studies to assess long-term trends by season and by urban area.
    a. Long term monitoring of wildfire and dust will also help to characterize any changes in these source impacts over time.
2. Along with site-specific AAEs developed in 2020, continue to analyze co-located $PM_{2.5}$ filters for radiocarbon and potassium ion, to quantify the impact of biomass burning on $PM_{2.5}$ concentrations and to establish a site-specific relationship between changes in AAE and the contribution of biomass burning.
3. Utilize aerosol optical data collected during the Corpus Christie San Antonio 2021 mobile field campaign and known or suspected areas of BB influence in 2020 and 2021 to identify potential $(BC)^2$ expansion sites along the 1-35 corridor. Note: that San Antonio would serve both the east-west and north-south sampling strategies.
4. Consider expansion to PM_{10} monitoring of aerosol absorption and scattering to better describe dust impacts in El Paso. This would also enable better characterization of potential mixed dust and smoke events which are anticipated when the dust is transported through regions of wildfire or agricultural burning prior to reaching El Paso.

8. References

1. Laing, J.R., D.A. Jaffe, and J.R. Hee, *Physical and optical properties of aged biomass burning aerosol from wildfires in Siberia and the Western USA at the Mt. Bachelor Observatory.* Atmos. Chem. Phys., 2016. **16**(23): p. 15185-15197.
2. Andreae, M.O. and A. Gelencser, *Black carbon or brown carbon? The nature of light-absorbing carbonaceous aerosols.* Atmospheric Chemistry and Physics, 2006. **6**: p. 3131-3148.
3. Bond, T.C. and R.W. Bergstrom, *Light absorption by carbonaceous particles: An investigative review.* Aerosol science and technology, 2006. **40**(1): p. 27-67.
4. Becerril-Valle, M., et al., *Characterization of atmospheric black carbon and co-pollutants in urban and rural areas of Spain.* Atmospheric Environment, 2017. **169**: p. 36-53.
5. Tasoglou, A., et al., *Absorption of chemically aged biomass burning carbonaceous aerosol.* Journal of Aerosol Science, 2017. **113**: p. 141-152.
6. Healy, R.M., et al., *Ambient measurements and source apportionment of fossil fuel and biomass burning black carbon in Ontario.* Atmospheric Environment, 2017. **161**: p. 34-47.
7. Titos, G., et al., *Spatial and temporal variability of carbonaceous aerosols: Assessing the impact of biomass burning in the urban environment.* Science of the Total Environment, 2017. **578**: p. 613-625.
8. Briggs, N.L. and C.M. Long, *Critical review of black carbon and elemental carbon source apportionment in Europe and the United States.* Atmospheric Environment, 2016. **144**: p. 409-427.
9. Brown, S.G., et al., *Wintertime Residential Biomass Burning in Las Vegas, Nevada; Marker Components and Apportionment Methods.* Atmosphere, 2016. **7**(4).
10. Garg, S., et al., *Limitation of the Use of the Absorption Angstrom Exponent for Source Apportionment of Equivalent Black Carbon: a Case Study from the North West Indo-Gangetic Plain.* Environmental Science & Technology, 2016. **50**(2): p. 814-824.
11. Lin, Y.H., et al., *Light-Absorbing Oligomer Formation in Secondary Organic Aerosol from Reactive Uptake of Isoprene Epoxydiols.* Environmental Science & Technology, 2014. **48**(20): p. 12012-12021.
12. Xie, M.J., et al., *Light Absorption of Secondary Organic Aerosol: Composition and Contribution of Nitroaromatic Compounds.* Environmental Science & Technology, 2017. **51**(20): p. 11607-11616.
13. Cappa, C.D., et al., *Light Absorption by Ambient Black and Brown Carbon and its Dependence on Black Carbon Coating State for Two California, USA, Cities in Winter and Summer.* Journal of Geophysical Research-Atmospheres, 2019. **124**(3): p. 1550-1577.
14. Washenfelder, R.A., et al., *Biomass burning dominates brown carbon absorption in the rural southeastern United States.* Geophysical Research Letters, 2015. **42**(2): p. 653-664.
15. Sinha, P.R., et al., *Evaluation of ground-based black carbon measurements by filter-based photometers at two Arctic sites.* Journal of Geophysical Research-Atmospheres, 2017. **122**(6): p. 3544-3572.
16. Zhi, G.R., et al., *Comparison of elemental and black carbon measurements during normal and heavy haze periods: implications for research.* Environmental Monitoring and Assessment, 2014. **186**(10): p. 6097-6106.

17. Dallmann, T.R., et al., *Characterization of particulate matter emissions from on-road gasoline and diesel vehicles using a soot particle aerosol mass spectrometer.* Atmospheric Chemistry and Physics, 2014. **14**(14): p. 7585-7599.
18. Schwarz, J.P., et al., *Assessing recent measurement techniques for quantifying black carbon concentration in snow.* Atmos. Meas. Tech. Discuss., 2012. **5**(3): p. 3771-3795.
19. Bahadur, R., et al., *Solar absorption by elemental and brown carbon determined from spectral observations.* Proceedings of the National Academy of Sciences of the United States of America, 2012. **109**(43): p. 17366-17371.
20. Ram, K., M.M. Sarin, and S.N. Tripathi, *Inter-comparison of thermal and optical methods for determination of atmospheric black carbon and attenuation coefficient from an urban location in northern India.* Atmospheric Research, 2010. **97**(3): p. 335-342.
21. Subramanian, R., et al., *Black carbon over Mexico: the effect of atmospheric transport on mixing state, mass absorption cross-section, and BC/CO ratios.* Atmospheric Chemistry and Physics, 2010. **10**(1): p. 219-237.
22. Ram, K. and M.M. Sarin, *Absorption Coefficient and Site-Specific Mass Absorption Efficiency of Elemental Carbon in Aerosols over Urban, Rural, and High-Altitude Sites in India.* Environmental Science & Technology, 2009. **43**(21): p. 8233-8239.
23. Sandradewi, J., et al., *Using aerosol light absorption measurements for the quantitative determination of wood burning and traffic emission contributions to particulate matter.* Environmental Science & Technology, 2008. **42**(9): p. 3316-3323.
24. Snyder, D.C. and J.J. Schauer, *An inter-comparison of two black carbon aerosol instruments and a semi-continuous elemental carbon instrument in the urban environment.* Aerosol Science And Technology, 2007. **41**(5): p. 463-474.
25. Ogren, J.A., et al., *Continuous light absorption photometer for long-term studies.* Atmos. Meas. Tech., 2017. **10**(12): p. 4805-4818.
26. Müller, T., et al., *Characterization and intercomparison of aerosol absorption photometers: result of two intercomparison workshops.* Atmos. Meas. Tech., 2011. **4**(2): p. 245-268.
27. Kondo, Y., et al., *Emissions of black carbon, organic, and inorganic aerosols from biomass burning in North America and Asia in 2008.* Journal of Geophysical Research-Atmospheres, 2011. **116**.
28. Bond, T.C., T.L. Anderson, and D. Campbell, *Calibration and intercomparison of filter-based measurements of visible light absorption by aerosols.* Aerosol Science & Technology, 1999. **30**(6): p. 582-600.
29. Wang, X., et al., *Deriving brown carbon from multiwavelength absorption measurements: method and application to AERONET and Aethalometer observations.* Atmospheric Chemistry and Physics, 2016. **16**(19): p. 12733-12752.
30. Sandradewi, J., et al., *Using aerosol light absorption measurements for the quantitative determination of wood burning and traffic emission contributions to particulate matter.* Environmental science & technology, 2008. **42**(9): p. 3316-3323.
31. Schmeisser, L., et al., *Classifying aerosol type using in situ surface spectral aerosol optical properties.* Atmos. Chem. Phys., 2017. **17**(19): p. 12097-12120.
32. Sheesley, R.J., et al. *Transport and Impacts of the June 2020 Saharan Dust Event on the Continental US*. in *AGU Fall Meeting Abstracts*. 2020.
33. Holland, H.D., *The chemistry of the atmosphere and oceans-(v. 1).* 1978.

34. Giardi, F., et al., *Size distribution and ion composition of aerosol collected at Ny-Ålesund in the spring–summer field campaign 2013.* Rendiconti Lincei, 2016. **27**(1): p. 47-58.
35. May, N., et al., *Multiyear study of the dependence of sea salt aerosol on wind speed and sea ice conditions in the coastal Arctic.* Journal of Geophysical Research: Atmospheres, 2016. **121**(15): p. 9208-9219.
36. Quinn, P., et al., *A 3-year record of simultaneously measured aerosol chemical and optical properties at Barrow, Alaska.* Journal of Geophysical Research: Atmospheres, 2002. **107**(D11).
37. Virkkula, A., et al., *Chemical composition of boundary layer aerosol over the Atlantic Ocean and at an Antarctic site.* Atmospheric Chemistry and Physics, 2006. **6**(11): p. 3407-3421.
38. Wagenbach, D., et al., *Sea-salt aerosol in coastal Antarctic regions.* Journal of Geophysical Research: Atmospheres, 1998. **103**(D9): p. 10961-10974.
39. Stein, A.F., et al., *Noaa's Hysplit Atmospheric Transport and Dispersion Modeling System.* Bulletin of the American Meteorological Society, 2015. **96**(12): p. 2059-2077.
40. Rolph, G., A. Stein, and B. Stunder, *Real-time Environmental Applications and Display sYstem: READY.* Environmental Modelling & Software, 2017. **95**: p. 210-228.
41. Schmeisser, L., et al., *Classifying aerosol type using in situ surface spectral aerosol optical properties.* Atmospheric Chemistry and Physics, 2017. **17**(19): p. 12097-12120.
42. Singh, A., P. Pant, and F.D. Pope, *Air quality during and after festivals: Aerosol concentrations, composition and health effects.* Atmospheric Research, 2019. **227**: p. 220-232.
43. Yoon, S., et al., *Apportioned primary and secondary organic aerosol during pollution events of DISCOVER-AQ Houston.* Atmospheric Environment, 2021. **244**: p. 117954.
44. Yoon, S., S. Usenko, and R.J. Sheesley, *Fine and Coarse Carbonaceous Aerosol in Houston, TX, during DISCOVER-AQ.* Atmosphere, 2020. **11**(5): p. 482.

Addendum to:

Final Report for Black and Brown Carbon $(BC)^2$ Monitoring in Houston and El Paso in 2020; PGA: 582-20-12102-011; Grant Number: 582-18-81339

Assessment of potential contribution of calcium carbonate to filter-based organic and elemental carbon concentrations at $(BC)^2$ sites. With high local dust levels, there was concern that the filter-based organic and elemental carbon concentrations may be biased high due to inclusion of carbonate. To verify that the carbonate does not have a significant impact on the $PM_{2.5}$, an acidification study was conducted for the El Paso samples in late Sept – early Nov 2020. For this test, the total carbon (TC; sum of organic and elemental carbon) was considered using the same OC:EC methodology employed for the rest of the $(BC)^2$ project. For this test, two filter punches were used for each sample. One filter was run for total carbon. The second filter was acidified using HCl in a desiccator overnight, dried to remove excess humidity and then run for total carbon. Any carbonate would be removed during this process and show as a deficit in the acidified TC that is beyond the TC uncertainty. The results indicate that no carbonate was present in the samples that could be detected in the TC analysis.

Added Jul 12, 2021 to the June 30, 2021 V2 of the final report.

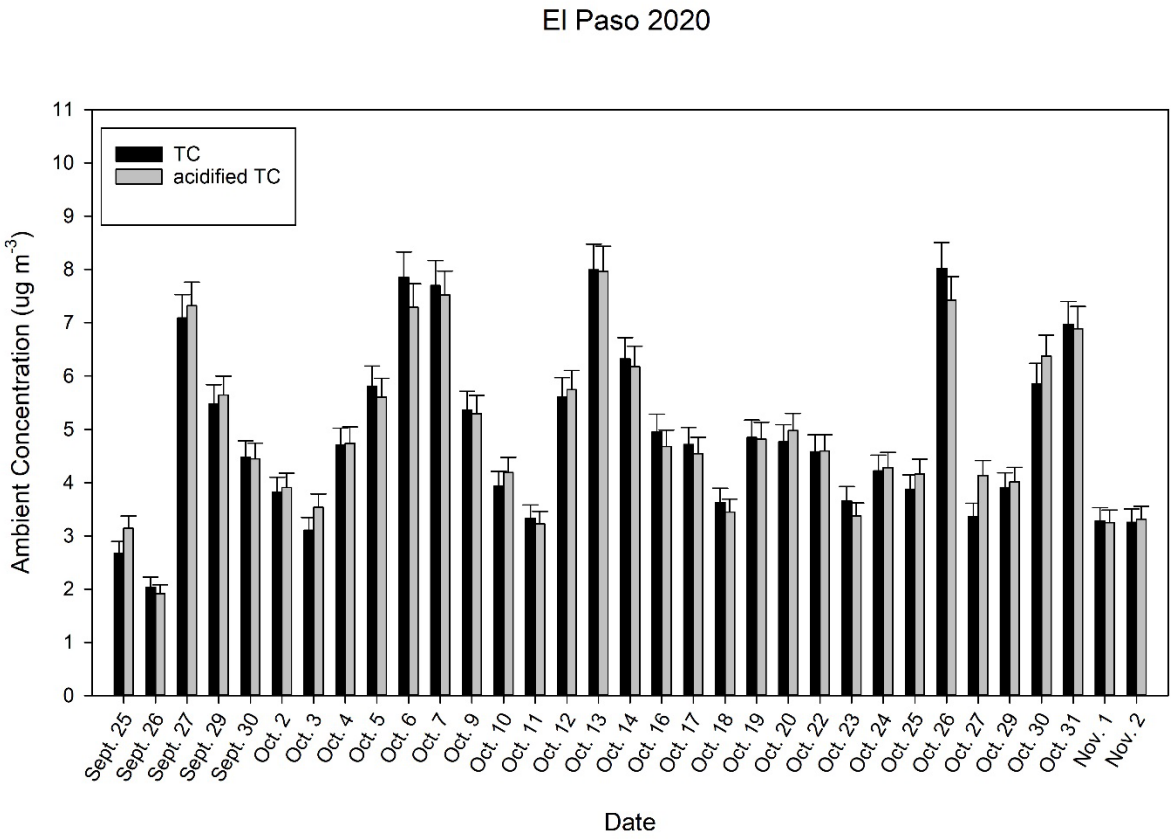

Figure A1: Total carbon (TC) and acidified TC for El Paso filters from 2020. The error bars are the instrument uncertainty for TC.